Author:
Osman, Sara J

Title:
Understanding particle size distributions to improve ash dispersal modelling

Understanding particle size distributions to improve ash dispersal modelling

Sara J. Osman

Supervisors: Alison Rust, University of Bristol

Frances Beckett, Met Office

A dissertation submitted to the University of Bristol in accordance with the requirements for award of the degree of Master of Science by Research in the Faculty of Science.

School of Earth Sciences

August 2019

12,864 words

Abstract

Volcanic eruptions can generate large volumes of ash and cause far-reaching air traffic disruption. To mitigate against aircraft encounters with ash clouds Volcanic Ash Advisory Centres (VAACs) forecast the expected location of the ash in the atmosphere. The size distribution of particles making up an ash cloud can vary significantly with eruption, but it is important to initialise dispersion models with an appropriate particle size distribution (PSD) because sedimentation rates are controlled by particle size. This project aims to better understand the range of PSDs generated from volcanic ash eruptions and consider the use of PSDs in ash dispersion modelling.

To understand the process of grain size analysis, I collected and analysed samples from the Minoan eruption on Santorini, compiled a total grain size distribution (TGSD) for the 1919 eruption of Kelut and calculated median grain size for a sample from the Askja 1875 eruption.

I compiled published grain size data and found that for large phreatomagmatic eruptions, grain size remains relatively constant with distance. This suggests that TGSDs for these eruptions could be compiled from fewer samples than are required for typical magmatic eruptions, which in turn could provide a larger dataset for dispersion modelling and studies on controls of eruption intensity.

To test the sensitivity of modelled ash concentrations to the input size distribution, I ran NAME with a range of PSDs from different types of eruption. I found clear differences between modelled mass loadings and the extent of the plume for mafic and silicic eruptions. The default PSD used by the London VAAC is most similar to the finest (silicic) test eruptions and I recommend that a second default PSD should be considered for operational forecasting, suitable for coarse-grained, mafic eruptions. This could be compiled from ground and airborne samples or based on a suitable statistical distribution.

Dedication and Acknowledgements

I would like to thank my supervisors Alison Rust and Frances Beckett for all the help and encouragement they have given me throughout the year. I have learned a huge amount and this project would not have been nearly so enjoyable without their enthusiastic support.

Thanks also to my partner, Steve, without whom this would not have been possible at all.

Author’s declaration

I declare that the work in this dissertation was carried out in accordance with the requirements of the University's *Regulations and Code of Practice for Research Degree Programmes* and that it has not been submitted for any other academic award. Except where indicated by specific reference in the text, the work is the candidate's own work. Work done in collaboration with, or with the assistance of, others, is indicated as such. Any views expressed in the dissertation are those of the author.

SIGNED: ..... DATE:.....

Table of contents

Figures

Tables

Chapter 1 Introduction

Volcanic eruptions can generate large volumes of ash which are then transported and dispersed by the wind and our turbulent atmosphere. The resulting ash clouds can travel huge distances from their source and cause severe disruption to air traffic, as jet engines can fail when the ash particles are ingested (e.g. Casadevall, 1994; Giehl et al., 2017; Song et al., 2019). In the UK, the main volcanic ash threat is from Icelandic eruptions and because of the seasonal weather patterns, eruptions in winter are likely to cause the most widespread disruption (Dingwell and Rutgersson, 2014). To mitigate against aircraft encounters with ash clouds Volcanic Ash Advisory Centres (VAACs) provide forecasts on the expected location of the ash in the atmosphere, and in Europe there is an additional requirement to forecast the expected concentration of ash (Civil Aviation Authority, 2017). The Met Office acts as the London VAAC and is responsible for forecasting ash dispersal over northern Europe as shown in Figure 1-1.

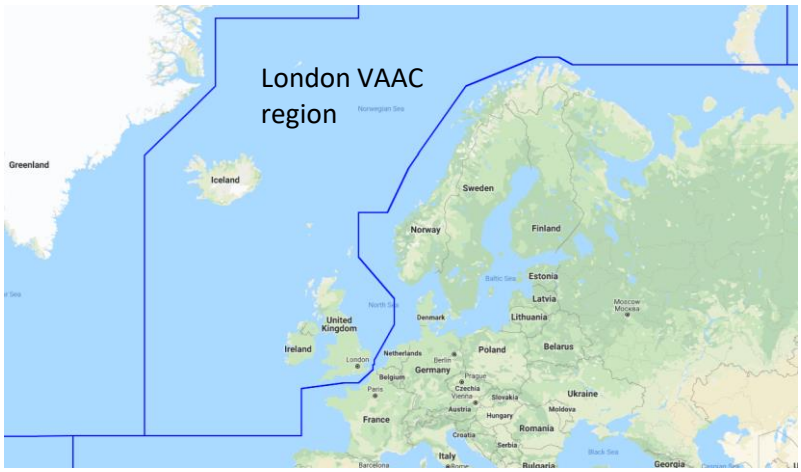

Figure 1-1 Area of responsibility of the London VAAC (www.ospo.noaa.gov/Products/atmosphere/vaac/).

As part of their forecasting process VAACs use atmospheric dispersion models to issue volcanic ash advisories (VAAs) and Volcanic Ash Graphics (VAGs). The models use either a Lagrangian approach, where the paths of individual particles are tracked through space (e.g. NAME, which is used by the London VAAC, and HYSPLIT) or a Eulerian approach where particles pass through a given observation window (e.g. FALL-3D and CANERM) (Wilkins et al., 2016). Models are initialised with a set of parameters which describe the source conditions and include source location, eruption duration, spatial distribution of ash at source and mass eruption rate (MER). Key input parameters describing the characteristics of the particles include size (in the form of total grain size distribution (TGSD)), shape and density. These all affect terminal velocity and influence whether ash remains in the plume or falls out (Beckett et al., 2015). Improving the representation of grain size distribution in

operational modelling is the focus of this project. In particular, this thesis explores how the grain size distributions of phreatomagmatic eruptions (i.e. ones in which external water affects the fragmentation of the magma) compare to those from magmatic eruptions, and tests the sensitivities of NAME (Jones et al., 2007) ash dispersion forecasts to the different grain size distributions.

1.1 Project aims and objectives

The aim of this project is to improve Met Office ash cloud dispersal forecasts, by understanding the differences in grain size distributions (GSDs) between phreatomagmatic and magmatic eruptions, assessing the impact of these distributions on ash dispersal modelling and suggesting default values for modelling eruptions with a range of magma compositions.

The objectives of the project are to:

- Compile published data on grain size variation with distance from source for phreatomagmatic eruptions. Compile similar data for magmatic eruptions, particularly from Iceland, for comparison.
- Identify trends for changes in GSD with distance from source for phreatomagmatic versus magmatic eruptions, e.g. magma composition, eruption magnitude.
- Understand the process of producing GSDs and TGSDs from field data by producing GSDs for Santorini Phase 0 samples and using the Voronoi tessellation technique (Bonadonna and Houghton, 2005) to produce a TGSD from published GSDs.
- To make it easier for NAME runs to use research where GSDs are reported in phi (ϕ) units, create a ϕ scale GSD that is equivalent to the current micron (μm) scale default used for London VAAC forecasting. Compare NAME output for the new scale with the current default.
- Use NAME to model ash dispersal to investigate the sensitivity to input PSDs.
- Recommend default PSDs for modelling dispersal for eruptions with a range of characteristics.

1.2 Terminology: PSD, GSD and TGSD

The term ‘grain size distribution’ is often used when referring to airborne particle concentrations with ‘particle size distribution’ used for both samples collected on the ground and modelled distributions, although the terms are used somewhat interchangeably (e.g. Carey and Sigurdsson, 1982; Hobbs et al., 1991; Bonadonna et al., 2011). In this project, to avoid confusion I have chosen to use ‘particle size distribution’ (PSD) when referring to model distributions and ‘grain size distribution’ (GSD) for sampled deposits (based on particle diameter measurements). Total grain size distribution (TGSD) refers to the best available estimate of the size distribution of the total erupted mass, usually compiled from GSDs at a range of distances from source. If ground-based TGSDs

represent a reasonable input distribution to initialise model runs, then simulations using input PSDs based on published TGSDs enable us to explore the impact of particle size on modelled ash dispersion.

1.3 Phreatomagmatic eruptions

Phreatomagmatism can occur following pre-eruptive mixing of magma with external water (e.g. ground water, crater lakes, glaciers or the sea). For low viscosity, basaltic magma, hydrodynamic mixing prior to eruption can produce sufficient contact area between magma and water to create an explosion (Austin-Erickson et al., 2008; Zimanowski et al., 2015). Experiments to simulate the small hydromagmatic explosion at Kverkfjöll on 15 August 2013 indicate that thermal energy was mainly dissipated as heat, with ~ 30 % converted to mechanical energy. Only minor magma fragmentation occurred, although aggregated particles were broken up (Montanaro et al., 2016).

For silicic eruptions, analysis of pressure gradients shows large amounts of groundwater (> 5 wt %) will only enter the conduit at low MER and even then, conditions are usually only favourable above the level of primary fragmentation. At high MER, surface water is needed, unless caldera collapse or the opening of a conduit disrupts an aquifer and allows water-saturated rocks to interact with magma (e.g. Vesuvius 79 CE, Santorini Minoan eruption) (Aravena et al., 2018; Aravena et al., 2019).

Phreatomagmatic eruptions can produce GSDs that vary little with distance, in contrast to magmatic eruptions where grain size decreases linearly, as shown in Figure 1-2 (Cashman and Rust, 2016). These differences between GSDs for phreatomagmatic and magmatic eruptions have implications for dispersal modelling and are explored further in Chapter 3.

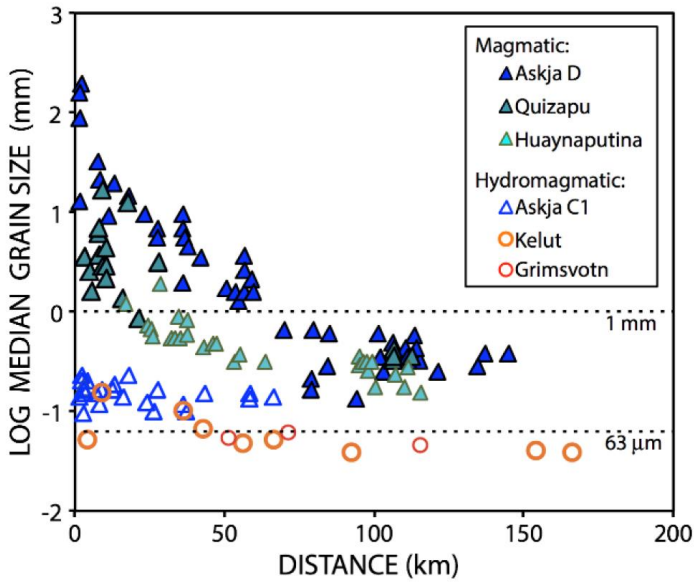

Figure 1-2 Change of median grain size with distance from source (Cashman and Rust, 2016).

1.4 London VAAC and NAME

The London VAAC uses NAME for ash dispersion forecasts (Jones et al., 2007), initialised with eruption source parameters (ESPs) described in Chapter 3. During an eruption, key ESPs are not usually known in real-time and so default values are used for operational forecasting, as shown in in Table 1-1 (Witham et al., 2017).

The assumption of a cuboid source, with ash released uniformly from the vent to the top of the plume, can model the distal ash cloud where near-source conditions are of less interest. However, this may overestimate proximal deposition, as larger model particles fall out from the base of the plume.

Parameter	**Default operational value**	
Source shape	Cuboid, uniform (top hat) distribution of release along entire source region.	
Mass eruption rate	Calculated from plume height using the method of Mastin et al (2009)	
Particle shape	Spherical	
Particle density	2300 kg m-3	
Particle size distribution	Particle size (μm)	Cumulative mass fraction (%)
	0.1–0.3	0.1
	0.3–1	0.6
	1–3	5.6
	3–10	25.6
	10–30	75.6
	30–100	100.0

Table 1-1 Default eruption source parameters used by London VAAC (Witham et al., 2017).

The MER is derived from the empirical relationship between plume height and erupted volume established by Mastin et al. (2009):

$H = 2.00\ V^{0.241}$ (1-1)

where H is the observed plume height above summit (in km) and V is the volumetric flow rate (in m^3 dense rock equivalent s^{-1}), calculated from field data, assuming tephra density of 2500 kg m^{-3}. For the Eyjafjallajökull 2010 eruption, the MER on 8 – 10 May was estimated at 2.2 – 3.5 x 10^4 kg s^{-1}, using video analysis of eruptive pulses (Dürig et al., 2015) and this is consistent with values calculated from plume heights, using the Mastin equation, of 3.7 x 10^4 kg s^{-1} . However, research

using buoyant plume models suggests that the Mastin approach underestimates the MER of weak plumes bent over by the wind, as was the case for this eruption (Costa et al., 2016; Devenish, 2016).

TGSDs vary depending on eruption style and magma fragmentation conditions (Houghton and Carey, 2015) and because the fall velocity of an erupted particle is most sensitive to its size, it is important to select a GSD that is appropriate for each eruption. Particle shape and density are also important and sensitivity to shape increases with particle size, with non-spherical, lower density particles remaining airborne longer (Saxby et al., 2018) . When modelling the Eyjafjallajökull 2010 eruption, the terminal velocity of 30 µm particles was only ~ 12 % that of 100 µm particles. In addition, modelled 100 µm particles with measured densities and sphericities, travelled up to 84 % further than those with the default characteristics (Beckett et al., 2015). This project focuses on TGSD and investigates the impact of different input distributions on the modelled ash plume.

1.5 Structure of this thesis

Chapter 2 reviews methods of compiling TGSDs and details work undertaken to understand the processes of obtaining GSDs from field data and compiling a TGSD. The chapter describes the compilation of GSDs using samples from Phase 0 of the Late Bronze Age eruption on Santorini. Although this work used only a few samples, it improved my understanding of the difficulties associated with collecting field samples and gave me a better appreciation of the limitations of the data used in my NAME modelling. This chapter also explains the process of using the TOTGS package (Biass and Bonadonna, 2014) to obtain an apparent TGSD, using the phreatomagmatic Kelut 1919 eruption as a case study. Again the data for this work are sparse, but it helped in my understanding of the data required to compile a TGSD and the implications of using an incomplete data set. Finally this chapter details my analysis of a sample from the Askja 1875 eruption to extend the dataset of median values at a range of distances from source.

Chapter 3 is written as an article which will be submitted to the Journal of Volcanology and Geothermal Research. It describes the compilation of published TGSDs for phreatomagmatic plus sample magmatic eruptions and comparison of modelled ash dispersion from NAME model simulations using a range of input PSDs. Finally it makes recommendations for default PSD values to simulate a range of eruptions and identifies future work. Because the article is self-contained, it necessarily contains some repetition of points covered in Chapter 1.

Chapter 4 summarises what I have learned during this project and highlights its conclusions and thoughts on future work. A glossary of terms is included at the end of the thesis.

Chapter 2 Methods of determining GSDs and TGSDs

The total grain size distribution (TGSD) of an eruption is a key input parameter for volcanic ash dispersion models as erupted particles are sorted by size during transport (Mastin et al., 2009; Macedonio et al., 2016). Because many Icelandic volcanoes erupt from beneath glaciers e.g. Grímsvötn 2011 (Olsson et al., 2013), it is important to understand any differences in the grain size distribution (GSD) of tephra from phreatomagmatic versus magmatic eruptions.

For magmatic eruptions, GSDs become more fine-grained with increasing distance from the vent as larger particles preferentially fall out, and so grain size data at a range of distances from the source are needed to enable the TGSD of an eruption to be estimated (Rust and Cashman, 2011). The mass of the coarsest and finest particles is often underestimated and reliable TGSDs require extensive sampling from well-preserved deposits, both proximally and distally (Spanu et al., 2016; Pioli et al., 2019). In simulations of a synthetic deposit with a known TGSD, based on the 2450 BP eruption of Pululagua in Ecuador, a widespread sampling strategy (Figure 2-1a) was found to reconstruct the input TGSD most closely, with sampling on downwind or downwind and crosswind transects less effective (Figure 2-1b and c) and sampling only crosswind always producing errors > 30 % (Pioli et al., 2019).

Phreatomagmatic eruptions often do not show this fining trend with distance from source, possibly because of more efficient initial fragmentation conditions (Liu et al., 2017) or distinct sedimentation processes including aggregation (e.g. Stevenson et al., 2013; Mueller et al., 2018) or *en masse* sedimentation of fine particles as shown in Figure 2-2 (e.g. Koyaguchi and Ohno, 2001; Carazzo and Jellinek, 2013; Manzella et al., 2015).

2.1 Compilation of GSDs and TGSDs

GSDs are traditionally compiled from field samples, sieved into whole-Φ or half-Φ bins. The Φ scale was developed to allow more systematic analysis of sediment size distributions, by using class intervals of equal size (Krumbein, 1936). Φ is defined in equation 2-1, where D is the particle size in mm, and D_o is a reference value of 1 mm to make the equation internally consistent (e.g. de' Michieli Vitturi et al., 2015).

$$\Phi = - \log_2 (D/D_0) \qquad (2\text{-}1)$$

More recently fine fractions are analysed optically, for example by laser diffraction using a Malvern Mastersizer (e.g. Verolino et al., 2018) or digital image analysis using a Retsch Camsizer (e.g. Poret et al., 2018), but results are often reported in Φ-scale bins, to allow comparison with earlier published research.

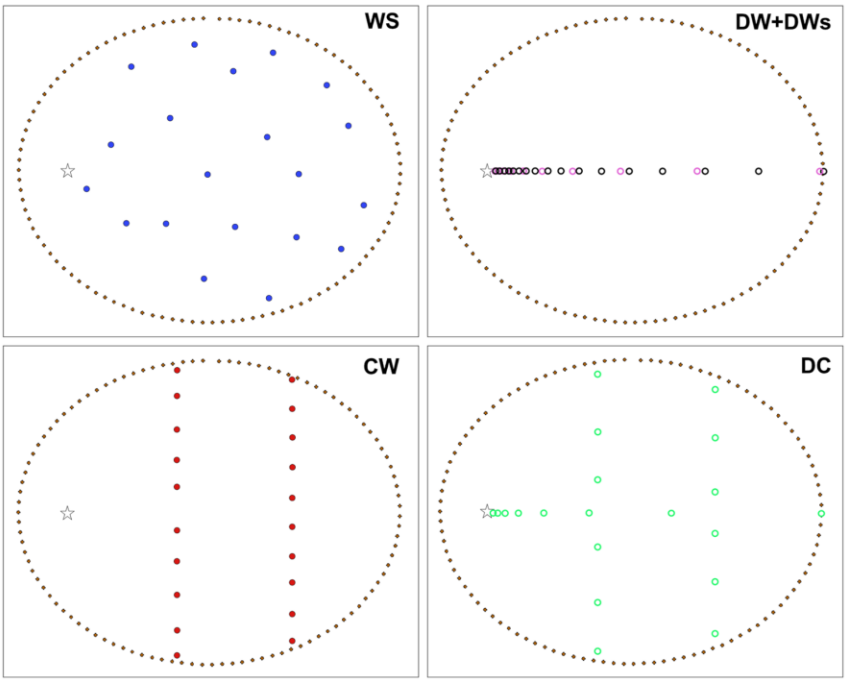

Figure 2-1 Sampling strategies for deposit from simulated eruption with 10 km plume height and 10 m s^{-1} maximum wind speed. ☆= vent, coloured dots = sampling points, black dots enclose deposit area. Sampling strategies: WS = Widespread, DW + DWs = Downwind + Downwind with 10 sampling points, CW = Crosswind (Pioli et al., 2019).

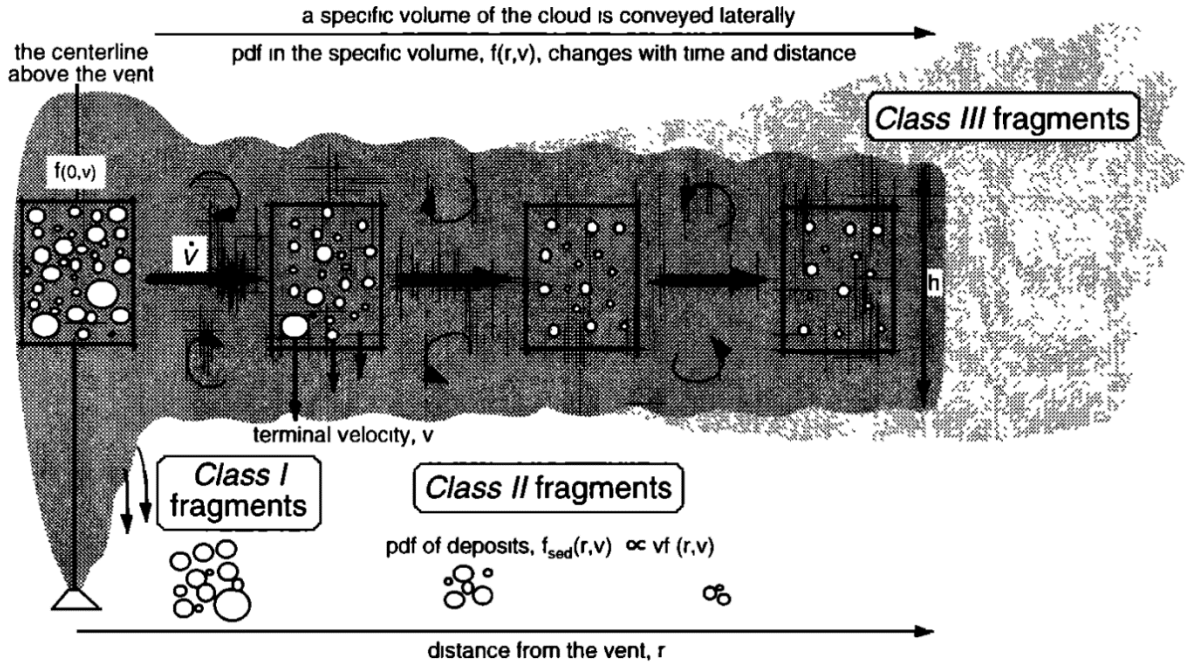

Figure 2-2 Schematic illustration of impact of particle size on fallout. Class I fragments are large particles that fall out close to source; Class II fragments are homogenised by turbulence in the plume and fall out as individual particles from the bottom of the plume at their terminal velocity; Class III fragments are very fine particles, with terminal velocities less than turbulent velocities in the plume, that are carried long distances (Koyaguchi and Ohno, 2001).

Several methods have been used to calculate TGSD, using GSDs compiled from field samples collected at a range of distances from the source, including:

- Weighted average of GSDs within isopachs (Murrow et al., 1980; Sparks et al., 1981). This technique is unsuitable if the distribution of sampling sites is not uniform (Bonadonna and Houghton, 2005).
- Weighted average of GSDs within sectors, defined using expert judgement. This has been used where averaging within isopachs would not adequately represent changes in GSD with distance from source (e.g. Carey and Sigurdsson, 1982).
- Voronoi tessellation, a statistical technique that removes the need for expert judgement to define sectors (e.g. Bonadonna and Houghton, 2005). The deposit area is divided into polygons around the sampling sites, such that all points within a polygon are closer to the enclosed sampling site than any other, and the TGSD is calculated as an average, weighted by area, over all the polygons. A Matlab code is available to calculate TGSD using this technique (Biass and Bonadonna, 2014).

To gain a better understanding of GSD measurement and TGSD determination, I collected and analysed samples from Phase 0 of the Minoan eruption on Santorini (described in Section 2.2 below). I compiled GSDs for both phreatomagmatic and magmatic deposits and compared my results with published data (Cioni et al., 2000). I also used published grain size data from the 1919 phreatomagmatic eruption of Kelut to compile a TGSD (described in Section 2.3 below), using the TOTGS Matlab code (Biass and Bonadonna, 2014).

Where GSDs are not available, median grain size can also give an indication of how grain size changes with distance from source (Section 3.2.3 gives more detail). Section 2.4 describes my analysis of a sample of the phreatomagmatic phase C of the 1875 eruption of Askja Volcano for comparison with published median data for other samples of this eruption. This sample, found in the University of Bristol store, appears to have been part of the study of the eruption by Sparks at al. (1981) but was not analysed for the original paper.

2.2 GSDs from samples collected in Santorini

Deposits from the main phases of the Late Bronze Age Plinian eruption of Santorini are well documented (Section 2.2.2), but the precursory Phase 0 is less studied. This sub-Plinian eruption provides a good opportunity to investigate changes in grain size from phreatomagmatic to magmatic activity for a sub-Plinian eruption.

2.2.1 Geological setting

Santorini is located in the Aegean Sea, 120 km north of Crete on the Hellenic Volcanic Arc (Figure 2-3), where the African plate is subducting to the north-east beneath the Aegean microplate (Flaherty et al., 2018). The tectonic setting is complex, with active NE-SW trending normal faults indicating back arc extension. Santorini sits at the northern edge of the Santorini-Christiana-Amorgos rift zone on continental crust around 25 km thick (Druitt et al., 1999; Druitt, 2014; Hooft et al., 2017).

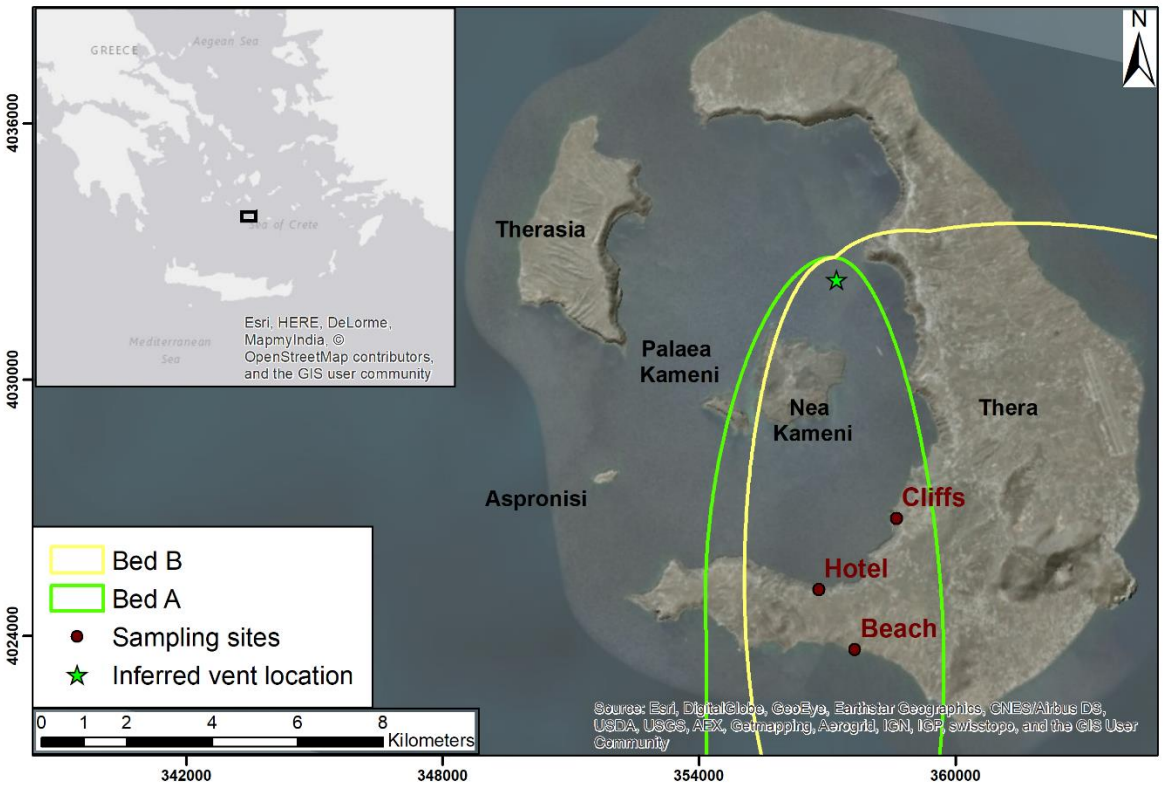

Figure 2-3 Location of sampling sites on Santorini and inferred vent location for Phase 0 of Minoan eruption (Heiken and McCoy, 1990)**.**

The basement rocks are Triassic limestones and Paleocene to Eocene schists and phyllites. Effusive volcanism began ~ 650 ka, with the oldest volcanic rocks found on the Akrotiri peninsula. The Peristeria composite stratovolcano developed in the north of Santorini from 530—430 ka and explosive volcanism started ~ 360 ka. Two eruptive cycles have occurred from 360— 180 ka and 180—3.6 ka, with explosive eruptions becoming increasing silicic during each cycle and ending with caldera collapse. In total, 12 Plinian eruptions have occurred at 17—45 ka intervals, most recently the Late Bronze Age (Minoan) eruption ~ 3600 years ago (Druitt et al., 1999; Vespa et al., 2006).

Today, the Santorini island group consists of five islands: Thera, Therasia and Aspronisi form the edge of a steep-walled caldera, which has a maximum depth of 390 m and cliffs rising to 300 m

above sea level; Palaea and Nea Kameni have been formed by intracaldera volcanism dating back to at least 46 CE (Nomikou et al., 2014). Small relatively frequent eruptions at Nea Kameni indicate a volatile-poor magma body ~ 10 km^3, at 3 – 6 km depth. Six eruptions have occurred over the past 450 years, with the most recent effusive eruption in 1950 (Degruyter et al., 2016).

2.2.2 Minoan eruption

Stromatolites found in Minoan Tuff and cosmic ray exposure dating of the current caldera cliffs indicate that, prior to the Minoan eruption, a shallow, flooded caldera occupied (at least) the northern part of the current caldera (Friedrich et al., 1988; Athanassas et al., 2016). The eruption is estimated at VEI 7 and produced 117— 129 km^3 bulk volume (3—86 km^3 dense rock equivalent) of rhyodacitic magma. However this is poorly constrained and is a maximum value based on estimating the volume of intracaldera fill from Phases 2 and 3 accommodated by downfaulting during caldera collapse (Johnston et al., 2014; Johnston et al., 2015; Flaherty et al., 2018; Karátson et al., 2018).

The date of the eruption has been estimated from ^{14}C dating of seed assemblages and olive branch segments buried in the fall deposit at the ancient city of Akrotiri, in southwest Thera. Recent revisions, using annual rather than decadal ^{14}C time series, suggest the eruption occurred between 1664 and 1511 BCE (with 95 % confidence) (Pearson et al., 2018), compared to previous estimates of 1636 – 1600 BC (Manning et al., 2014 and references therein).

The eruption consisted of 5 phases:

- Phase 0 was sub-Plinian, from a vent north east of the present island of Nea Kameni (Figure 2-3). Deposits up to 10 cm thick were dispersed to the south-southeast from a plume 7 – 10 km high (Heiken and McCoy, 1990; Cioni et al., 2000).
- Plinian Phase 1 produced fallout up to 5.5 m thick, from same vent as Phase 0. Dispersal was initially south-southeast and then southeast or east-southeast (Bond and Sparks, 1976; Cioni et al., 2000; Druitt, 2014).
- Phases 2 and 3 produced pyroclastic surge then flow deposits from phreatomagmatic activity, as the vent migrated northwards into the flooded caldera from the previous Plinian eruption of ~ 22 ka (Pfeiffer, 2001; Druitt, 2014).
- Phase 4 resulted in high temperature (up to 400 °C) pyroclastic flow deposits covering the whole island. Magmatic activity occurred from subaerial vents with syn- or post-eruptive caldera collapse (Druitt, 2014).

Phase 0 lasted 30 to 40 minutes and deposits consist of three subunits which indicate oscillations between wet and dry conditions. Bed A_l is lithic-rich coarse ash, up to 2 cm thick from a

phreatomagmatic explosion and there is then a gradational change to magmatic conditions and deposition of pumice-rich lapilli (Bed A_p). A final phreatomagmatic pulse produced Bed B, which consists of yellowish, fine to coarse ash which is often indurated. Sampling locations for these beds are shown in Table 2-1. In Akrotiri, there is evidence of earthquake damage and restoration work before and during fall deposits from Phases 0 and 1, suggesting syn-eruptive seismic activity (Cioni et al., 2000). The bed previously identified as a fourth subunit of Phase 0 has now been re-categorised as the onset of Phase 1 (Heiken and McCoy, 1990; Cioni et al., 2000).

2.2.3 Field sampling in Santorini

Phreatomagmatic and magmatic samples were collected from Phase 0 at 3 sites as shown in Table 2-1 and Figures 2-3 and 2-4.

Site	**Location**	**Distance from vent (km)**	**Description**
Cliffs	Lat: 25. 42388889 Long: 37555556	~ 5.7	Cliff exposure. Phase 0 consists of indurated Bed B, up to 10 cm thick, overlain by Phase 1 deposit.
Hotel	Lat: 25.40388889 Long: 36.36027778	~ 7.3	Cliff exposure. Underlying paleosol contains pottery shards. Total thickness of Phase 0 deposit is ~ 10 cm comprising Beds A_L, A_P and B, overlain by Phase 1 deposit. Problems with sampling included: • Difficulty in extracting finest material. • Contamination from loose material in overlying Phase 1 bed.
Beach	Lat: 25. 41361111 Long: 36. 34777778	~ 8.7	Cliff exposure on seashore. Bed B is indurated, up to 10 cm thick and overlain by Phase 1 deposit.

Table 2-1 Location and description of Phase 0 sampling sites in Santorini.

2.2.4 Methods

Indurated samples from Bed B were separated using an ultrasonic bath; then all samples were oven-dried and manually sieved using half-Φ sieves from -6 ϕ to 3 ϕ. Material finer than 3 ϕ was analysed using the X-jet module (air pressure dispersion) of a Retsch Camsizer. This uses dynamic image analysis, where multiple images of a particle's trajectory are used to identify its terminal velocity and dimensions (British Standards Institution, 2006). A dispersion pressure of 75 kPa was selected, as it was high enough to avoid particles clumping, but not so high as to split the grains.

Figure 2-4 Phase 0 sampling sites in Santorini. a. Cliffs site ~ 6 km from vent. b. Hotel site ~ 7 km from vent. c. Beach site ~ 9 km from vent. Location of sites is shown in Figure 2-3 and Table 2-1.

A GSD (in half-Φ bins) was compiled for each sampling location and these were compared with the results from the first comprehensive survey of Phase 0 by Cioni et al. (2000). Because it was difficult to sample the different Phase 0 beds at the Hotel site without getting contamination from the overlying Phase 1 bed, that bed was sampled as well, to help identify any contamination in the Phase 0 samples.

2.2.5 Results

Figures 2-5 a and b show GSDs for beds A_L and A_P from the Hotel site. A_P shows very good agreement with the Cioni et al. (2000) sample from the same site, while A_L has a higher weight % in the 0 and 1 Φ bins, and lower weight % in the -1 Φ bin. Some coarser material may have come from the overlying Phase 1 bed (Figure 2-6) and the lack of the finest material is probably the result of sampling difficulties.

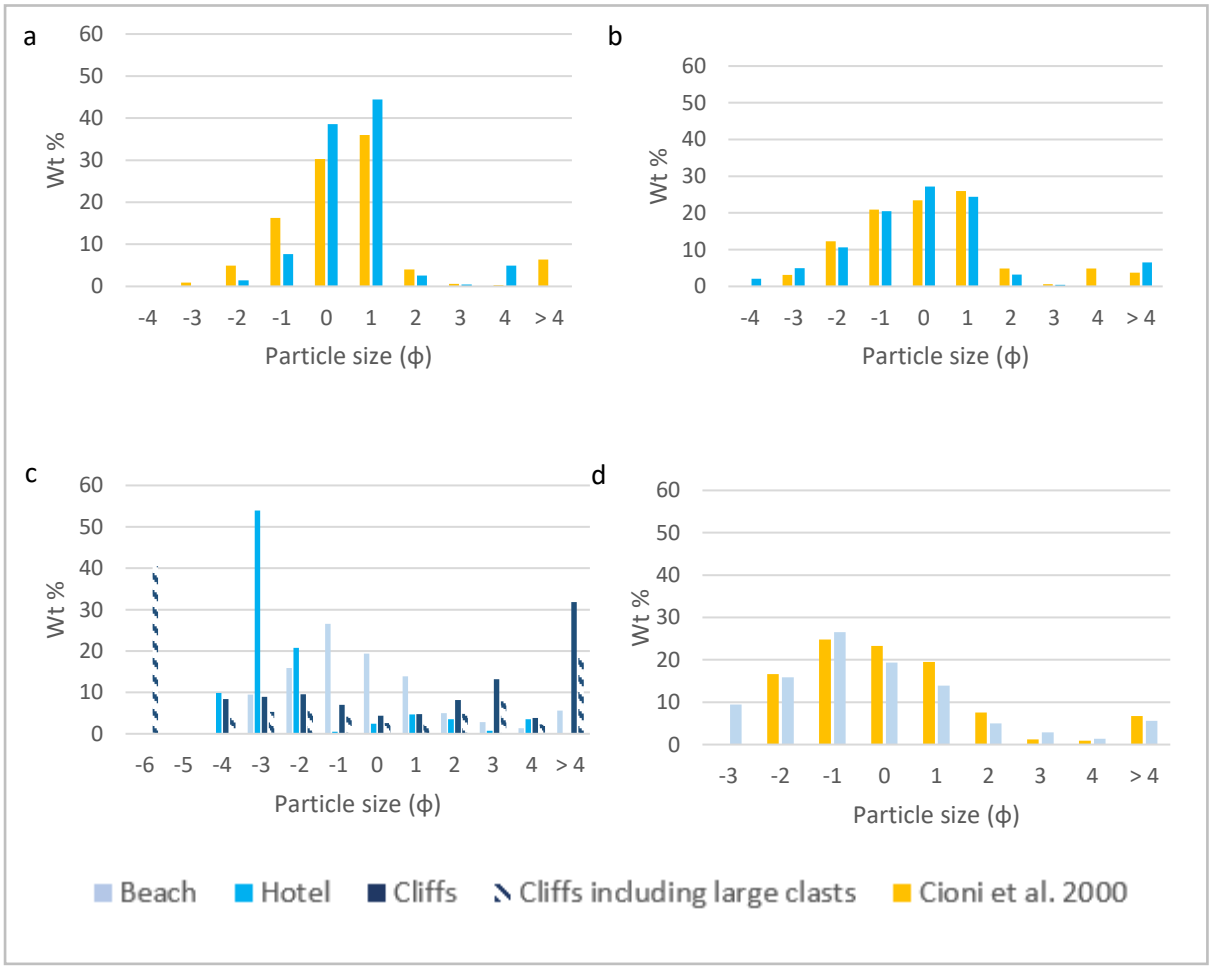

Figure 2-5 Grain size distributions for Santorini Phase 0 samples. a. Bed A_L. b. Bed A_P. Results are compared with Cioni et al. (2000).c. Bed B for 3 sampling sites. d. Comparison of Bed B beach site results from this study with Cioni et al. (2000).

The three samples of Bed B (Figure 2-5 c) show a wide range of GSDs, with the Beach sample (~ 9 km from the probable vent location (Heiken and McCoy, 1990) most closely matching the earlier study (Figure 2-5 d). This sample was indurated and heavily impregnated with salt, which may have reduced contamination from upper beds and erosion of particles. The Hotel sample (~ 7 km from the vent) showed a higher concentration of coarser particles, probably from the overlying Phase 1 bed. The more proximal Cliffs sample (~ 6 km from the vent) contained a much higher fraction of large clasts, as expected closer to source, and also of fines, which may have filtered down from overlying beds. Figure 2-7 shows the cumulative GSDs for all samples.

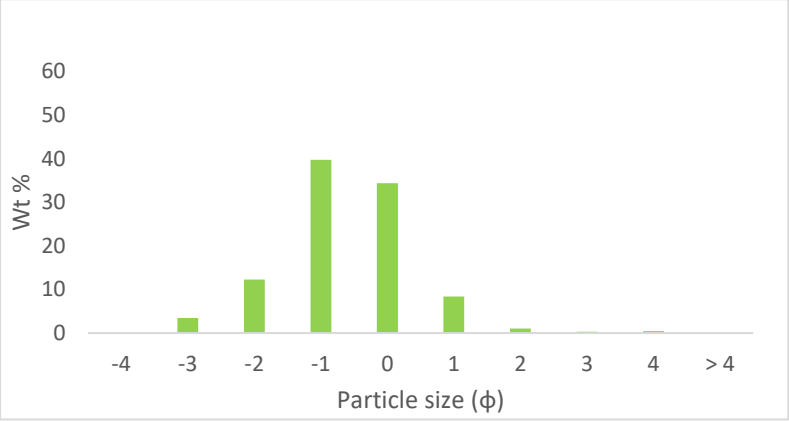

Figure 2-6 Grain size distribution for Santorini Phase 1 bed overlying the Phase 0 samples at the Hotel site. This sample was taken to identify contamination in the Phase 0 samples.

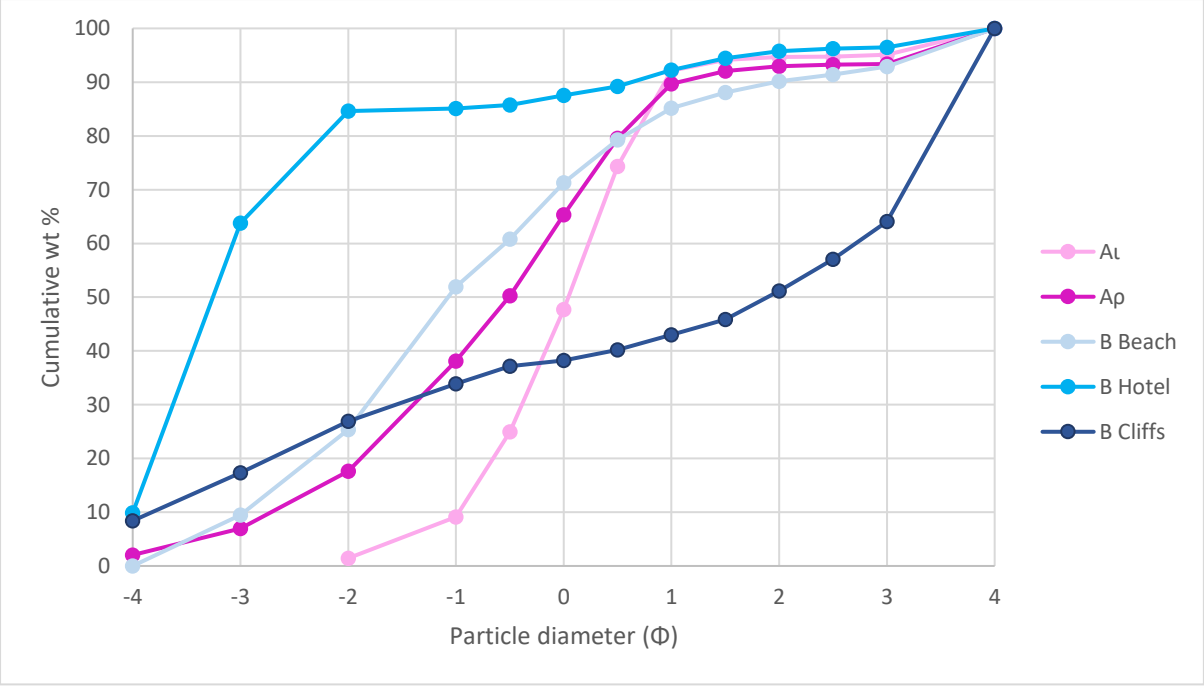

Figure 2-7 Cumulative grain size distribution for Santorini Phase 0 samples.

2.2.6 Discussion

Despite some sampling issues, my results show good agreement with earlier research (Cioni et al., 2000) and indicate three distinct beds formed during Phase 0 of the Minoan eruption. The finer GSD for Bed A_L compared to the overlying Bed A_P, is consistent with a move from phreatomagmatic to magmatic conditions.

2.3 TGSD for Kelut 1919

To better understand the process of compiling a TGSD by Voronoi tessellation, I used the TOTGS script run on Matlab (Biass and Bonadonna, 2014) to create a TGSD for the Kelut 1919 eruption. The dataset is sparse and the result only shows an apparent TGSD for particles ≤ 2 mm diameter, as there are insufficient data on larger grains. I have also made lots of assumptions, described in detail in Sections 2.3.2 and 2.3.3. Therefore, the result is not robust but the process helped me to understand how TGSDs are obtained from field data.

2.3.1 Geological setting

Kelut volcano, in eastern Java, Indonesia (Figure 2-8 a), erupts frequently, with 35 known eruptions since 1000 CE (Goode et al., 2018). The devastating VEI 4 phreatomagmatic eruption on 19—20 May 1919 drained the crater lake (containing an estimated 3.8×10^{10} litres of water) and the resulting lahar led to over 5000 deaths in nearby villages (Mohr and van Baren, 1954). The eruption produced 0.1 km^3 of basaltic andesite—andesite tephra and ash was deposited in two separate areas, one east and one west of the volcano. This was interpreted as being due to local wind patterns, with low altitude monsoon winds carrying ash to the west, and the prevailing trade winds above 6.5 km transporting ash to the east (Mohr and van Baren, 1954; Crosweller et al., 2012).

2.3.2 Data from field studies

Extensive field work, carried out after the 1919 eruption, is reported in Mohr and van Baren (1954) and the ash deposit was estimated to extend over 500 km west of Kelut (Figure 2-8 b). For this deposit, measurements included tephra thickness, particle density and GSDs at 2—360 km from source (Figure 2-8 b and c). Deposition east of the volcano was not considered as no thickness data was available for this deposit.

Tephra thickness was reported at four sites, with locations identified by elevations (Table 2-2) and GSDs were reported at eight sites for particles ≤ 2 mm diameter, with locations reported as distance from source (Table 2-3). One GSD, at 36 km from source, had a total mass fraction of 105.7 % and I excluded this from further calculations, as no other information is given to identify the source of error. Deposit density values range from 0.260—0.100 kg m^{-3} as shown in Table 2-4. In all cases I have assumed that the measurements were taken downwind of the source. If samples were

collected off-axis, it is likely that the TGSD will underestimate the proportion of larger grains, which will have travelled further than the samples will suggest.

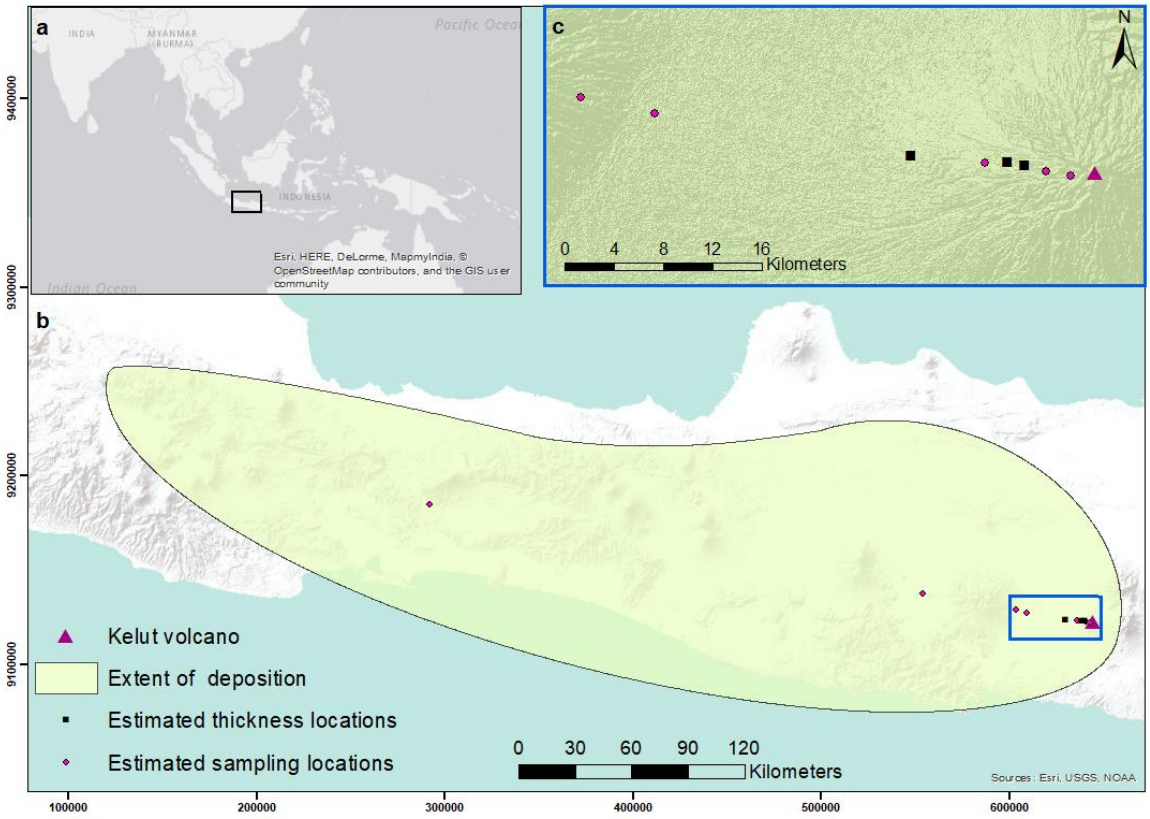

Figure 2-8 Location of sampling sites on Kelut volcano. a. Location of Kelut in eastern Java, Indonesia. b. Extent of deposition west of Kelut, following 1919 eruption, locations where ash thickness was measured and sampling sites for grain size analysis. c. Detail of proximal sampling sites (Mohr and van Baren, 1954).

Elevation (m)	Deposit thickness (mm)
Crater rim	450
800	250
700	200
350	130

Table 2-2 Elevation and thickness data for Kelut 1919, western deposit (Mohr and van Baren, 1954).

Grain size bin (µm)	Distance from source (km)							
	2	**4**	**9**	**36**	**36**	**42**	**92**	**360**
1000—2000	10.3	0.5	0.2			0.1		
500—1000	11.3	3.0	1.3	0.1		0.2		
200—500	47.4	16	35.7	19.8	6.2	6.5	0.1	
100—200	8.4	11.8	25.4	19.2	3.8	9.1	1.5	0.6
50—100	10.2	21.7	8.5	21.5	36.9	27.2	36.7	13.5
20—50	3.9	24.4	15.3	15.4	32	23.8	32.3	80.7
5—20	4.3	17.3	8.9	17.7	21.3	26.7	22.4	2.9
2—5	1.8	3.2	3	2.8	3.5	3.8	4.0	1.1
0.5—2	0.8	1.4	1.4	1.0	1.6	1.4	2.1	0.4
< 0.5	1.2	0.6	0.2	0.5	0.4	1.4	0.6	0.3
Total	99.6	99.9	99.9	98	105.7	100.2	99.7	99.5

Table 2-3 Mass fraction by binned grain size for particles ≤ 2 mm diameter in samples collected at 2—360 km from source (Mohr and van Baren, 1954 Table 76).

Grain size (µm)	Phi equivalent	Density of freshly deposited ash sample (kg m^{-3})
3000—200	-1.5—2	0.260
200—50	2—4.5	0.150
< 50	> 4.5	0.100

Table 2-4 Deposit density (edited from Mohr and van Baren, 1954 Table 75).

2.3.3 Methods

To identify how far from source the thickness measurements were taken, I used ArcGIS to create contours from a USGS SRTM 1 arc-second (~ 30 m resolution) digital elevation model of eastern Java (https://earthexplorer.usgs.gov/). I then located the sampling sites on the appropriate contour, as shown in Figure 2-9, and measured the distance from source. I assumed the crater rim site was 1 km from source.

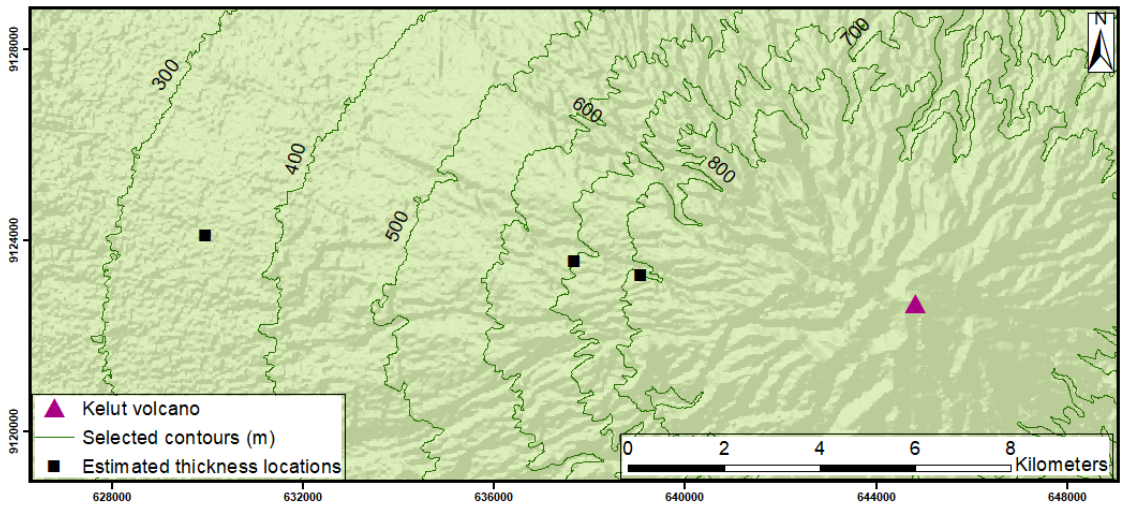

Figure 2-9 Area downwind of Kelut volcano showing selected height contours and the estimated location of thickness sampling sites.

Because no thickness measurements were available at distances > ~ 15 km from source, I made some assumptions for the distal deposit. Ash thickness at 360 km from source had been sufficient for a GSD to be compiled from the sample, at 500 km from source 'only a very thin layer [of ash] was perceptible' and the deposit envelope (Figure 2-8 b) shows the distal extent of deposition being ~ 540 km (Mohr and van Baren, 1954). Based on this information, I took the thickness at 360 km as 5 mm, and at 500 km as 1 mm.

I plotted the measured and assumed thickness values on a semi-log plot of thickness vs distance from source and identified 2 sectors (proximal to ~ 15 km and > 15 km). I assumed exponential thinning so thickness trends could be plotted as straight lines (Pyle, 1989) as shown in Figure 2-10. I was then able to calculate thickness values for each GSD sampling site.

I converted each GSD from the reported µm-scale bins to whole-Φ bins, assuming particle size is uniformly distributed within each bin (Table A-1). In addition, I allocated all particles finer than 0.5 µm to the 12 ϕ bin (0.24—0.49 µm). I also calculated a bulk density at each sampling site using the mass fractions and density values from tables 2-3 and 2-4. By multiplying this by the thickness at each site I obtained the accumulation at each site (in g m^{-2}) required to calculate TGSD using the TOTGS software (Biass and Bonadonna, 2014).

The other input required for TOTGS is the location of zero mass points, to constrain the Voronoi polygons. I used ArcGIS to optimise the location of these points to obtain the best fit tessellation with the deposit footprint. Using only the original 7 sites, the fit was not good at medial distances (Figure 2-11 a) so I added a synthetic datapoint at 220 km from source, a process used by Alfano et

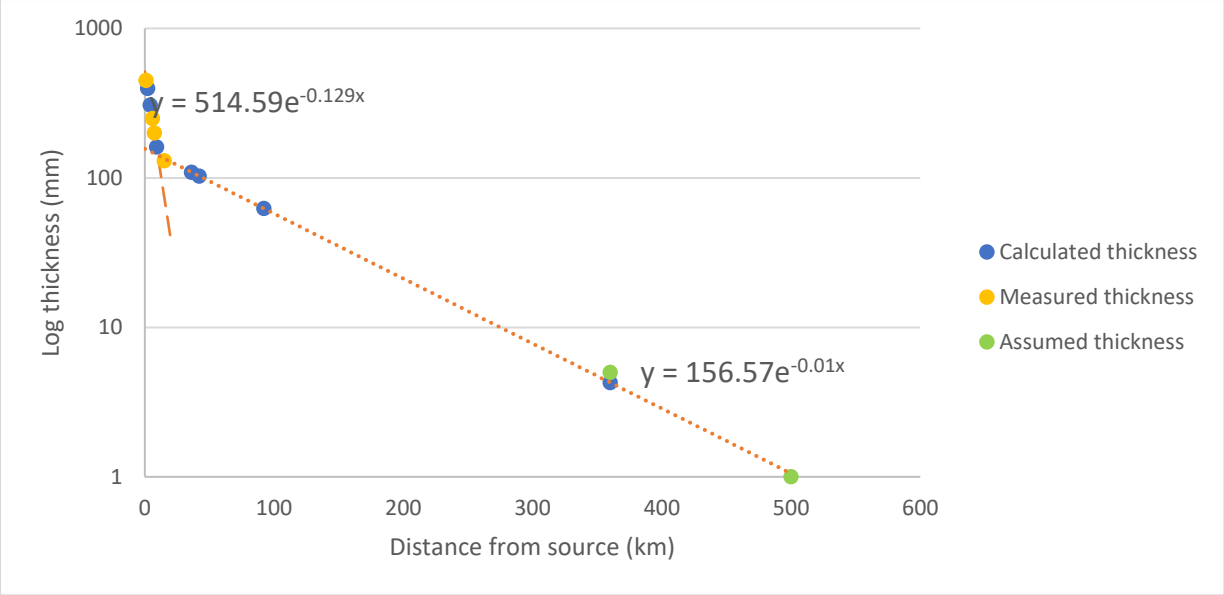

Figure 2-10 Semi-log plot of thickness vs distance from source showing exponential thinning over 2 sectors**.**

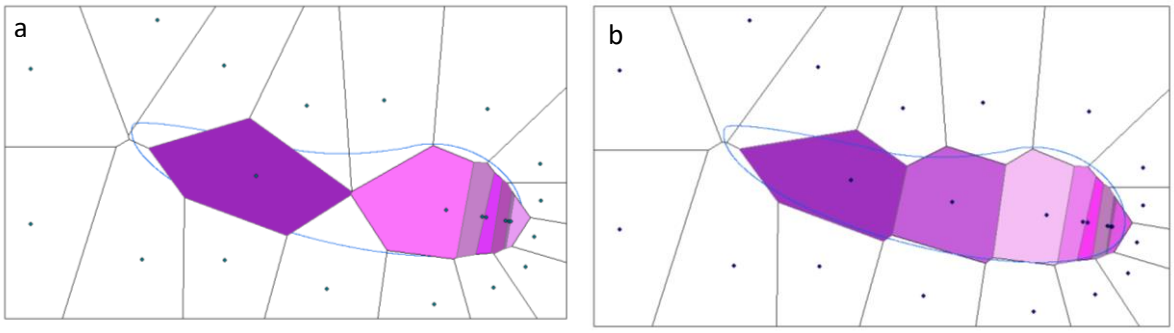

Figure 2-11 Identification of zero mass points to provide best fit of Voronoi tessellation with deposit footprint, for input to TOTGS software. a. Using only data points from Mohr and van Baren (1954). b. With additional synthetic datapoint at 220 km from source.

al. (2016) when producing a TGSD for the Chaitén 2008 eruption. I calculated grain size and density values by interpolating between the 92 km and 360 km sites, assuming uniform change with distance (Table A-1). This provided a better fit as shown in Figure 2-11 b. The GSD dataset input to TOTGS is shown in Table A-2.

2.3.4 Results

Figure 2-12a shows the Voronoi tessellation results from TOTGS and Figure 2-12b shows the resulting TGSD, which has a bimodal distribution with modes at 2 and 5 ϕ. However, this may be an artefact of the sparse sampling, as found by Alfano et al. (2016).

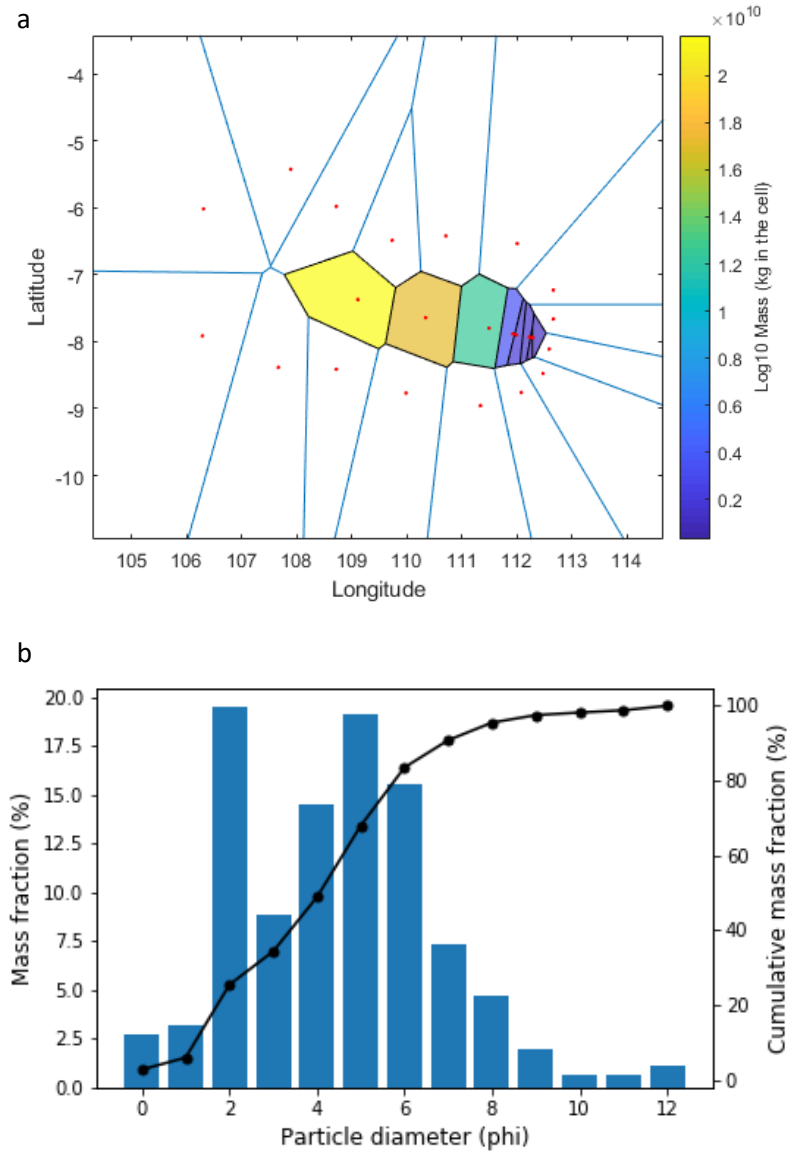

Figure 2-12 Results from TOTGS (Biass and Bonadonna, 2014) for Kelut 1919 eruption using data from Mohr and van Baren (1954). a) Voronoi tessellation. b) Total grain size distribution for particles ≤ 2 mm diameter (Φ bins 0—12).

2.3.5 Discussion

It is, of course, not possible to produce a robust TGSD from 7 GSDs and only very proximal thickness data. However, the Kelut 1919 apparent TGSD produced from this work, normalised to 125 µm, is consistent with other published phreatomagmatic TGSDs, particularly the larger eruptions (VEI ≥ 4) of Taupo 130 CE Rotongaio and Oruanui 25.4 ka BP, as shown in Figure 2-13. In particular it provides evidence of a finer-grained GSD than seen in other (smaller) basaltic phreatomagmatic eruptions, suggesting that the largest mafic eruptions may be capable of producing fine-grained TGSDs more usually associated with silicic eruptions. However, it should be noted that a different result may have been obtained if deposition east of the volcano, likely from a higher part of the plume, had also been

considered. In addition, a complete TGSD would require data on larger particles (> 2 mm), but this would then allow a more detailed comparison with other eruptions.

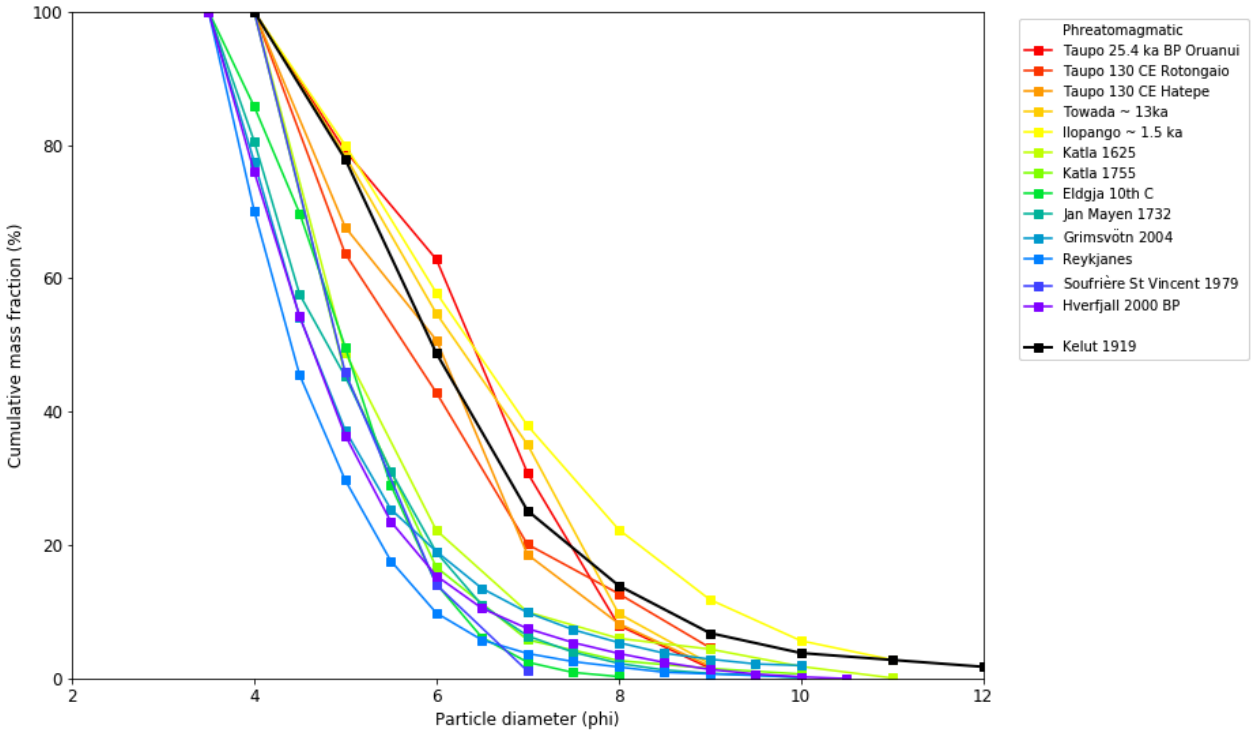

Figure 2-13 Phreatomagmatic TGSDs normalised to 125 µm, including TGSD for Kelut 1919 eruption calculated in this work.

2.4 Analysis of Askja 1875 sample

The Askja 1875 eruption is described briefly in Section 3.3. Published data on samples from this eruption include median grain sizes at a range of distances from source for both Phase C (phreatomagmatic) and Phase D (magmatic) (Sparks et al., 1981). The median provides a stable measure of grain size, little influenced by extreme values (Bonadonna et al., 2013), and the Askja 1875 dataset allows a rare grain size comparison to be made for wet and dry phases of the same eruption.

Sample AS82 from phreatomagmatic Phase C is held in the University of Bristol sample store (marked as 'Distal Askja phreatopl, 110 km from source'), but the median grain size for this sample is not shown in the published data, which includes medians ≤ 70 km from source (Sparks et al., 1981). I re-weighed the sample (in Φ bins) and found the median grain size to be between 2 and 3 Φ as shown in Table 2-5. I then calculated the median grain size (i.e. grain size at 50 % mass fraction):

$$Median\ (\Phi\ ) = \Phi 1 + \frac{(50 - \%\ mass\ in\ \Phi 1\ bin)}{(\%\ mass\ in\ \Phi 2\ bin - \ \%\ mass\ in\ \Phi 1\ bin)}$$

where *Φ1* is largest Φ value with mass fraction < 50 and *Φ2* is smallest Φ value with mass fraction > 50

= 2 + (50 - 41.09)/(65.98 – 41.09) = 2.36

This sample provides an important distal data point, showing that the relatively constant relationship with distance in the published data seems to extend further from source, as shown in Figure 2-14. The data point is also included in further discussion of Askja 1875 and changes of grain size with distance in Section 3.5.

Original bin (mm)	Bin (Φ)	Mass (g)	Cumulative mass fraction (%)
1	0	0.17	2.50
½	1	0.94	16.35
¼	2	1.68	41.09
1/16	3	1.69	65.98
< 1/16	> 3	2.31	100
Total mass		6.79	

Table 2-5 GSD for Askja 1875 Phase C sample AS82 collected 110 km from source (Sparks et al., 1981).

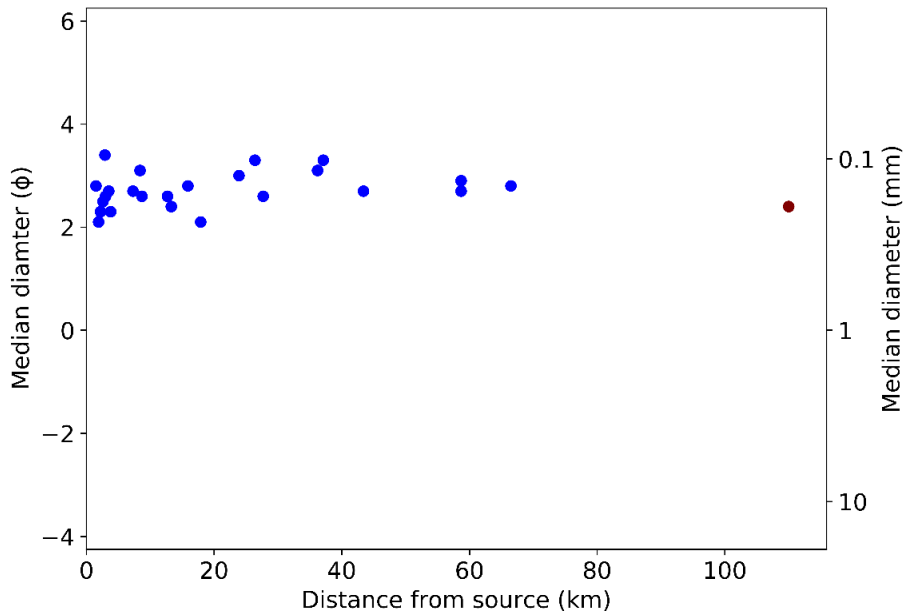

Figure 2-14 Change of median grain size with distance from source for Askja 1875 Phase C, including new data point 110 km from source (Sparks et al., 1981).

Chapter 3 Understanding grain size distributions and their impact on ash dispersal modelling

This chapter is written as an article for submission to the Journal of Volcanology and Geothermal Research. I collected the published grain size distributions, undertook all the analysis including NAME simulations, plotted the results using Python and wrote this chapter. Alison Rust and Frances Beckett supervised my project and provided feedback on the text. Jen Saxby helped with setting up NAME through JASMIN.

3.1 Introduction

The dispersion of volcanic ash through the atmosphere can cause severe disruption to air traffic around the globe, as seen following the Eyjafjallajökull eruption in 2010 (e.g. Budd et al., 2011). Jet engines can fail when ash particles are ingested, as ash can melt on turbine blades or block the cooling system (e.g. Casadevall, 1994; Giehl et al., 2017; Song et al., 2019). To mitigate against aircraft encounters with ash clouds, Volcanic Ash Advisory Centres (VAACs) provide forecasts on the extent of ash in the atmosphere, and the VAACs in Europe also forecast expected ash concentrations (Civil Aviation Authority, 2017). The Met Office acts as the London VAAC and is responsible for providing civil aviation forecasts of ash dispersal over northern Europe, including Iceland.

When modelling ash dispersion, the total grain size distribution (TGSD) is a key parameter because the sedimentation rate of a particle is controlled by its size. Hence the distribution chosen to initialise a model has a significant impact on both the extent of the modelled plume and ash mass loadings within it (Beckett et al., 2015). TGSD varies greatly between eruptions, reflecting both eruption style and magma fragmentation conditions (Mastin et al., 2009; Houghton and Carey, 2015). It can be estimated from grain size distributions (GSDs) in the deposit compiled at a range of distances from the source, but determination of a reliable TGSD requires well-preserved deposits and spatially extensive sampling (Pioli et al., 2019). Sampling the whole extent of a deposit can be difficult because of safety concerns in very proximal areas and poor preservation or access issues in distal areas, particularly when deposition is over the sea (Mastin et al., 2009). However, when the total range of grain sizes is small, results are less sensitive to the number of sample sites used (Bonadonna and Houghton, 2005).

The London VAAC uses the Lagrangian advection-diffusion model NAME (Numerical Atmospheric Dispersion Modelling Environment) to simulate dispersal of distal ash clouds and to forecast atmospheric ash concentrations (Jones et al., 2007). Model particles are released into the atmosphere and their motion is driven by wind plus a random component to account for atmospheric turbulence. The 4-dimensional meteorology profile (3 spatial dimensions plus time) is

taken from the Met Office Unified Model (UM), archived at 3-hourly intervals. The UM has a horizontal resolution of ~ 10 km and 59 vertical levels extending from 0–30 km above sea level (Jones et al., 2007; Witham et al., 2017).

Model particles fall out of the ash cloud because of sedimentation (fallout under gravity), dry deposition (turbulence leading to impact with the ground) and wet deposition (washout by falling precipitation or rainout when particles become cloud condensation nuclei) (Webster and Thomson, 2011; Webster and Thomson, 2014; Webster and Thomson, 2017).

As the TGSD of an eruption is rarely available in near real-time, the London VAAC uses a default particle size distribution (PSD) for operational forecasting, based on airborne measurements taken following the January 8, 1990 eruption of Mount Redoubt (Hobbs et al., 1991; Maryon et al., 1999). The source of this ash is thought to have been a (possibly phreatomagmatic) vent explosion, as well as dome collapse creating a co-pyroclastic density current (co-PDC) plume (Scott and McGimsey, 1994). Because only the finest particles are entrained into co-PDC plumes, the resulting TGSD is likely to be finer than for a vent-derived plume (Engwell and Eychenne, 2016). Figure 3-1 shows the size distribution of ash particles in samples taken 2.5 and 7 hours after the eruption (Hobbs et al., 1991).

The simplified curve used for the default NAME modelling, which is also shown, includes linear extrapolation for particle diameters > 30 µm. To obtain the default PSD (Table 3-1), the mass distribution for each particle size bin was calculated assuming particles are spheres of constant density (i.e. volume is proportional to mass). In addition, a 'token' percentage of mass was added in the 30—100 µm bin to account for large particles in the distal ash plume (Maryon et al., 1999).

Grain size bin (µm)	**Mass fraction (%)**
0.1–0.3	0.1
0.3–1	0.5
1–3	5.0
3–10	20.0
10–30	70.0
30–100	4.4

Table 3-1 Default grain size distribution used by London VAAC for forecasting ash dispersion.

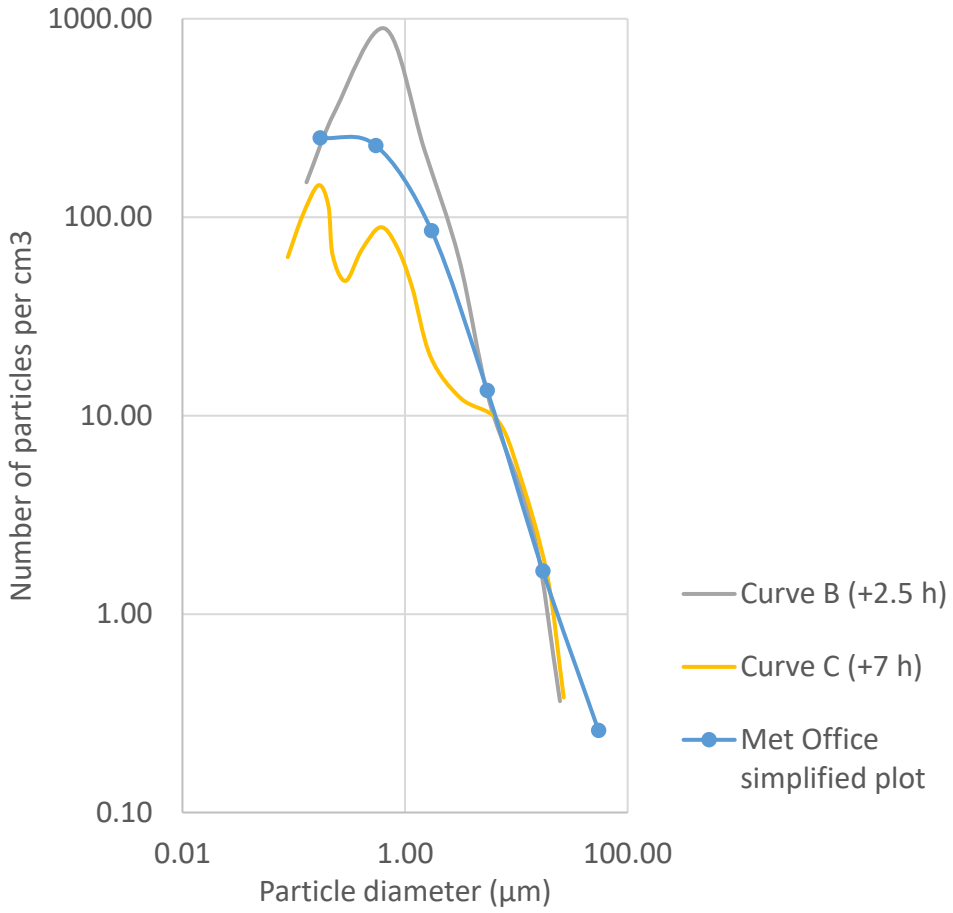

Figure 3-1 Particle number size distributions in emissions from Mount Redoubt, January 8, 1990 eruption. Curve B: 4.0 km above sea level (asl), ~ 130 km downwind and ~ 2.5 hours after eruption. Curve C: 2.6 km asl, ~170 km downwind and ~ 7 hours after eruption (Hobbs et al., 1991). Met Office simplified plot is used for NAME default particle size distribution (from data in Maryon et al., 1999).

Unlike magmatic eruptions, where GSDs become more fine-grained with increasing distance from the vent, when water interacts with magma prior to eruption (phreatomagmatic conditions), grain size appears relatively constant with distance (Cashman and Rust, 2016). This raises the possibility that TGSDs for phreatomagmatic eruptions could be constructed from a more limited set of samples. The lack of a fining trend with distance from source may result from more efficient initial fragmentation conditions (Liu et al., 2017) or distinct sedimentation processes. Water can enhance aggregation, with small particles falling out in clusters close to source (e.g. Stevenson et al., 2013; Mueller et al., 2018) or sedimentation of fine particles can be driven by gravitational instabilities in the plume (e.g. Koyaguchi and Ohno, 2001; Carazzo and Jellinek, 2013; Manzella et al., 2015). This is relevant to the PSD used by the London VAAC because many Icelandic volcanoes erupt from beneath glaciers e.g. Grímsvötn 2011 (Olsson et al., 2013), making phreatomagmatic eruptions likely.

The motivation for this work is to better understand grain size distribution and, in particular, to identify any differences between the GSDs of magmatic eruptions and phreatomagmatic ones. From this we aim to quantify the impact of using different GSDs for modelling the distal ash cloud and to recommend default distributions to use when modelling a range of eruptions.

In this study we first compiled published grain size data for phreatomagmatic eruptions with a range of magma compositions, as well as sample magmatic eruptions for comparison. These data include TGSDs as well as GSDs and median grain size at a range of distances from source (Section 3.2). We then selected a subset to use for NAME simulations, covering a range of eruption sizes and magma compositions (Section 3.3). We present modelled air and deposit mass loadings, as well as a comparison with ground observations and a statistical analysis of the results from different input PSDs (Section 3.4). Finally, we discuss the sensitivity of modelled mass loadings to the PSD used to initialise NAME and make recommendations for real-time forecasting (Sections 3.5 and 3.6).

3.2 Compilation of published grain size data and selection of PSDs for modelling

In order to better understand how grain size changes with distance from the source, and its impact on TGSD for phreatomagmatic eruptions, data were collected from published literature as shown in Table 3-2. Ideally TGSDs would be compiled from both airborne and ground-based sampling, to ensure representation of the full range of erupted particle sizes. However, such comprehensive data are rarely available and so this compilation of published data represents the TGSDs of mapped deposits with no comment made on the goodness (or otherwise) of the GSDs used to compile them. Phreatomagmatic eruptions were selected where at least one of the following datasets was available:

- TGSD which includes grains in the size range used by the VAAC default PSD (≤ 100 μm).
- GSDs or median grain size at a range of distances from the source.

The eruptions cover a range of compositions from basaltic (e.g. Hverfjall 2000 BP) to rhyolitic (e.g. Taupo 130 CE). The change of GSD and median grain size with distance from source were examined. Median grain size was included because it provides information on the stability of grain size with distance from source and is available for a wider range of phreatomagmatic eruptions than TGSD or GSD with distance. It is the preferred measure of central tendency because it is less influenced by outliers than the mean (Bonadonna et al., 2013).

Equivalent data for a range of magmatic eruptions were also compiled for comparison, as shown in Table 3-3 (e.g. basaltic Eldgja 10th Century (Moreland, 2017), andesitic Hekla 1693 (Janebo et al., 2018) and rhyolitic Askja 1875 Layer D (Janebo, 2016).

Eruption	Date	VEI	Magnitude	Intensity	Tephra vol/km^3	Composition	GSDs/Md phi dist from vent	Reference
Iceland								
Askja Unit C	1875	5	4.9	10.9	0.45	Rhyolite	2–58	(Sparks et al., 1981)
Eldgja	10th C	4			0.028	Basalt	11–43	(Moreland, 2017)
Grímsvötn	2004	3			0.0005	Basalt	0.5–26	(Jude-Eton, 2013)
Grímsvötn	2011	4	4.4		0.1	Basalt	50–115	(Olsson et al., 2013)
Hverfjall	2000 BP	2			0.08	Basalt	1–20	(Liu et al., 2017)
Jan Mayen	1732	4			0.4	Basanite	4.5–16.5	(Gjerløw et al., 2015)
Katla	1625	5	5		1.24	Rhyolite	22	(Höskuldsson et al., 2018;
Katla	1755	5	5		1.34	Rhyolite	22	Schmith et al., 2018)
Reykjanes	1226	4	4.6		0.1	Basalt	10–64	(Magnúsdóttir, 2015)
Others								
El Chichón Unit A	1982	5	5.1	11.17	0.29	Trachyandesite	17–70	(Varekamp et al., 1984)
Ilopango	~ 1.5 ka BP	6	6.9	11.3	0.65	Dacite—rhyolite	15—21	(Pedrazzi et al., 2019)
Kelut	1919	4	4.3		0.1	Basaltic andesite–andesite	2–360	(Mohr and van Baren, 1954; Fisher, 1964)
Soufriere St Vincent	1979	3				Basaltic andesite	10–36	(Brazier et al., 1982)
Taupo Hatepe	130 CE	6	6.7	12.1	13.5 for both	Rhyolite	10–95	(Walker, 1981)
Taupo Rotongaio	130 CE	6	6.7	12.1	phases	Rhyolite	7–68	(Walker, 1981)
Taupo Oruanui	25.4 ka BP	8	8.1	11.2	430	Rhyolite	11–111	(Self, 1983; Van Eaton and Wilson, 2013)
Towada	13 ka BP	6	6.7	11.34	0.29	Dacite	15–60	(Hayakawa, 1983; 1985)

Table 3-2 Details of phreatomagmatic eruptions. VEI, magnitude and intensity details come from references shown, the LaMEVE database (Crosweller et al., 2012) and the Global Volcanism Program catalogue of Holocene eruptions (Venzke, 2013).

Eruption	Date	VEI	Magnitude	Intensity	Tephra vol /km3	Composition	GSDs/Md phi dist from vent	Reference
Iceland								
Askja Unit D	1875	5	4.9	10.9	1.37	Rhyolite	2.5–150	(Janebo, 2016)
Eldgja	10th C	4				Basalt	1–21	(Moreland, 2017)
Eyjafjallajökull	2010	4	4	8.65	>0.1	Trachyte	2–56	(Bonadonna et al., 2011)
Grímsvötn	2011	4	4.4		0.7	Basalt	15–70	(Gudmundsson and Larsen, 2016)
Hekla	1104	5	5.1		1.2	Dacite	7–216	(Janebo et al., 2018)
Hekla	1300	4	4		0.1	Andesite	10–212	(Janebo et al., 2018)
Hekla	1693	4	4.3		0.2	Andesite	9–166	(Janebo et al., 2018)
Hekla	1766	4	4.3		0.2	Andesite	6–218	(Janebo et al., 2018)
Hekla	1845	4	4.3	7.86	0.2	Andesite	5–90	(Gudnason et al., 2018)
Hekla	1991	3			0.16–0.19	Basaltic andesite	5–195	(Gudnason et al., 2017)
Hekla	2000	3			0.01/0.001	Basaltic andesite		(Höskuldsson et al., 2007; Biass et al., 2014)
Other								
Ilopango	~ 1.5 ka	6	6.9	11.3	1.84	Dacite—rhyolite	10—33	(Pedrazzi et al., 2019)
Pululagua	2450 BP	6	6	11.3	1.1	Dacite	5–30	(Volentik, 2009)
Ruapehu	1996	3			0.006	Andesite	0.4–177	(Bonadonna et al., 2005)
Rungwe	~ 4 ka BP	5	5	11.24	>=2.2	Trachyte	8–28	(Fontijn et al., 2011)
Fuego	1974	4	4.4	10.75	0.193	Basalt	8–60	(Rose et al., 2008)
Mt St Helens	1980	5	4.8	11.06	1.2	Dacite	10-480	(Carey and Sigurdsson, 1982)
Spurr Aug & Sep	1992	4	4	10.38	> 0.04	Andesite	5-370	(Durant and Rose, 2009)
Chaitén	2008	4	4.9	10.7	0.75	Rhyolite	3-310	(Alfano et al., 2016)

Table 3-3 Details of magmatic eruptions. VEI, magnitude and intensity details come from references shown, the LaMEVE database (Crosweller et al., 2012) and the Global Volcanism Program catalogue of Holocene eruptions (Venzke, 2013).

3.2.1 Eruptions considered

Askja 1875

Askja, within Iceland's Northern Volcanic Zone (NVZ), erupted in 6 phases of varying intensity, lasting 17 hours on 28–29 March 1875. The main eruption included a Subplinian phase (Unit B) followed by phreatomagmatic fall and with some proximal pyroclastic flow (Unit C) and a magmatic Plinian phase (Unit D). Units C and D consisted of 4.5 x 10^8 m^3 and 1.37 x 10^9 m^3 of rhyolitic tephra respectively, (Sparks et al., 1981; Carey et al., 2010; Janebo, 2016).

Eyjafjallajökull 2010

Eyjafjallajökull is situated in the Eastern Volcanic Zone (EVZ) in southern Iceland. The Subplinian 2010 eruption lasted from 14 April–21 May, resulting in significant disruption to European airspace. Plume heights ranged from 3–10 km and dispersing 2.7 x 10^5 m^3 of trachytic tephra (Gudmundsson et al., 2012).

Eldgja 10th century

The flood lava eruption in the first half of the 10th century occurred from the Eldgja fissure within the Katla Volcanic System in Iceland's EVZ. The mainly effusive basaltic eruption is estimated to have lasted between 6 months and 6 years, and included some 16 explosive episodes, both magmatic and phreatomagmatic. A subaerial eruption produced magmatic Unit 7 (2.4 x 10^7 m^3 of tephra) and a subglacial eruption produced phreatomagmatic Unit 8 (2.8 x 10^7 m^3 of tephra). Plume heights for both phases are estimated at 11–18 km (Moreland, 2017).

Grímsvötn 2004 and 2011

Grímsvötn lies beneath the Vatnajökull ice cap in Iceland's EVZ. The 1—6 November 2004 eruption started beneath ~ 200 m thick ice, and magma took some 30 minutes to reach the surface. Phreatomagmatic Unit A, consisting of 5 x 10^5 m^3 of tachylitic tephra with low vesicularity, was dispersed to the north from a 6 km high plume during the initial subaerial phase. Units B to G consisted of pyroclastic density currents (PDCs), some combined with fall deposits (Jude-Eton et al., 2012).

The May 21–28, 2011 eruption was the most explosive at Grímsvötn for over a century (Olsson et al., 2013), with a 15–20 km high plume dispersing 6–8 x 10^8 m^3 of basaltic tephra. High wind shear resulted in low level dispersal to the south (< 4 km altitude) and northerly dispersal at higher altitudes. Alternating water-rich and water-poor phases produced units consisting of fine ash with accretionary lapilli (phreatomagmatic) and pumice-rich lapilli (magmatic) (Stevenson et al., 2013).

Hekla

Hekla is located on the western edge of Iceland's EVZ and has experienced 18 explosive eruptions since 870 CE. High intensity eruptions in 1104 and 1300 produced columns 20 – 25 km high. The 1104 dacitic eruption dispersed 1.2 x 10^9 m^3 tephra to the north and in 1300, 1 x 10^8 m^3 andesitic tephra was dispersed to the northeast. Subplinian eruptions in 1693 in 1766 each deposited ~ 2 x 10^8 m^3 of andesitic tephra towards the north from plumes up to 18 km high (Crosweller et al., 2012; Janebo et al., 2018).

An hour-long Plinian eruption on 2 September 1845 deposited 1.3 x 10^8 m^3 of andesitic tephra east-southeast from a 19 km plume (Gudnason et al., 2018). On 17 January 1991, a 50-minute long explosive eruption dispersed 1.6—1.9 x 10^8 m^3 of basaltic-andesite tephra from a plume blown north-northeast in strong winds and reaching 10.3—12.7 km above sea level (Gudnason et al., 2017). On 26 February 2000, a Subplinian eruption lasting around 30 minutes dispersed ~ 1 x 10^6 m^3 basaltic-andesite tephra to the north from a plume 12 km high (Höskuldsson et al., 2007).

Hverfjall 2000 BP

Hverfjall Fires occurred from a 50 km long fissure in the Krafla Volcanic System in Iceland's NVZ. Magma interaction with an aquifer resulted in an initial basaltic phreatomagmatic fall deposit from the Hverfjall vent with a total volume of 8 x 10^7 m^3 (Liu et al., 2017).

Jan Mayen 1732

Beerenberg Volcano on Jan Mayen Island is situated at the northern end of the mid-Atlantic Ridge and is the northernmost active subaerial volcano. The 1732 Surtseyan eruption on the southwestern flank lasted 4–40 days from historic accounts. A plume of 9–12 km deposited a total volume of ~ 4 x 10^8 m^3 basanitic tephra (Gjerløw et al., 2015).

Katla 1625 and 1755

The subglacial 1625 eruption of Katla, in Iceland's EVZ, began on 2 September with a jökullhaup. Phreatomagmatic conditions were more prevalent at the start and end of the eruption, which consisted of 9 phases, lasting a total of 11 days. It produced ~ 1.24 x 10^9 m^3 of rhyolitic tephra. The 1755 eruption was also subglacial, beginning with a jökullhaup on 17 October and lasting 17 days. 1.34 x 10^9 m^3 of rhyolitic tephra was deposited mainly to the east and ash was reported on ships close to the Faroe Islands (Höskuldsson et al., 2018; Schmith et al., 2018).

Reykjanes 1226

The vent for the 1226 eruption in the Reykjanes Volcanic Belt, southwest Iceland is estimated to have been ~ 2.5 km offshore. A plume 9—10 km high deposited ~ 1 X 10^8 m^3 tholeiitic tephra to the

northeast, a deposit known as the Medieval Tephra Layer (Magnúsdóttir, 2015; Höskuldsson et al., 2018).

Chaitén 2008

The 2008—2013 eruption of Chaitén volcano in Chile included a Subplinian explosive phase on 6 May 2008 which produced a plume 18—20 km high and dispersed 3 x 10^8 m^3 of rhyolitic tephra to the northeast (Alfano et al., 2016).

El Chichón 1982

El Chichón is situated in Chiapas state, south east Mexico. The 28 March–11 April 1982 eruption consisted of 3 Plinian phases interspersed with smaller phreatic eruptions. The initial phreatomagmatic phase lasted 5–6 hours and produced 2.9 x 10^8 m^3 of trachyandesitic tephra (Layer A), dispersed to the northeast from an ash plume 17 km high. Phases B and C then produced ash flow, fall and surge deposits (Varekamp et al., 1984).

Fuego 1974

The October 1974 eruption of Fuego, in Guatemala, lasted 10 days and included a Subplinian phase on 14 October. This phase lasted around 5 hours and produced a plume ~ 15 km high, dispersing 4 x 10^7 m^3 basaltic tephra to the southwest (Rose et al., 2008).

Ilopango ~ 1.5 ka BP

Ilopango caldera is located in the Volcanic Arc of El Salvador. The dacite—rhyolite Tierra Blanca Joven eruption occurred between 270 and 535 CE and consisted of 8 phases (depositional units A_0 to F). Initial magma interaction with a caldera lake or shallow aquifer deposited 3.5 x 10^8 m^3 of tephra westwards from a 29 km high plume (phreatomagmatic Unit A). Drier conditions resulted in magmatic Unit B, with 1.84 x 10^9 m^3 of tephra dispersed to the southwest from a 7 km plume. Units C to F were then deposited by pyroclastic flows and the final Unit G was deposited from a co-PDC plume (Pedrazzi et al., 2019).

Pululagua 2450 BP

Pululagua forms part of the Western Andean Volcanic Front of Ecuador. The Plinian dacitic eruption of 2450 BP occurred in calm conditions and initial phreatomagmatic pulses were immediately followed by a Plinian eruption with a plume height of 28–36 km. The total tephra fall volume was ~1.1 x 10^9 m^3 and ash fall is overlain by pyroclastic flows and surges signalling the end of the eruption (Volentik, 2009).

Ruapehu 1996

Mount Ruapehu is situated at the southern end of the Taupo Volcanic Zone, New Zealand. The Vulcanian eruption on 17 June 1996 lasted around 9 hours and produced an 8.5 km high plume, bent over by a south-southwesterly wind. Initial activity the previous day had drained the small crater lake, resulting in a magmatic eruption producing 4 x 10^6 m^3 of andesitic tephra (Bryan and Sherburn, 1999; Bonadonna et al., 2005; Klawonn et al., 2014).

Rungwe

The plume from the ~ 4 ka BP Plinian eruption of Rungwe volcano in south western Tanzania reached ~ 33 km height in calm conditions and dispersed 3.2—5.8 x 10^9 m^3 trachytic tephra. Ash has been recovered from sediment cores in Lake Malawi, 115 km south-southeast of the volcano (Fontijn et al., 2011).

Mount St Helens 1980

The 1980 eruption of Mount St Helens, in Washington state, USA, produced a 14 km-high ash plume that lasted around 9 hours. The eruption dispersed 1.2 x 10^9 m^3 of dacitic tephra > 500 km to the east-northeast. Aggregation and fallout of fine particles resulted in a secondary thickening of the deposit around 325 km from source (Carey and Sigurdsson, 1982).

Soufrière St Vincent 1979

The 13–26 April 1979 eruption of Soufrière on St Vincent, in the eastern Caribbean, created a new vent in a lava island formed following the 1971–72 eruption. Magma interaction with a shallow hydrothermal system resulted in a phreatomagmatic eruption lasting around 6 minutes on 26 April, which emptied the surrounding crater lake (Fiske and Sigurdsson, 1982). The eruption plume rose to 7–8 km, with dispersal to the south and east. Basaltic andesite tephra covered both St Vincent and the island of Bequia, 36 km to the south (Brazier et al., 1982; Poret et al., 2017).

Mount Spurr

The Crater Peak vent of Mount Spurr in Alaska erupted 3 times in 1992 with Subplinian eruptions on 27 June, 18 August, and 16–17 September. The latter 2 eruptions were extensively sampled and had plumes that reached the stratosphere but ash was mainly dispersed in the upper troposphere (~ 12 km high). Ash was reported up to 1200 km from source, with aggregation of fine particles leading to secondary thickening 200—300 km from source. Both eruptions were of similar size, producing a total of 1.1 x 10^8 m^3 of andesitic tephra (McGimsey et al., 2002; Durant and Rose, 2009).

Taupo volcano

The Phreatoplinian, 25.4 ka BP Oruanui eruption of Taupo volcano in New Zealand produced 10 depositional units from vents within Lake Huka, a paleolake located close to the present-day Lake Taupo. Rhyolitic magma interacted with water to produce ~ 4.3 x 10^{11} m^3 of fall deposit. Unit 3 was extensively sampled and consists of > 5 x 10^9 m^3 tephra, including some co-PDC ash to ~ 40 km from source. (Self, 1983; Wilson, 2001; Van Eaton and Wilson, 2013).

The 130 CE eruption occurred from a northeast-southwest trending fissure centred on Horomatangi Reefs in Lake Taupo. The rhyolitic eruption consisted of 6 phases, of which phases 3 and 4 were phreatomagmatic when water from Lake Taupo entered the vents. Phase 3 produced the 2.5 x 10^9 m^3 Hatepe ash deposit, followed by a coarser pumice bed indicating a short-lived return of magmatic conditions. Phase 4 produced the 3.2 x 10^9 m^3 Rotongaio ash deposit, which is found in eroded gulleys in the Hatepe ash (Walker, 1981; Smith and Houghton, 1995).

Towada ~ 13 ka BP

The 13 ka BP caldera-forming eruption of Towada volcano, in northern Honshu, Japan, produced the phreatomagmatic Hachinohe ashfall overlain with ignimbrite. 3.5 x 10^9 m^3 of rhyodacitic tephra was deposited in a continuous sequence of alternating beds suggesting a fluctuating mass eruption rate. Phreatomagmatic beds of fine ash with accretionary lapilli (beds HP 1, 3 and 5) alternate with magmatic pumice lapilli beds (HP 2, 4 and 6) (Hayakawa, 1990).

3.2.2 Total grain size distributions

Figures 3-2 and 3-3 shows TGSDs for the phreatomagmatic and magmatic eruptions respectively, considered above. The eruptions cover a wide range of magma compositions from mafic (here taken as basaltic—andesitic, ≤ 63 % SiO_2) to silicic (dacitic—rhyolitic, > 63 % SiO_2). Phreatomagmatic eruptions show a smaller range of grain sizes with medians from 0—4 Φ (62.5 —1000 μm) and larger eruptions e.g. Taupo Oruanui, Rotongaio and Hatepe and Towada (all VEI ≥ 6) having the finest TGSDs. In contrast, magmatic eruptions have a wider range of grain sizes with median values in the range -2—4 Φ (62.5 —4000 μm).

3.2.3 Change of grain size with distances from source

Many of the phreatomagmatic eruptions show little variation of GSD with distance, particularly for larger eruptions (Figure 3-4). Similarly median grain size is relatively constant up to tens or even hundreds of km from source for larger phreatomagmatic eruptions (Figure 3-5a). These include the silicic eruptions of Oruanui 25.4 ka BP, and Rotongaio and Hatepe 130 CE, and the mafic eruptions of Jan Mayen 1732 and Grímsvötn 2011. The one eruption that does not fit this pattern is El Chichón 1982 Layer A (VEI 5), where medial samples have a much coarser GSD than distal ones, although this

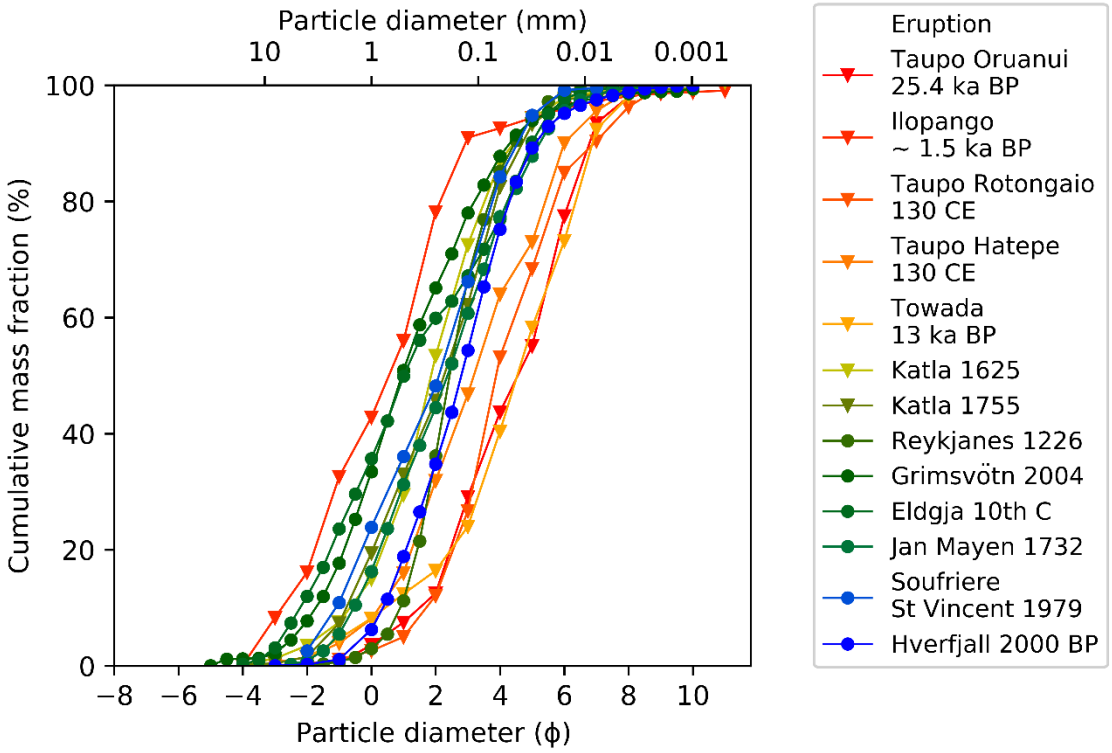

Figure 3-2 Total grain size distributions for phreatomagmatic eruptions based on deposits. The legend lists eruptions in order of VEI (large to small). Magma composition: ▽silicic, **O** mafic.

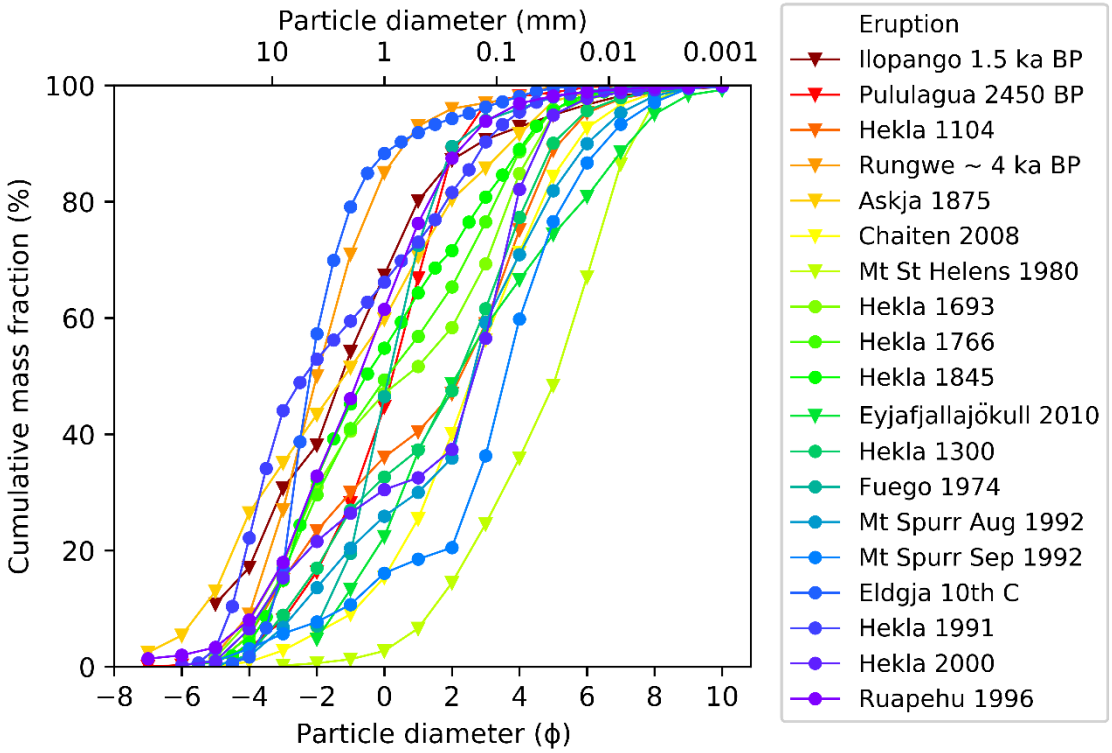

Figure 3-3 Total grain size distributions for selected magmatic eruptions based on deposits. The legend lists eruptions in order of VEI (large to small). Magma composition: ▽ silicic, **O** mafic.

is from very limited data. For the smaller eruptions (VEI ≤ 4), where ash only reaches distances of ≤ 50 km, the median grain size can become finer with distance, as expected for magmatic eruptions (Figure 3-5b.)

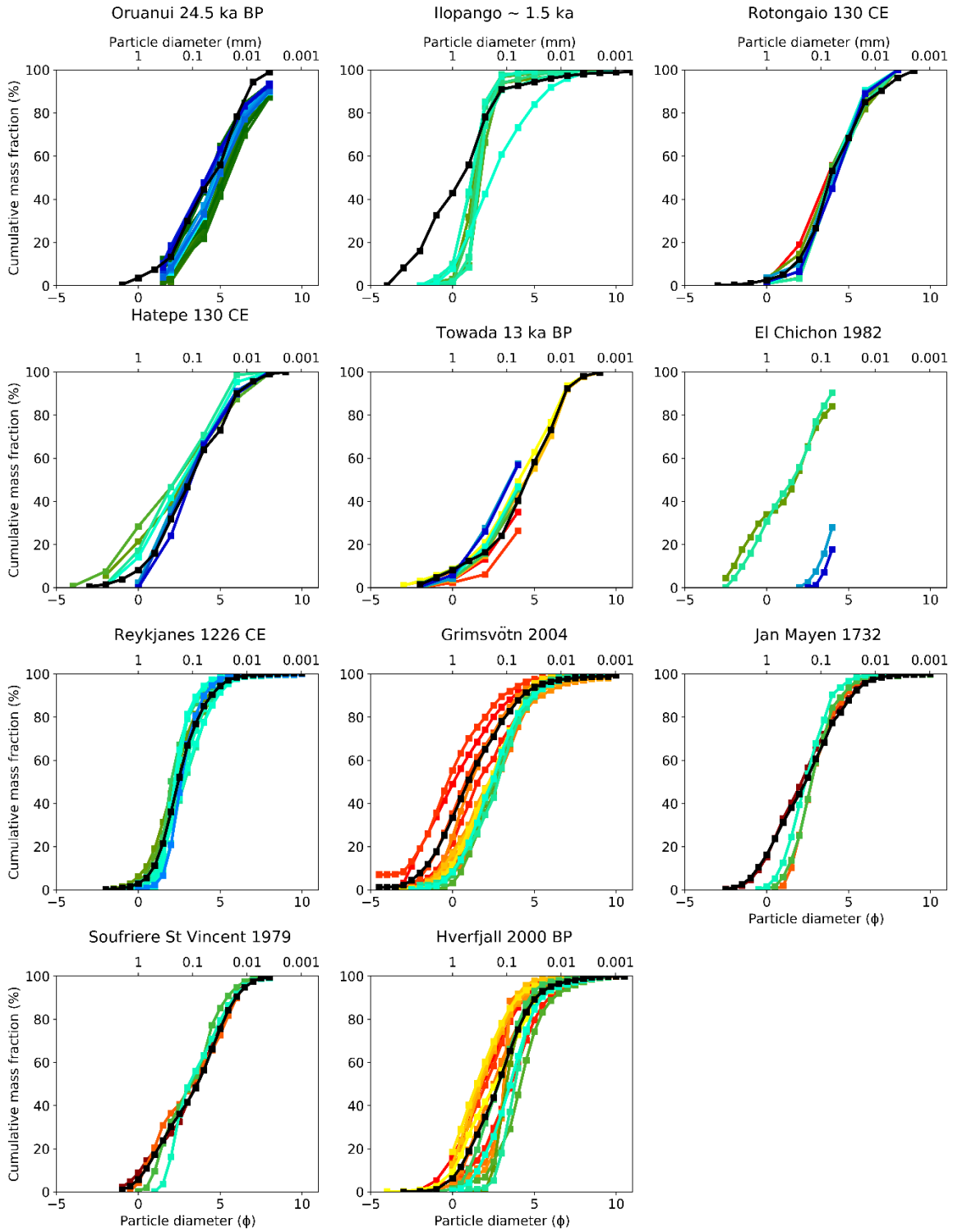

Figure 3-4 Phreatomagmatic TGSDs and GSDs at varying distance from source. Colours indicate distance of GSD from source: < 10 km red/yellow; 10—50 km greens; > 50 km blues. GSDs for Towada and El Chichón only report grains size ≤ 4 Φ.

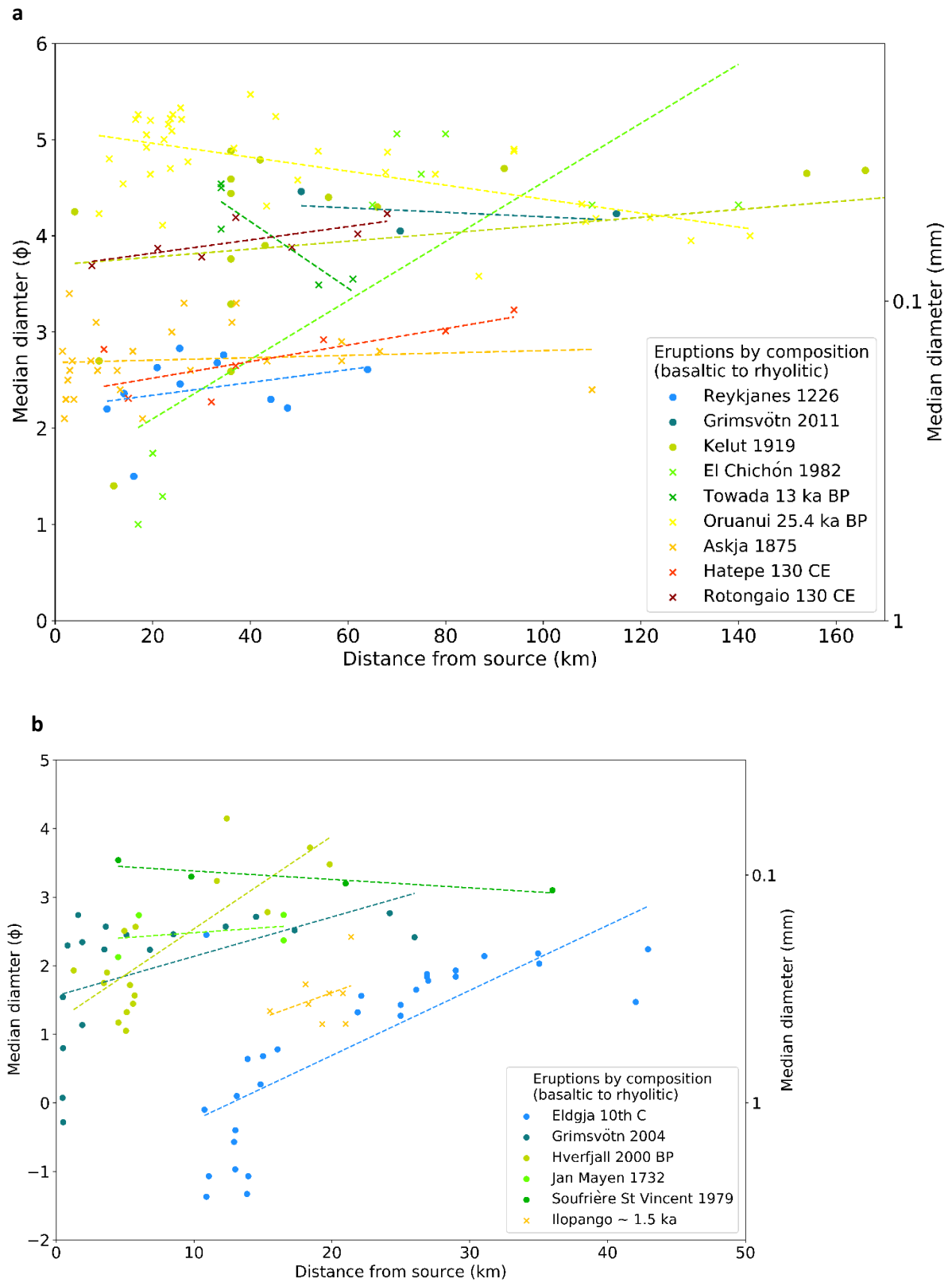

Figure 3-5 Change of median grain size with distance from source for phreatomagmatic eruptions a) sampled > 50 km from source, b) sampled only < 50 km from source. Symbols represent eruption size: x VEI ≥ 5, o VEI ≤ 4. Dashed lines show linear trendlines.

For a few eruptions, phreatomagmatic and magmatic phases from the same eruption have been analysed, but only for Askja 1875 are there sufficient samples, including > 50 km from source to allow the phases to be effectively compared. Figure 3-6 shows a more constant median for the phreatomagmatic phase of this eruption than for the magmatic phase, where there is a significant fining with increasing distance from the vent. Other median grain sizes for phreatomagmatic and magmatic phases from the same eruption are included in Appendix B; for Eldgja 10th century and Ilopango ~ 1.5 ka BP samples are all < 50 km from source and for Grímsvötn 2011 there are only 3 phreatomagmatic data points, making it difficult to reach any conclusions.

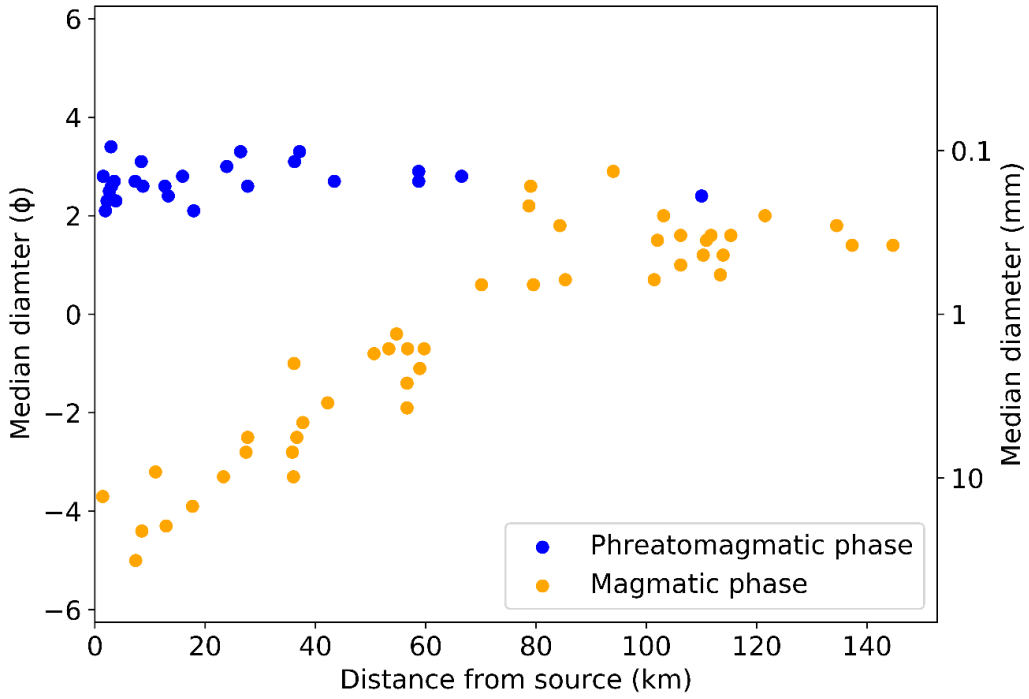

Figure 3-6 Change of median grain size with distance from source for phreatomagmatic and magmatic phases of Askja 1875. Note: phreatomagmatic data point at 110 km is reweighed sample AS82 described in Section 2.4**.**

3.3 Methods

3.3.1 Phi (Φ) scale for PSDs

In the NAME input file, particle size bins are defined in terms of microns (µm) but research papers based on ash samples taken from the ground, often use the phi (Φ) scale for GSD (Krumbein, 1936). Φ is defined in equation 1, where D is the particle size in mm, and D_o is a reference value of 1 mm to make the equation internally consistent (e.g. de' Michieli Vitturi et al., 2015).

$$\Phi = - \log_2 (D/D_0) \qquad (3\text{-}1)$$

To make it easier to run NAME simulations using TGSDs directly from the literature, we compiled micron equivalents of whole- *Φ* and half- *Φ* scales (Tables 3-4 and 3-5). We then calculated mass fractions equivalent to the VAAC default PSD and compared results from NAME simulations of the Eyjafjallajökull 2010 eruption using the new scales and the current VAAC default. Air mass loadings showed very little difference between the three scales, with fractional bias < 0.01 for all cases where the plume is dispersed beyond the immediate source area. Further details of the calculations and the tests are shown in Appendix C; statistical tests are defined in Appendix D.

Reported particle size (*Φ*)	**Particle size range (*Φ*)**	**Particle size range (µm)**	**VAAC default mass fraction (%)**
>12	> 12	< 0.244140625	0.081246
12	11-12	0.244140625 - 0.48828125	0.221047
11	10-11	0.48828125 - 0.9765625	0.287858
10	9-10	0.9765625 - 1.953125	3.056559
9	8-9	1.953125 - 3.90625	6.338199
8	7-8	3.90625 - 7.8125	11.51433
7	6-7	7.8125 - 15.625	32.53672
6	5-6	15.625 - 31.25	41.71322
5	4-5	31.25 - 62.5	2.533153
4	3-4	62.5 - 125	1.717660

Table 3-4 Micron equivalents of whole- *Φ* particle size scale and corresponding mass fractions for the VAAC default particle size distribution.

3.3.2 Normalising TGSDs to ≤ 125 µm

The published TGSDs were normalised to include only grains ≤ 125 µm diameter to assist comparison with the VAAC default PSD which only contains particles ≤ 100 µm. On the Φ scale, we selected reported grain sizes ≥ 4 Φ (3.5 Φ for results reported on the half-Φ scale), because although 4 Φ = 62.5 µm, for sieve results, the 4 Φ bin contains particles from 3—4 Φ i.e. from 62.5—125 µm. Similarly, on the half Φ scale, the 3.5 Φ bin contains particles from 3—3.5 Φ (88.4—125 µm). We selected four phreatomagmatic eruptions for analysis, to cover the range of coarse to fine TGSDs (Eldgja, Grímsvötn 2004, Rotongaio and Oruanui). In addition, one fine (Eyjafjallajökull 2010) and one coarse (Hekla 1991) magmatic TGSD was included. The Eyjafjallajökull 2010 TGSD is compiled from both ground samples and satellite data (Bonadonna et al., 2011) and so, to investigate the impact of including satellite retrievals in TGSDs we also added the Eyjafjallajökull 2010 TGSD derived only from ground samples (Figure 3-7).

Reported particle size (*Φ*)	Particle size range (*Φ*)	Particle size range (µm)	VAAC default mass fraction (%)
> 12.5	> 12.5	< 0.244140625	0.081246
12	12-12.5	0.244140625 - 0.345266983	0.077118
11.5	11.5-12	0.345266983 - 0.488281250	0.143929
11	11-11.5	0.488281250 - 0.690533966	0.143929
10.5	10.5-11	0.690533966 - 0.976562500	0.143929
10	10-10.5	0.976562500 - 1.381067932	1.479235
9.5	9.5-10	1.381067932 - 1.953125	1.577324
9	9-9.5	1.953125 - 2.762135864	1.577324
8.5	8.5-9	2.762135864 - 3.90625	4.760874
8	8-8.5	3.90625 - 5.524271728	5.757166
7.5	7.5-8	5.524271728 - 7.8125	5.757166
7	7-7.5	7.8125 - 11.048543456	10.454179
6.5	6.5-7	11.048543456 - 15.625	22.082541
6	6-6.5	15.625 - 22.097086912	22.082541
5.5	5.5-6	22.097086912 - 31.25	19.630683
5	5-5.5	31.25 - 44.194173824	1.266577
4.5	4.5-5	44.194173824 - 62.5	1.266577
4	4-4.5	62.5 - 88.388347648	1.266577
3.5	3.5-4	88.388347648 – 125.0	0.451083

Table 3-5 Micron equivalents of half-*Φ* particle size scale and corresponding mass fractions for the VAAC default particle size distribution.

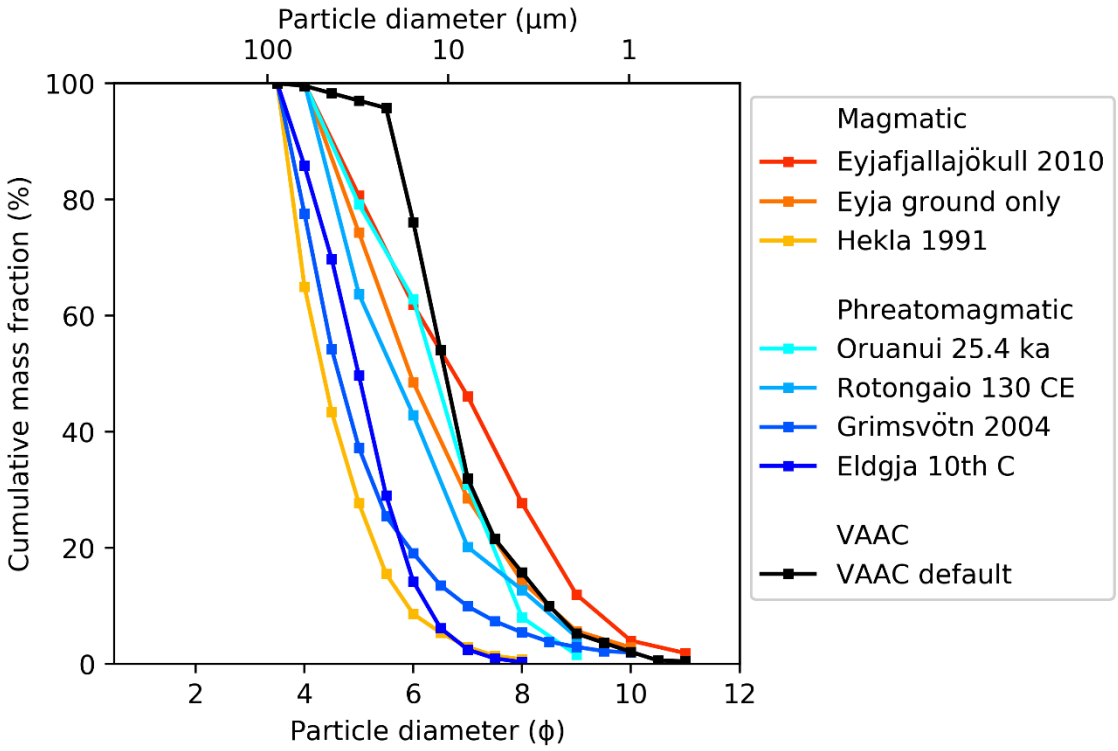

Figure 3-7 TGSDs, normalised to 125 µm, selected for the NAME model runs.

For the eruptions selected, the mass fraction on particles > 3 Φ (≤ 125 μm) ranged from 14 % (Hekla 1991) to 73 % (Rotongaio). In order to forecast actual ash concentrations, it would be important to take account of the mass eruption rate and the fraction of mass represented by the particle sizes used for modelling. However, the focus of this work is to compare the impact of different PSDs and so all NAME runs used the same MER and a fixed distal ash fraction of 5 %, as described further in Section 3.3.3.

3.3.3 NAME simulations

NAME was run on the JASMIN scientific data analysis environment (Lawrence et al., 2013) with the input parameters shown in Table 3-6, using the source location and meteorological conditions from the Eyjafjallajökull 2010 eruption. Particles were assumed to be spherical and of constant density as this study focuses only on the impact of particle size.

PSD was varied with runs using the VAAC default PSD (Table 3-1) and the PSD from each test eruption (detailed in Appendix E) and keeping all the other variables constant. NAME was run with 3-hourly time steps and modelled ash mass loadings in the air and on the ground were output onto a 33 km horizontal grid and plotted using the Python IRIS library. This time steps and grid size were chosen as a balance between time taken for the simulations to run and resolution required to identify the impact of changing PSD on modelled ash mass loadings.

Parameter	**Values**
Source location (latitude, longitude)	-19.62, 63.63
Summit height (m asl)	1666
Source shape	Cuboid, uniform (top hat) distribution of release along entire source region.
No of particles	15000/hr
Particle shape	Spherical
Particle density	2300 kg m^{-3}
Deposition	Dry deposition – Yes; Wet deposition - Yes, bulk scheme. Scavenging parameters as recommended in Thomson et al. (2018), Table 1
Met data	UK_Mk6 L59pp data with ~ 25 km resolution and 3 hourly frequency (Jones, 2018).

Table 3-6 Input parameters for NAME runs.

Source strength was calculated from reported plume height (Webster et al., 2012) using the method of Mastin et al. (2009). For the main series of simulations, we released particles uniformly along the entire height of the source, but to investigate the impact of this decision we also did a limited number of runs with particles released only from the top 1 km, as described in Section 3.4.3 and Appendix F.1. We also investigated the relative importance of wet and dry deposition by running dry-deposition-only and wet-deposition-only simulations using the VAAC default PSD (Appendix F.2). The London VAAC assumes that 5 % of erupted material reaches the distal plume and we also applied this approach.

Results were compared to runs using the VAAC default PSD for 4—8 May 2010, chosen as this was the period relating to the published Eyjafjallajökull 2010 TGSD (Bonadonna et al., 2011). Within this time frame, total column mass loadings were selected for comparison on 2 days: one with a narrow plume (6 May 12:00 UTC) and one with a more extensive plume (8 May 00:00 UTC). Deposition for the period 4—12 May was considered, as ~ 95 % of the mass was found to deposit within this timeframe.

To investigate the change of particle size with distance, modelled deposit PSDs were calculated at ~ 50 km intervals along the axis of deposition, up to 400 km from source as shown in Figure 3-8.

3.3.4 Statistical evaluation of NAME output

The differences between VAAC default and other PSDs were investigated quantitatively using a range of statistical tests. Statistical comparison of different model runs must take into account both differences in ash concentration within a model plume and the different spatial extents of the plumes. As no one test can comprehensively describe differences for dispersion model results, a compilation of tests is recommended (e.g. Chang and Hanna, 2004; Draxler et al., 2013). Four tests, described in detail in Appendix D, were selected to give a broad evaluation of the samples being compared: Fractional Bias (FB); Pearson's Correlation Coefficient (PCC); Figure of Merit in Space (FoM) and the Kolmogorov-Smirnov Parameter (KSP).

Statistical analyses are usually used to compare model results with a limited set of observed values, and hence to make the tests meaningful for comparing two model runs with different input parameters, we used the following approach:

- We applied thresholds (0.2 g m^{-2} for air mass loading and 0.1 g m^{-2} for deposits) before calculating FoM. This enables differences between the PSDs to be identified at useful ash concentrations. Without this, FoM values are 100, because of the wide-ranging extent of very low ash concentrations.

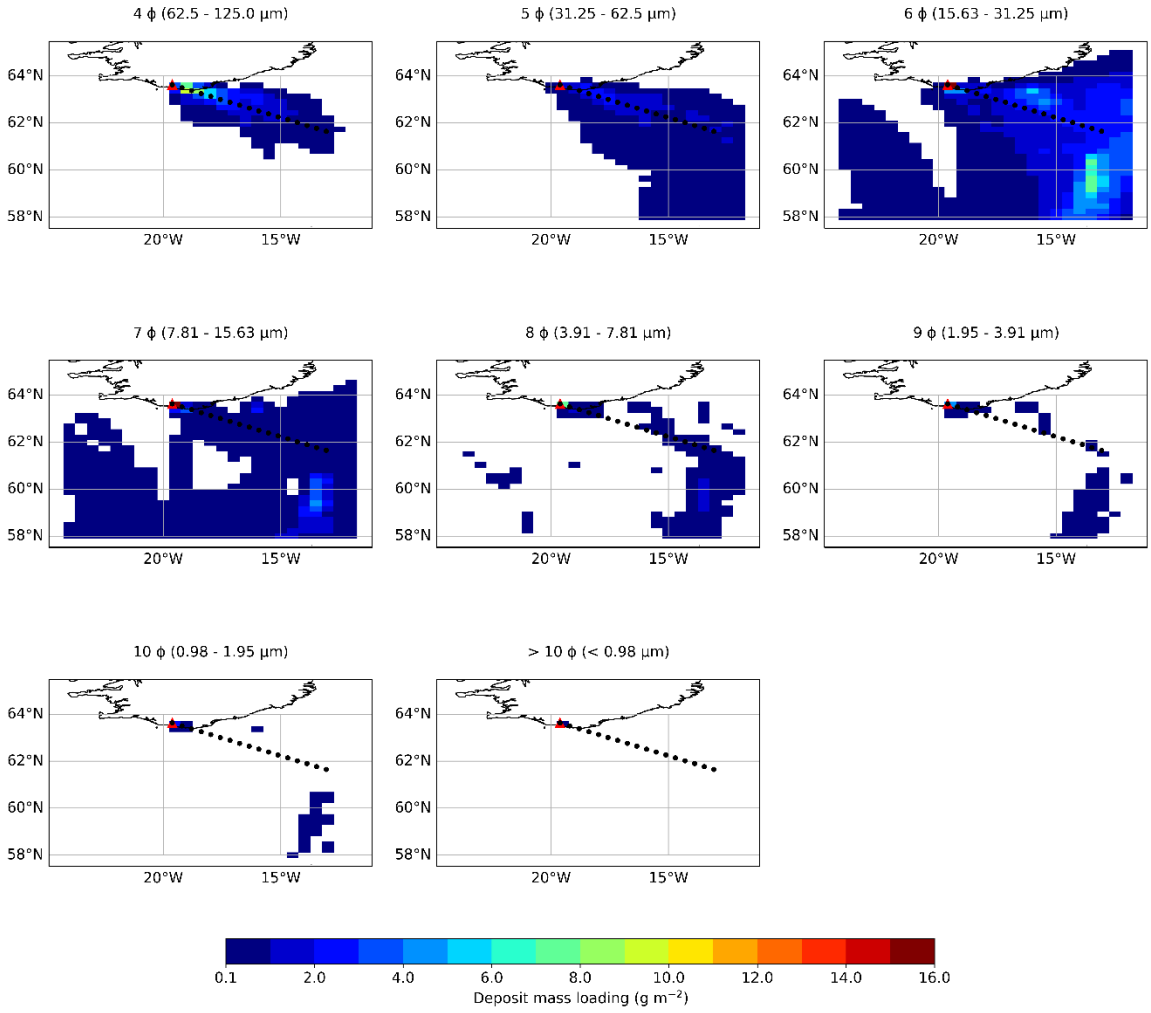

Figure 3-8 Binned deposit concentrations for VAAC default PSD with line of black dots showing positions along the axis of deposition to ~ 400 km from source where model deposit grain size was analysed.

- We defined the area of interest used for FB, PCC and KSP calculations, as a box drawn around the VAAC plume (having the largest spatial extent) using the thresholds as above. This removed the large number of grid cells with very low or no ash loadings far from the main plume.

3.4 Results

This section compares the results using VAAC default PSD and with those using the test PSDs. However, it must be borne in mind that the test PSDs, with the exception Eyjafjallajökull 2010, are based on ground samples while the VAAC default is based on airborne samples. This is addressed further in the Discussion section.

3.4.1 Total column mass loading

Total column mass loading (in g m^{-2}) measures the total mass of ash in the air column above 1 m^2 of ground. Figures 3-9 and 3-10 show total column mass loadings for each PSD on 6 May 2010 12:00 UTC (high plume) and 8 May 2010 00:00 UTC (low plume) respectively. In each case, the VAAC default plume extends further then when using any other PSDs.

3.4.2 Deposit mass loading

Figure 3-11 shows deposit mass loading for the period 4 – 12 May 2010. Deposition using the VAAC default PSD extends further then when using any other input PSD, but proximal deposit mass loadings are lower, reflecting the low mass fraction of larger particles (≤ 5 Φ, ≥ 31.25 µm). Proximal mass loadings of these particles are high for all test PSDs, covering the whole range of magma compositions from basaltic e.g. Hekla 1991, to rhyolitic e.g. Rotongaio (Figure 3-12).

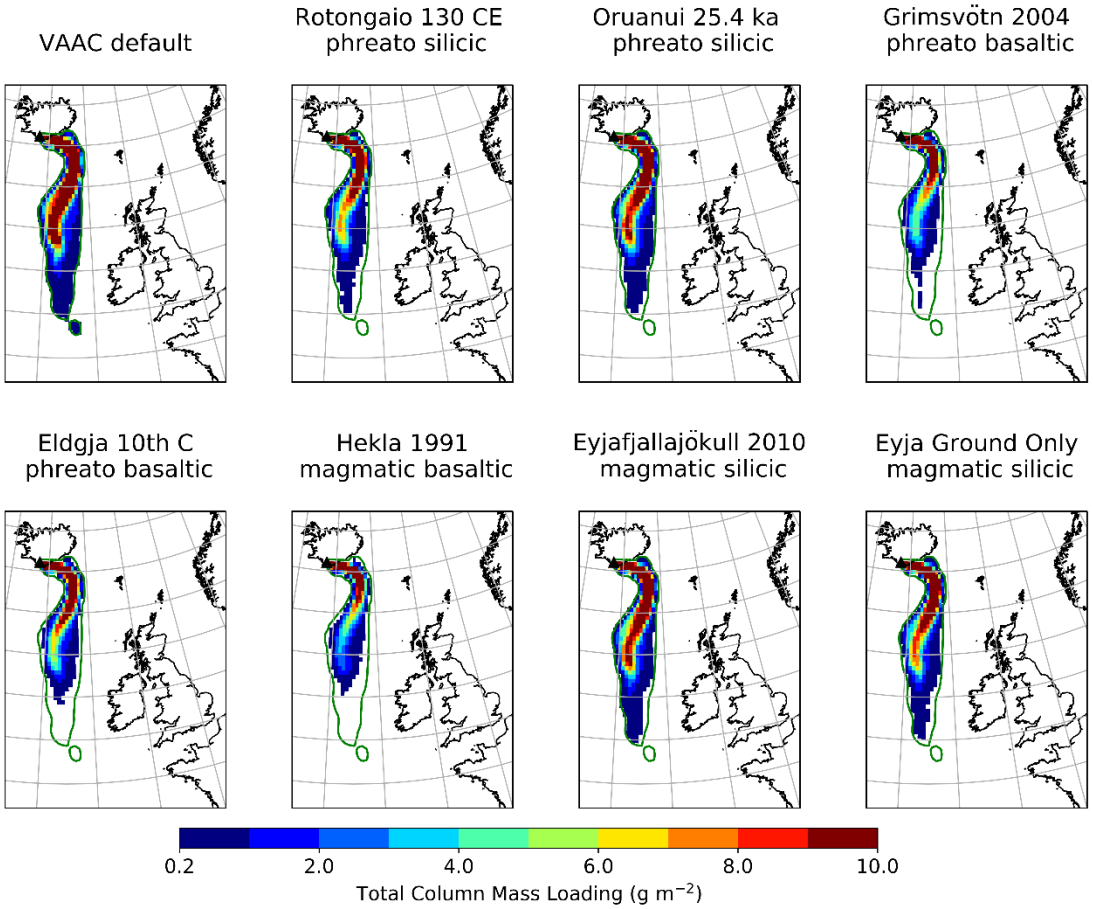

Figure 3-9 Total column mass loadings for 6 May 2010 12:00 UTC using range of input PSDs. Extent of plume using VAAC default PSD is shown as green outline on each plot. Plume height at source ~ 10 km above sea level (Webster et al., 2012).

Particles ≤ 5 Φ (≥ 31.25 µm) reached distances up to ~ 1500 km from source, highlighting the importance of using ground samples when compiling TGSDs, as satellite retrievals are usually not configured to identify such large particles (Stevenson et al., 2015). For the smaller particles (> 5 Φ, < 31.25 µm), using the VAAC default PSD results in a more extensive deposit with higher mass loading of ash, and the difference is largest when compared with using the coarsest (mafic) PSD (Hekla 1991). In this case, the VAAC PSD is likely to substantially overestimate the distance travelled by the small particles before deposition.

Binned median values of the deposit grain size were calculated at each grid point (Figure 3-13). The VAAC default deposit most closely matches deposits using the finest input PSDs (Eyjafjallajökull 2010 and Oruanui ~ 25.4 ka BP).

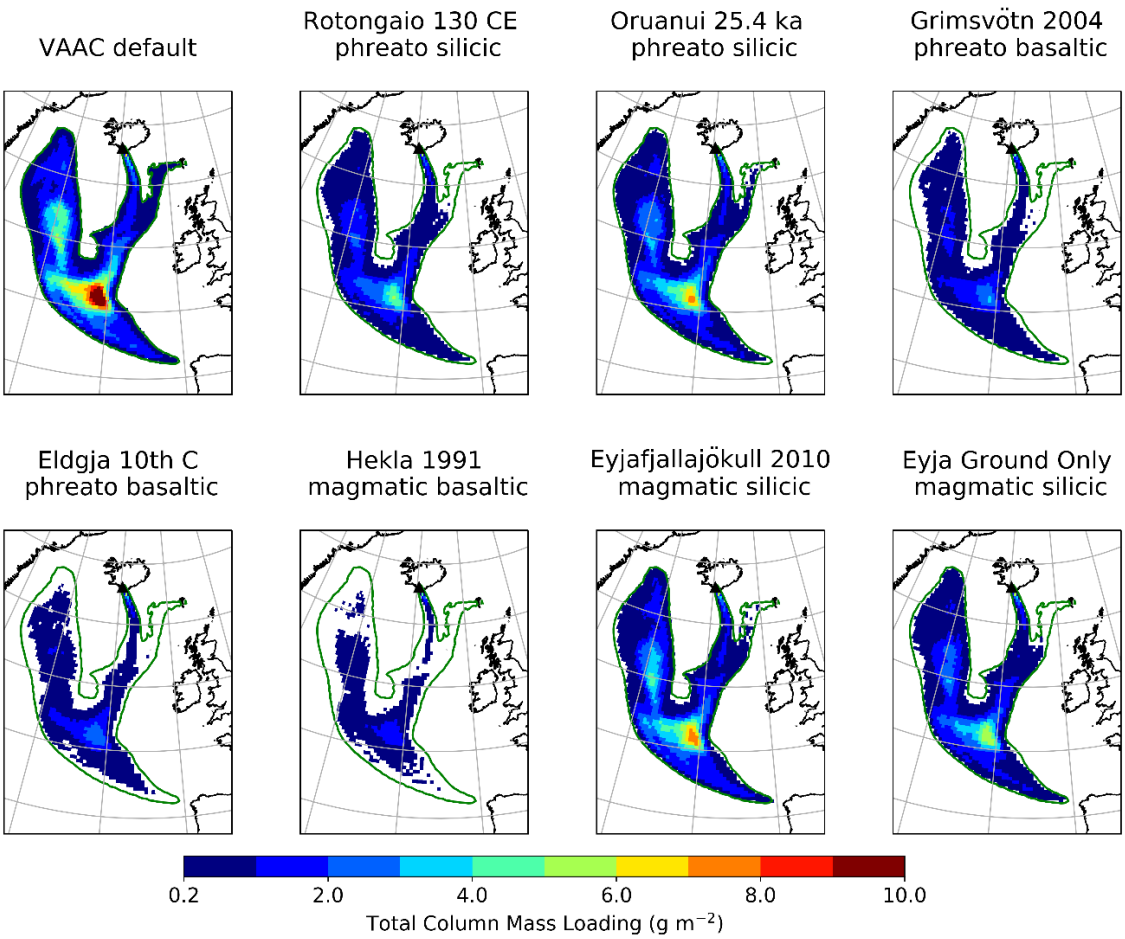

Figure 3-10 Total column mass loadings for 8 May 2010 00:00 UTC using range of input PSDs. Extent of plume using VAAC default PSD is shown as green outline on each plot. Plume height at source ~ 5.5 km above sea level (Webster et al., 2012).

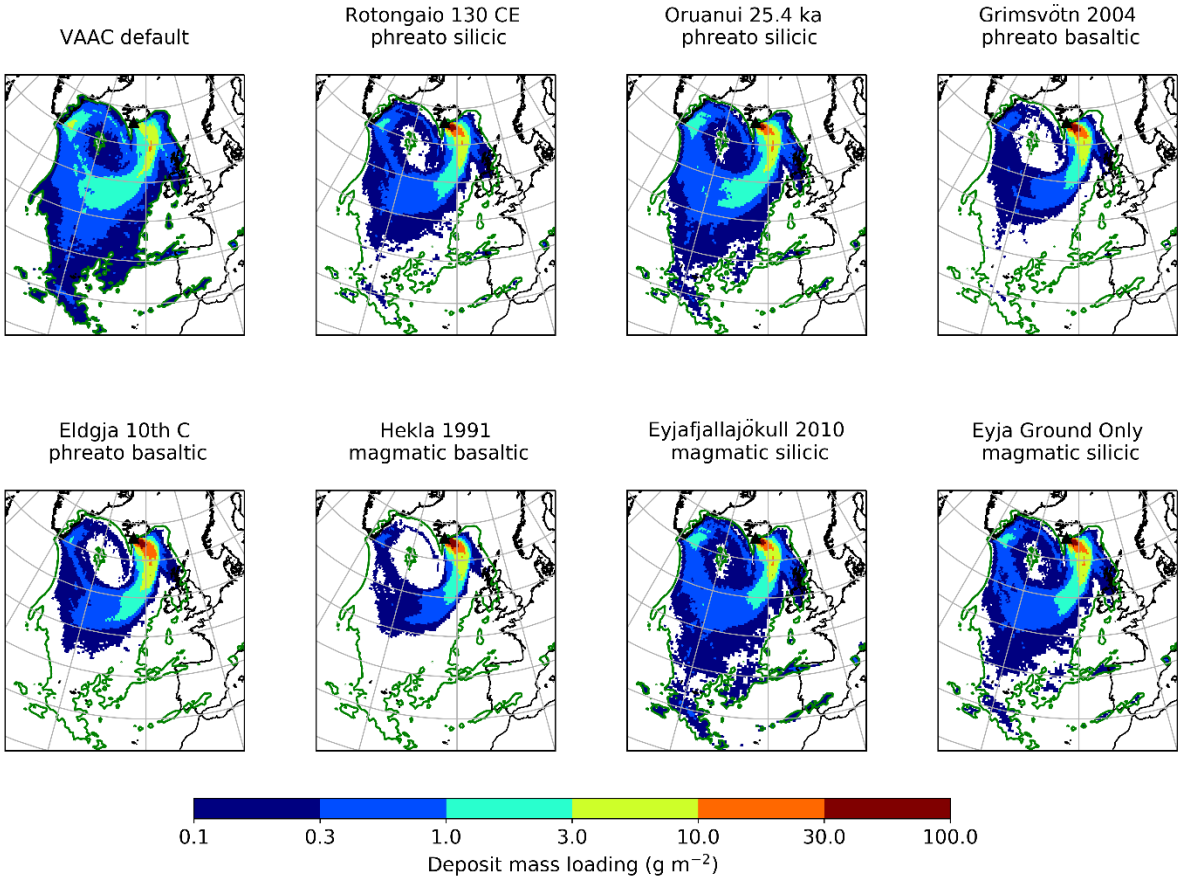

Figure 3-11 Deposition for period 4—12 May 2010 using range of input PSDs. Extent of plume using VAAC default PSD is shown as green outline on each plot.

3.4.3 Comparison with ground observations

Modelled deposit PSDs at ~ 50 km intervals along the axis of deposition, up to 400 km from source were also plotted. Figure 3-14 shows the modelled results for the VAAC default, Oruanui (fine PSD), Hekla 1991 (coarse PSD) and Eyjafjallajökull 2010 excluding satellite data (intermediate PSD), as well as the PSDs obtained from ground sampling for Eyjafjallajökull 2010.

Model particles > 7 Φ (< 7.8 µm) make up a very small mass fraction of the deposit in all the test cases (< 6 %), even at 400 km from source. When considering particles < 7 Φ, the deposits have increasing mass fractions of finer particles with increasing distance, a trend seen most clearly when the input PSD had relatively high proportions of fine particles (Oruanui and Eyjafjallajökull ground samples only).

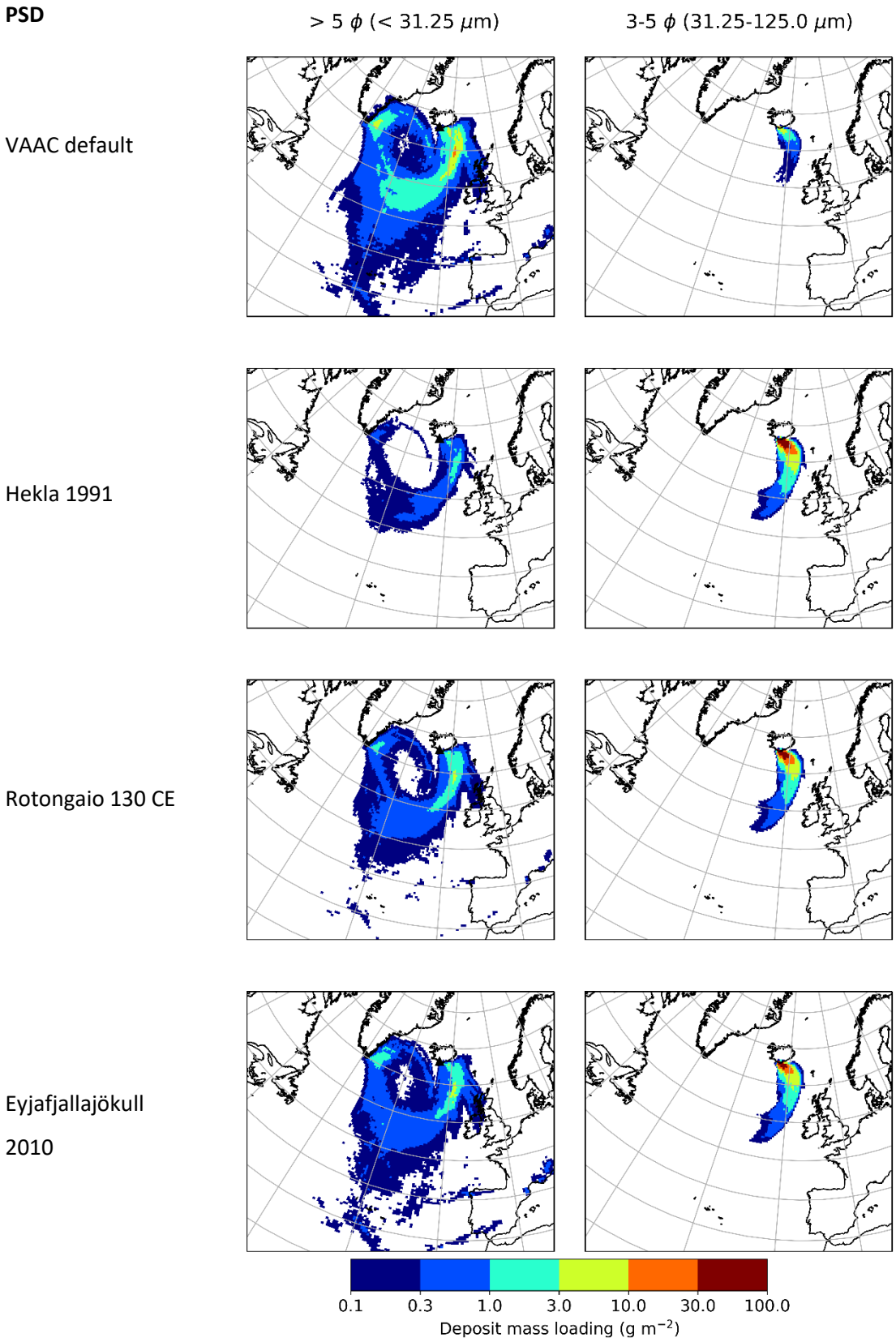

Figure 3-12 Deposit mass loadings binned at > 5 Φ (< 31.25 µm) and 3—5 Φ (31.25—125 µm) for range of PSDs.

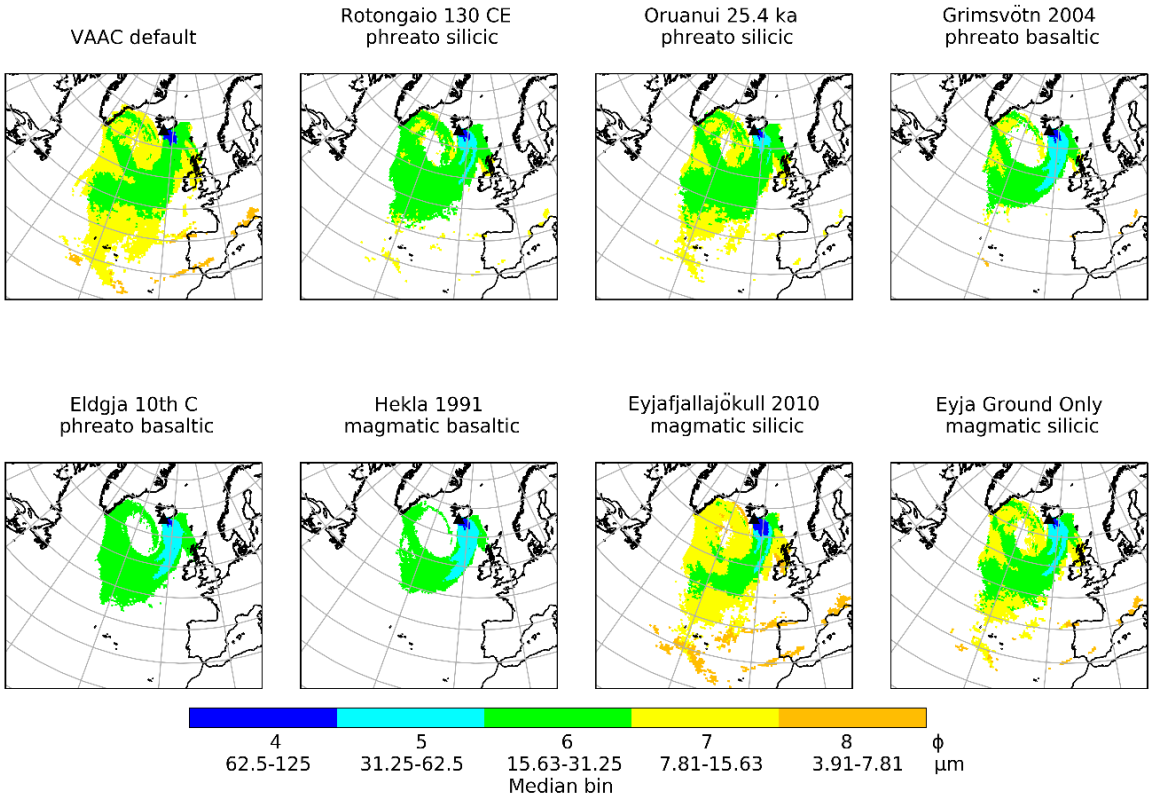

Figure 3-13 Modelled median grain size of deposits using PSDs from phreatomagmatic and magmatic eruptions with silicic and mafic compositions.

This pattern contrasts with the VAAC default case where the input PSD contained only ~ 4 % mass fraction of larger particles (< 5 Φ (> 31.25µm)) and ~ 50 % of particles finer than 7 Φ (7.8 µm). Here the deposit mass fraction > 7 Φ remains at ~ 20 % at distances ≥ ~ 250 km. When considering particles < 7 Φ, the deposits have increasing mass fractions of finer particles with distance, up to ~ 250 km and changes are less pronounced beyond that.

For Eyjafjallajökull 2010, the modelled deposit PSDs are not directly comparable with observed values, because they are taken along different trajectories (the model trajectory follows the deposition axis over the sea (Figure 3-8) whereas sampling obviously took place on land). In addition, particles were released with a uniform distribution along the entire height of the plume, which will increase deposition close to source, particularly for the larger particles. This presents a problem when comparing the modelled deposit with the ground samples, as in this case sampling extended only to ~ 50 km from source. We also ran a simulation using the PSD based on the Eyjafjallajökull 2010 ground samples only, with particles released from the top 1 km of the plume (Figure 3-14f). In this case the PSD of the deposit at ~ 50 km from source is in good agreement with the ground samples, suggesting release from the top of the plume better reflects the source conditions.

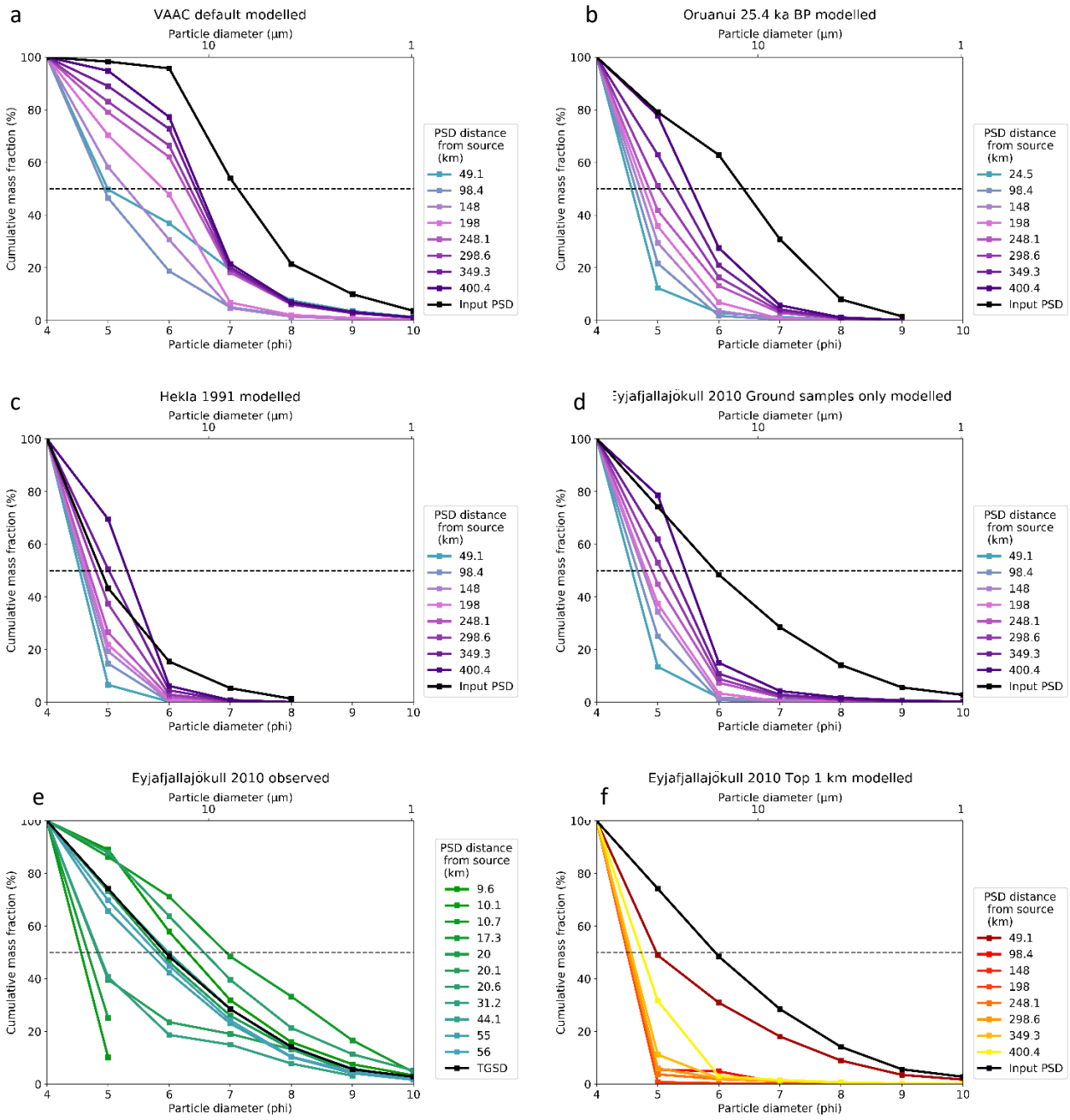

Figure 3-14 Change of modelled deposit PSD with distance from source for input PSDs: (a) default VAAC PSD, (b) Oruanui ~ 25.4 ka BP, (c) Hekla 1991, (d) Eyjafjallajökull 2010 deposit samples only. Samples collected from the Eyjafjallajökull 2010 deposit are shown in (e). (f) shows input PSD as for (d) with particles released only from the top 1 km of the plume. Dotted line indicates the median grain size (i.e. 50 % mass fraction).

At greater distances from source the modelled deposit is made up almost entirely of particles in the 4 Φ bin (62.5—125 μm), until ~ 400 km when there is some deposition of smaller particles. Proximal deposition of the largest particles is likely due to model particles being spherical and so falling out more quickly than real particles with sphericities measured at 0.4—1 (Bonadonna et al., 2011).

Given these caveats, the results can still provide an insight into which particle sizes show the largest differences between samples and simulations. The observed GSDs (up to 56 km from source) contain a higher mass fraction of fine material (up to 50 % > 7 Φ) than shown in the model results at all distances from source (50—400 km). This may be due to aggregated particles falling out prematurely or fine particles depositing *en masse.*

3.4.4 Differences between VAAC default and test PSD mass loadings

Residual ash mass loading was calculated by subtracting the VAAC default value from each test PSD concentration. Figure 3-15 shows the results for total column mass loadings on 6 May 2010 12:00 UTC and 8 May 2010 00:00 UTC and deposition for 4—12 May 2010, for the coarsest (Hekla 1991) and finest (Eyjafjallajökull 2010) test PSD concentrations. Values for the remaining test eruptions are shown in Appendix D, Figures D1—3. Peak values of total column mass loading are up to 8 g m^{-2} higher using the VAAC default PSD than for all other PSDs, with differences most extreme when compared to the coarsest PSDs (Eldgja and Hekla). Deposition close to source is correspondingly lower for the VAAC default than for all test PSDs.

3.4.5 Statistical evaluation of NAME output

Table 3-7 summarises statistical comparisons of the test PSDs with the VAAC default PSD. All test PSDs resulted in lower total column mass loadings, compared to using the VAAC default PSD, as shown by the negative FB (-0.218 — -1.522). Bias was more extreme when the plume was more dispersed on 8 May. Deposit mass loadings were correspondingly greater, although FB values were smaller (0.068— 0.398).

PCC values were high for total column mass loadings, ranging from 0.846 to 0.992, with the highest values seen with the more concentrated plume. PCC values for the deposits were lower, ranging from 0.542 to 0.686. The pattern was similar for FoM, where values for total column mass loadings ranged from 38.68 to 90.25 and again the highest values were seen with the more concentrated plume. Deposit values were between 35.97 and 82.04. KSP ranged from 4.6 to 23.8 for total column mass loadings and from 9.4 to 38.5 for deposits.

For total column mass loadings, the finest PSD (Eyjafjallajökull 2010 including satellite observations) was the most similar to the VAAC default PSD across all measures. The coarsest PSD (Hekla 1991) was most different, except for KSP values for the 6 May, where Eldgja had the highest value. For deposits, Eyjafjallajökull showed the lowest bias and Oruanui was most similar in the other measures. Hekla 1991 was most different across all measures.

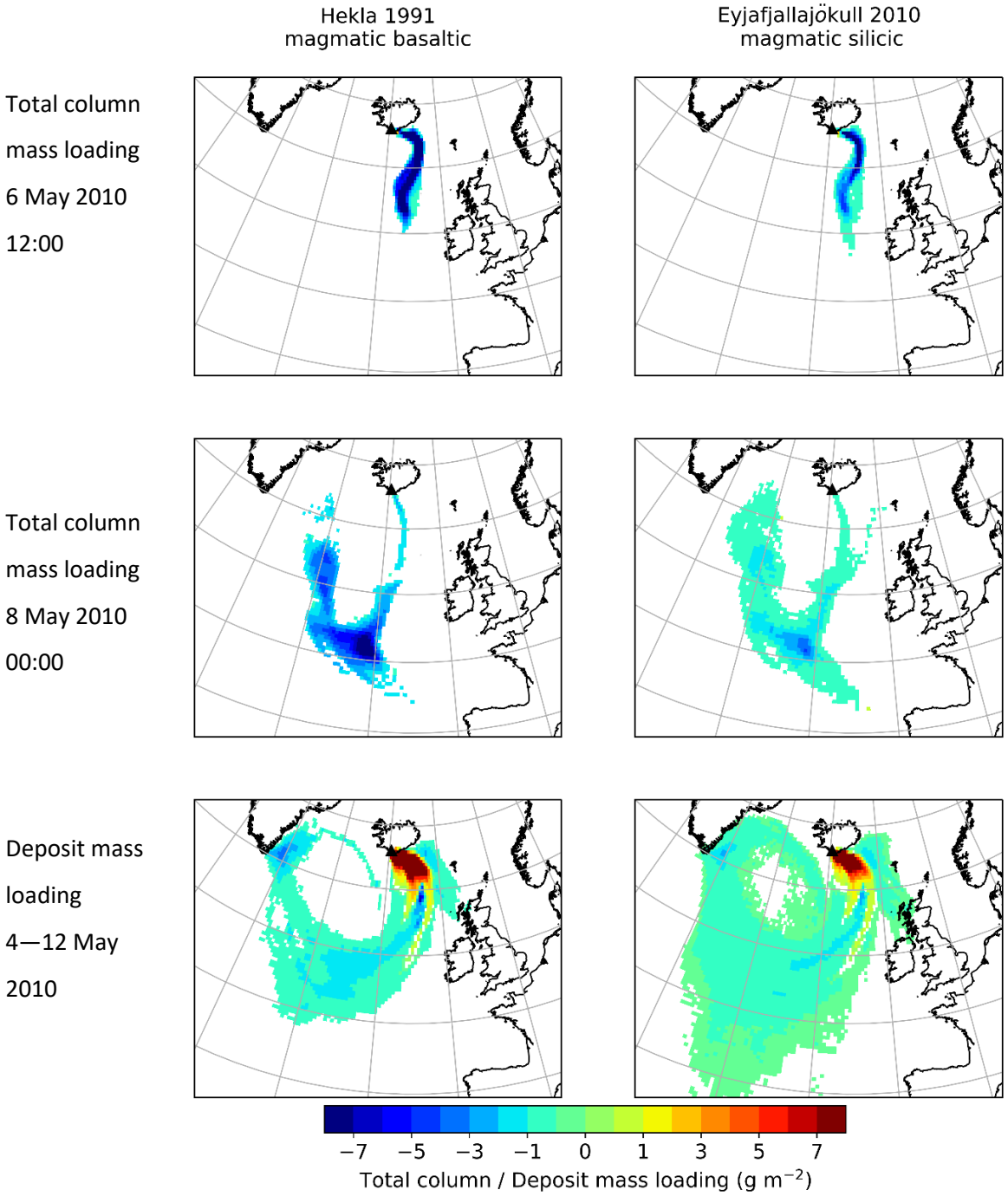

Figure 3-15 Residual mass loadings when VAAC default PSD mass loading is subtracted from coarse (Hekla 1991) and fine (Eyjafjallajökull 2010) PSD for total column mass loadings on 6 May 2010 12:00 UTC and 8 May 2010 00:00 UTC and deposit mass loadings for 4–12 May 2010.

These values confirm that modelled total column and deposit mass loadings using the VAAC default PSD are most similar to a fine PSD, with larger differences for more dispersed ash plumes and for deposition over several days.

Appendix D shows tables comparing values using each PSD with each other. Eruptions with the finest PSDs (Eyjafjallajökull 2010, Oruanui and VAAC default) rank highest across all measures (lower FB,

higher PCC and FoM and lower KSP) when compared with each other and lowest when compared to eruptions with the coarsest PSDs (Hekla 1991 and Eldgja).

		Rotongaio	Oruanui	Grímsvötn 2004	Eldgja	Hekla 1991	Eyja	EyjaG
Air	FB	-0.412	-0.228	-0.584	-0.449	**-0.743**	**-0.218**	-0.318
6 May	PCC	0.973	0.992	0.947	0.965	**0.916**	**0.992**	0.983
2010	FoM	83.17	89.47	71.36	71.36	**63.32**	**90.25**	85.93
12:00	KSP	9.0	9.4	13.9	**22.9**	21.0	**4.6**	7.4
Air	FB	-0.807	-0.464	-1.165	-1.270	**-1.522**	**-0.325**	-0.636
8 May	PCC	0.987	0.995	0.956	0.905	**0.846**	**0.990**	0.991
2010	FoM	80.18	89.82	68.79	58.41	**38.68**	**89.94**	85.32
00:00	KSP	13.2	8.2	18.0	19.7	**23.8**	**5.6**	10.4
Deposit	FB	0.265	0.201	0.336	0.361	**0.398**	**0.068**	0.213
4—12	PCC	0.599	**0.686**	0.569	0.634	**0.542**	0.671	0.642
May	FoM	64.62	**82.04**	47.17	52.40	**35.97**	81.20	72.17
2010	KSP	18.9	**9.4**	28.9	30.4	**38.5**	12.9	16.0

Table 3-7 Statistical differences between VAAC default PSD and test PSD results. FB = fractional bias; PCC = Pearson's Correlation Coefficient; FoM = Figure of Merit in Space; KSP = Kolmogorov Smirnov Parameter.

3.5 Discussion

3.5.1 GSDs for phreatomagmatic eruptions

GSDs for phreatomagmatic eruptions, that is eruptions where external water is thought to have contributed to the fragmentation of the magma, can be relatively constant over large distances from source (Figures 3-4—3-6). This is in contrast to magmatic eruptions where GSDs (and therefore, median grain size) become finer as distance increases (e.g. Figures 3-6 and B-1), a pattern readily explained by particles with higher terminal velocities tending to land on the ground sooner, and so closer to the vent. This raises the question of why proximal phreatomagmatic deposits lack coarser particles and conversely contain more finer particles than seen in most magmatic deposits. The pattern is particularly found for the larger eruptions where ash is deposited > 50 km from source and for these eruptions, source conditions may have been such that an explosive eruption would have taken place even without the presence of water.

Recent modelling suggests that suitable conditions for magma-water interaction leading to phreatomagmatic explosions usually occur only above the magma fragmentation level, as at deeper levels water causes cooling and increased viscosity (Aravena et al., 2018). This is corroborated for Askja 1875 and Taupo 130 CE eruptions, where magma fragmentation mechanisms appear similar for both magmatic and phreatomagmatic phases, with rapid ascent leading to nucleation of small vesicles immediately prior to eruption (Houghton and Carey, 2019).

The presence of water may therefore encourage secondary fragmentation, reducing the size of coarser particles, or may only impact on transport and deposition of already fine particles, by enhancing aggregation. Accretionary lapilli (compound particles much larger than their component ash particles) found in proximal samples (e.g. Brazier et al., 1982; Hayakawa, 1983) can help to explain the relative abundance of fine particles close to source. In addition, the smallest particles have terminal velocities less than velocities within the plume and these do not fall out as individual particles. Gravitational instabilities in the plume influence the settling of these fine particles, resulting in deposition that is independent of distance (Koyaguchi and Ohno, 2001; Manzella et al., 2015).

The lack of change in GSD with distance, suggests that, at least for large phreatomagmatic eruptions, it may be possible to obtain reliable estimates of TGSD from relatively few sampling locations. This could be valuable in enlarging the phreatomagmatic dataset available to dispersion modellers and would aid studies of the fundamental physics of magma fragmentation and controls of eruption intensity. However, if the particles are settling dominantly as aggregates or gravitational instabilities, they will not be effectively modelled as individual particles.

3.5.2 Sensitivity of modelled ash mass loadings to input PSDs.

Modelled total column and deposit mass loadings show significant differences depending on the input PSD used, with results using the VAAC default PSD being most similar to the finest (silicic) test PSDs. However, the VAAC default PSD is based on measurements in the air (Hobbs et al., 1991; Maryon et al., 1999), and the test PSDs, with the exception Eyjafjallajökull 2010, were all compiled using only samples collected on the ground. Satellite data for Eyjafjallajökull 2010 added significant mass on particles ≥ 7 Φ (≤ 7.8 μm) (Bonadonna et al., 2011), and so ground-based TGSDs may underestimate the mass fraction of the finest material. This is an important point, because London VAAC dispersion modelling aims to quantify distal airborne concentrations of the smallest particles.

A comparison of the results for Eyjafjallajökull 2010 using the TGSD based on ground samples only and ground plus satellite data shows that using ground-based TGSDs could lead to model results underestimating both peak ash concentrations and the spatial extent of the plume. This accords with

results of other studies highlighting the importance of compiling TGSDs from both ground and airborne measurements (e.g. Pardini et al., 2016; Poret et al., 2018).

However, satellite retrieval data can also be problematic as all particles are assumed to be dense spheres and the retrieval algorithm is set to interpret brightness temperature difference as always coming from particles with diameter < ~ 16 μm. This does not take into account that reflection off bubble walls of larger particles would also give the same brightness temperature difference (Stevenson et al., 2015). Further work is required to understand how satellite data can best be used to improve TGSDs.

3.5.3 PSDs for real-time forecasting during an eruption

The focus of the London VAAC is dispersal of the distal mass fraction of ash, and the above discussion shows that this is likely to be finer than PSDs used in our NAME simulations which were based on ground samples. TGSDs for phreatomagmatic eruptions can be finer than for magmatic eruptions (Figures 3-2 and 3-3) but when we consider only particles likely to be in the distal ash cloud (> 3Φ, < 125 μm), there is almost total overlap, with composition being the most important factor (Figure 3-7).

Our results show clear differences between total column mass loadings for mafic and silicic eruptions, with modelled concentrations using the current VAAC default PSD matching results for silicic eruptions with the finest PSDs. This could be a problem particularly for forecasting ash plumes from coarse-grained, mafic eruptions which occur frequently in Iceland (as shown in tables 3-2 and 3-3). Hence a second default PSD should be considered for these eruptions.

As described in Section 3.5.2, model PSDs derived only from ground samples are likely to underestimate the mass of the finest particles and this would need to be considered when choosing any new coarse-grained default PSD. One option would be to select a sample eruption where satellite data are also available, as done for Eyjafjallajökull 2010 (Bonadonna et al., 2011). Alternatively, a statistical distribution could be used, based on best fit with sampled data. Pioli et al. (2019) suggest lognormal and Weibull (Rosin-Rammler) distributions are suitable for modelling deposits with fine tails.

This is also relevant to eruptions with the finest GSDs, which may be finer than any of our test values, as it is possible that the VAAC default PSD may also underestimate the mass fraction of the finest particles in these eruptions.

3.6 Conclusions

3.6.1 Summary

We compiled published grain size data for phreatomagmatic and magmatic eruptions and found that for large phreatomagmatic eruptions, GSD remains relatively constant with distance. This suggests that TGSDs for these eruptions could be compiled from fewer samples than are required for typical magmatic eruptions, potentially providing a larger dataset of TGSDs.

We compiled and tested micron equivalents of whole- Φ particle and half- Φ particle size bins, enabling GSDs published in Φ units to be used as NAME model input, without the need to resample the mass fractions to equivalent micron bins.

We investigated the sensitivity of modelled ash mass loadings to input PSDs and found that all the test PSDs resulted in lower total column mass loadings, compared to using the VAAC default PSD. We found clear differences between mass loadings for mafic and silicic eruptions with the VAAC default being most similar to the finest (silicic) test eruptions. Peak values of total column mass loading were up to 8 g m^{-2} higher than for the coarsest test PSD (based on Hekla 1991). As the test PSDs were mainly based on ground-samples, adding mass on the finest particles is likely to produce more representative results. However, as seen by the difference in the Eyjafjallajökull PSD with and without satellite data in Figure 3-7, the coarsest PSDs are still likely to be coarser than the VAAC default value.

3.6.2 Recommendations and future work

More work is now needed to identify suitable phreatomagmatic deposits, probably from the largest eruptions, for which TGSDs could be compiled from limited sampling to expand the current dataset.

A second default PSD should be considered for the London VAAC, suitable for mafic eruptions such as Hekla 1991. This could be compiled from ground and airborne samples or based on a suitable statistical distribution e.g. lognormal or Weibull.

Further work is also needed to understand how best to integrate data from ground samples with satellite retrievals to improve TGSDs which form the basis of model input PSDs.

With the exception of Eyjafjallajökull 2010, the finer test PSDs were based only on ground samples and so it is possible that these PSDs underestimate the true mass of the finest particles. Therefore the possibility of an eruption with a finer grain size distribution than the VAAC default should also be considered.

Chapter 4 Reflections

I believe I have achieved my aim of understanding more about grain size distributions in order to improve ash dispersal modelling.

The fieldwork in Santorini gave me a good understanding of how samples are collected, including some of the difficulties of collecting loose material, such as minimising contamination from overlying beds. I was able to use both traditional (sieving) and new (Camsizer) methods of grain size analysis and I now understand the importance of synthesising data from different methods to obtain the best results across the range of grain sizes encountered in real deposits. Compiling a TGSD for Kelut 1919 showed me the limits of a small dataset, and this work and reanalysis of the Askja 1875 sample underlined the importance of keeping samples which may provide new insights many years after they were collected.

I have been able to collate a significant dataset of GSDs for phreatomagmatic eruptions which shows that, at least for the largest eruptions, grain size varies little with distance from the vent. This is an important finding which should enable more TGSDs to be compiled, of use to dispersion modellers but also to understanding more about source conditions.

Understanding and running the NAME model have proved challenging at times, but I do appreciate the enormous power of being able to simulate ash dispersal using global atmospheric conditions. Results from my modelling show that the London VAAC default PSD is likely to overestimate air concentrations for more mafic eruptions with coarser GSDs, which occur frequently in Iceland. A key recommendation is that a second default PSD should be considered, compiled either from ground and airborne samples or based on a suitable statistical distribution.

References

Alfano, F., Bonadonna, C., Watt, S., Connor, C., Volentik, A. and Pyle, D.M. 2016. Reconstruction of total grain size distribution of the climactic phase of a long-lasting eruption: the example of the 2008–2013 Chaitén eruption. *Bulletin of Volcanology*. **78**(7), p.46.

Aravena, A., Vitturi, M. de' M., Cioni, R. and Neri, A. 2019. Physical constraints for effective magma-water interaction along volcanic conduits during silicic explosive eruptions: reply. *Geology*. **47**(5), pp.e462–e462.

Aravena, A., Vitturi, M. de' M., Cioni, R. and Neri, A. 2018. Physical constraints for effective magma-water interaction along volcanic conduits during silicic explosive eruptions. *Geology*. **46**(10), pp.867–870.

Athanassas, C.D., Bourlès, D.L., Braucher, R., Druitt, T.H., Nomikou, P. and Léanni, L. 2016. Evidence from cosmic ray exposure (CRE) dating for the existence of a pre-Minoan caldera on Santorini, Greece. *Bulletin of Volcanology*. **78**(5), p.35.

Austin-Erickson, A., Büttner, R., Dellino, P., Ort, M.H. and Zimanowski, B. 2008. Phreatomagmatic explosions of rhyolitic magma: experimental and field evidence. *Journal of Geophysical Research*. **113**, p.B11201.

Beckett, F.M., Witham, C.S., Hort, M.C., Stevenson, J.A., Bonadonna, C. and Millington, S.C. 2015. Sensitivity of dispersion model forecasts of volcanic ash clouds to the physical characteristics of the particles. *Journal of Geophysical Research: Atmospheres*. **120**(22), 11,636-11,652.

Biass, S. and Bonadonna, C. 2014. TOTGS: Total grainsize distribution of tephra fallout. [Accessed 31 July 2019]. Available from: https://vhub.org/resources/3297.

Biass, S., Scaini, C., Bonadonna, C., Folch, A., Smith, K. and Höskuldsson, A. 2014. A multi-scale risk assessment for tephra fallout and airborne concentration from multiple Icelandic volcanoes. Part 1: hazard assessment. *Natural Hazards and Earth System Science*. **14**(8), pp.2265–2287.

Bonadonna, C., Cioni, R., Pistolesi, M., Connor, C., Scollo, S., Pioli, L. and Rosi, M. 2013. Determination of the largest clast sizes of tephra deposits for the characterization of explosive eruptions: a study of the IAVCEI commission on tephra hazard modelling. *Bulletin of Volcanology*. **75**(1), p.680.

Bonadonna, C. and Costa, A. 2013. Plume height, volume, and classification of explosive volcanic eruptions based on the Weibull function. *Bulletin of Volcanology*. **75**(8), p.742.

Bonadonna, C., Genco, R., Gouhier, M., Pistolesi, M., Cioni, R., Alfano, F., Hoskuldsson, A. and Ripepe, M. 2011. Tephra sedimentation during the 2010 Eyjafjallajökull eruption (Iceland) from deposit, radar, and satellite observations. *Journal of Geophysical Research*. **116**(B12), p.B12202.

Bonadonna, C. and Houghton, B.F. 2005. Total grain-size distribution and volume of tephra-fall deposits. *Bulletin of Volcanology*. **67**(5), pp.441–456.

Bonadonna, C., Phillips, J.C. and Houghton, B.F. 2005. Modeling tephra sedimentation from a Ruapehu weak plume eruption. *Journal of Geophysical Research*. **110**(B8), p.B08209.

Bond, A. and Sparks, R.S.J. 1976. The Minoan eruption of Santorini, Greece. *Journal of the Geological Society*. **132**(1), pp.1–16.

Brazier, S., Davis, A.N., Sigurdsson, H. and Sparks, R.S.J. 1982. Fall-out and deposition of volcanic ash during the 1979 explosive eruption of the Soufrière of St. Vincent. *Journal of Volcanology and Geothermal Research*. **14**(3–4), pp.335–359.

British Standards Institution 2006. *BS ISO 13322-2: particle size analysis. Image analysis methods. Dynamic image analysis methods.*

Bryan, C.. and Sherburn, S. 1999. Seismicity associated with the 1995–1996 eruptions of Ruapehu volcano, New Zealand: narrative and insights into physical processes. *Journal of Volcanology and Geothermal Research*. **90**(1–2), pp.1–18.

Budd, L., Griggs, S., Howarth, D. and Ison, S. 2011. A fiasco of volcanic proportions? Eyjafjallajökull and the closure of European airspace. *Mobilities*. **6**(1), pp.31–40.

Carazzo, G. and Jellinek, A.M. 2013. Particle sedimentation and diffusive convection in volcanic ash-clouds. *Journal of Geophysical Research: Solid Earth*. **118**(4), pp.1420–1437.

Carey, R.J., Houghton, B.F. and Thordarson, T. 2010. Tephra dispersal and eruption dynamics of wet and dry phases of the 1875 eruption of Askja Volcano, Iceland. *Bulletin of Volcanology*. **72**(3), pp.259–278.

Carey, S.N. and Sigurdsson, H. 1982. Influence of particle aggregation on deposition of distal tephra from the May 18, 1980, eruption of Mount St. Helens volcano. *Journal of Geophysical Research: Solid Earth*. **87**(B8), pp.7061–7072.

Casadevall, T.J. 1994. The 1989-1990 eruption of Redoubt Volcano, Alaska: impacts on aircraft operations. *Journal of Volcanology and Geothermal Research*.

Cashman, K. V. and Rust, A.C. 2016. Volcanic ash: generation and spatial variations *In*: S. Mackie, K. V. Cashman, H. Ricketts, A. C. Rust and M. Watson, eds. *Volcanic ash: hazard observation*. Amsterdam: Elsevier, pp.5–22.

Chang, J.C. and Hanna, S.R. 2004. Air quality model performance evaluation. *Meteorology and Atmospheric Physics*. **87**(1–3), pp.167–196.

Cioni, R., Gurioli, L., Sbrana, A. and Vougioukalakis, G. 2000. Precursory phenomena and destructive events related to the Late Bronze Age Minoan (Thera, Greece) and AD 79 (Vesuvius, Italy) Plinian eruptions; inferences from the stratigraphy in the archaeological areas *In*: W. G. McGuire, D. R. Griffiths, P. L. Hancock and I. S. Stewart, eds. *The archaeology of geological catastrophe. Special Publications 171*. Geological Society, London, pp.123–141.

Civil Aviation Authority 2017. Guidance regarding flight operations in the vicinity of volcanic ash. CAP1236. , p.31. [Accessed 23 July 2019]. Available from: http://publicapps.caa.co.uk/docs/33/CAP 1236 FEB17.pdf.

Costa, A., Suzuki, Y.J., Cerminara, M., Devenish, B.J., Ongaro, T.E., Herzog, M., Van Eaton, A.R., Denby, L.C., Bursik, M., de' Michieli Vitturi, M., Engwell, S., Neri, A., Barsotti, S., Folch, A., Macedonio, G., Girault, F., Carazzo, G., Tait, S., Kaminski, E., Mastin, L.G., Woodhouse, M.J., Phillips, J.C., Hogg, A.J., Degruyter, W. and Bonadonna, C. 2016. Results of the eruptive column model inter-comparison study. *Journal of Volcanology and Geothermal Research*. **326**, pp.2–25.

Crosweller, H.S., Arora, B., Brown, S.K., Cottrell, E., Deligne, N.I., Guerrero, N.O., Hobbs, L., Kiyosugi, K., Loughlin, S.C., Lowndes, J., Nayembil, M., Siebert, L., Sparks, R.S.J., Takarada, S. and Venzke, E. 2012. Global database on large magnitude explosive volcanic eruptions (LaMEVE). *Journal of Applied Volcanology*. **1**(1), p.4.

de' Michieli Vitturi, M., Neri, A. and Barsotti, S. 2015. PLUME-MoM 1.0: a new integral model of volcanic plumes based on the method of moments. *Geoscientific Model Development*. **8**(8), pp.2447–2463.

Degruyter, W., Huber, C., Bachmann, O., Cooper, K.M. and Kent, A.J.R. 2016. Magma reservoir response to transient recharge events: The case of Santorini volcano (Greece). *Geology*. **44**(1), pp.23–26.

Devenish, B.J. 2016. Estimating the total mass emitted by the eruption of Eyjafjallajökull in 2010 using plume-rise models. *Journal of Volcanology and Geothermal Research*. **326**, pp.114–119.

Dingwell, A. and Rutgersson, A. 2014. Estimating volcanic ash hazard in European airspace. *Journal of Volcanology and Geothermal Research*. **286**, pp.55–66.

Draxler, R.R., Arnold, D., Galmarini, S., Hort, M.C., Jones, A., Leadbetter, S.J., Malo, A., Maurer, C. and Rolph, G. 2013. *Evaluation of meteorological analyses for the radionuclide dispersion and deposition from the Fukushima Daiichi nuclear power plant accident. WMO-No 1120.* [Online]. Geneva: WMO. [Accessed 10 July 2019]. Available from: http://library.wmo.int/pmb_ged/wmo_1120_en.pdf.

Druitt, T.H. 2014. New insights into the initiation and venting of the Bronze-Age eruption of Santorini (Greece), from component analysis. *Bulletin of Volcanology*. **76**(2), p.794.

Druitt, T.H., Edwards, L., Mellors, R.M., Pyle, D.M., Sparks, R.S.J., Lanphere, M., Davies, M. and Barreirio, B. 1999. Santorini volcano. *Geological Society, London, Memoirs*. **19**.

Durant, A.J. and Rose, W.I. 2009. Sedimentological constraints on hydrometeor-enhanced particle deposition: 1992 Eruptions of Crater Peak, Alaska. *Journal of Volcanology and Geothermal Research*. **186**(1–2), pp.40–59.

Dürig, T., Gudmundsson, M.T., Karmann, S., Zimanowski, B., Dellino, P., Rietze, M. and Büttner, R. 2015. Mass eruption rates in pulsating eruptions estimated from video analysis of the gas thrust-buoyancy transition—a case study of the 2010 eruption of Eyjafjallajökull, Iceland. *Earth, Planets and Space*. **67**(1), p.180.

Engwell, S. and Eychenne, J. 2016. Contribution of fine ash to the atmosphere from plumes associated with pyroclastic density currents *In*: S. Mackie, K. V. Cashman, H. Ricketts, A. C. Rust and M. Watson, eds. *Volcanic ash: hazard observation*. Amsterdam: Elsevier, pp.67–85.

Fisher, R.V. 1964. Maximum size, median diameter, sorting of tephra. *Journal of Geophysical Research*. **69**(2), pp.341–355.

Fiske, R.S. and Sigurdsson, H. 1982. Soufriere volcano, St. Vincent: observations of its 1979 eruption from the ground, aircraft, and satellites. *Science (New York, N.Y.)*. **216**(4550), pp.1105–6.

Flaherty, T., Druitt, T.H., Tuffen, H., Higgins, M.D., Costa, F. and Cadoux, A. 2018. Multiple timescale constraints for high-flux magma chamber assembly prior to the Late Bronze Age eruption of Santorini (Greece). *Contributions to Mineralogy and Petrology*. **173**(9), p.75.

Fontijn, K., Ernst, G.G.J., Bonadonna, C., Elburg, M.A., Mbede, E. and Jacobs, P. 2011. The ~4-ka Rungwe Pumice (south-western Tanzania): a wind-still Plinian eruption. *Bulletin of Volcanology*. **73**(9), pp.1353–1368.

Friedrich, W.L., Eriksen, U., Tauber, H., Heinemeier, J., Rud, N., Thomsen, M.S. and Buchardt, B. 1988. Existence of a water-filled caldera prior to the Minoan eruption of Santorini, Greece. *Naturwissenschaften*. **75**(11), pp.567–569.

Giehl, C., Brooker, R.A., Marxer, H. and Nowak, M. 2017. An experimental simulation of volcanic ash deposition in gas turbines and implications for jet engine safety. *Chemical Geology*. **461**, pp.160–170.

Gjerløw, E., Höskuldsson, A. and Pedersen, R.-B. 2015. The 1732 Surtseyan eruption of Eggøya, Jan Mayen, North Atlantic: deposits, distribution, chemistry and chronology. *Bulletin of Volcanology*. **77**(2), p.14.

Goode, L.R., Handley, H.K., Cronin, S.J. and Abdurrachman, M. 2018. Insights into eruption dynamics from the 2014 pyroclastic deposits of Kelut volcano, Java, Indonesia, and implications for future hazards. *Journal of Volcanology and Geothermal Research*. **In press**.

Gudmundsson, M.T. and Larsen, G. 2016. Catalogue of Icelandic volcanoes: Grímsvötn. [Accessed 19 July 2019]. Available from: http://icelandicvolcanos.is.

Gudmundsson, M.T., Thordarson, T., Höskuldsson, Á., Larsen, G., Björnsson, H., Prata, F.J., Oddsson, B., Magnússon, E., Högnadóttir, T., Petersen, G.N., Hayward, C.L., Stevenson, J.A. and Jónsdóttir, I. 2012. Ash generation and distribution from the April-May 2010 eruption of Eyjafjallajökull, Iceland. *Scientific Reports*. **2**(1), p.572.

Gudnason, J., Thordarson, T., Houghton, B.F. and Larsen, G. 2018. The 1845 Hekla eruption: grain-size characteristics of a tephra layer. *Journal of Volcanology and Geothermal Research*. **350**, pp.33–46.

Gudnason, J., Thordarson, T., Houghton, B.F. and Larsen, G. 2017. The opening subplinian phase of the Hekla 1991 eruption: properties of the tephra fall deposit. *Bulletin of Volcanology*. **79**(5), p.34.

Hayakawa, Y. 1990. Mode of eruption and deposition of the Hachinohe phreatoplinian ash from the Towada Volcano, Japan. *Geographical Reports of Tokyo Metropolitan University*. **25**, pp.167–182.

Hayakawa, Y. 1985. Pyroclastic geology of Towada volcano. *Bulletin of the Earthquake Research Institute University of Tokyo*. **60**, pp.507–592.

Hayakawa, Y. 1983. The Hachinohe ash: an example of an accretionary lapilli fall deposit from Towada Volcano, Japan. *Bulletin of the Volcanological Society of Japan, series 2*. **28**(1), pp.25–40.

Heiken, G. and McCoy, F. 1990. Precursory activity to the Minoan eruption, Thera, Greece *In*: D. . Hardy, C. G. Doumas, J. A. Sakellarakis and P. M. Warren, eds. *Thera and the Aegean world III : proceedings of the Third International Congress, Santorini, Greece, 3-9 September 1989*., pp.79–87.

Hobbs, P.V., Radke, L.F., Lyons, J.H., Ferek, R.J. and Coffman, D.J. 1991. Airborne measurements of particle and gas emissions from the 1990 volcanic eruptions of Mount Redoubt. *Journal of Geophysical Research*. **96**(10), 18,735-752.

Hooft, E.E.E., Nomikou, P., Toomey, D.R., Lampridou, D., Getz, C., Christopoulou, M.-E., O'Hara, D., Arnoux, G.M., Bodmer, M., Gray, M., Heath, B.A. and Van der Beek, B.P. 2017. Backarc tectonism, volcanism, and mass wasting shape seafloor morphology in the Santorini-Christiana-Amorgos region of the Hellenic Volcanic Arc. *Tectonophysics*. **712**–**713**, pp.396–414.

Höskuldsson, Á., Janebo, M., Thordarson, T., Andrésdóttir, T.B., Jónsdóttir, I., Guðnason, J., Schmith, J., Moreland, W. and Magnúsdóttir, A.Ö. 2018. *Total grain size distribution in selected Icelandic eruptions* [Online]. Reykjavik: University of Iceland. Available from: https://earthice.hi.is/sites/earthice.hi.is/files/Pdf_skjol/total_grain-size_distribution_in_selected_icelandic_eruptions_01.pdf.

Höskuldsson, Á., Óskarsson, N., Pedersen, R., Grönvold, K., Vogfjörð, K. and Ólafsdóttir, R. 2007. The millennium eruption of Hekla in February 2000. *Bulletin of Volcanology*. **70**(2), pp.169–182.

Houghton, B. and Carey, R.J. 2015. Pyroclastic fall deposits. *The Encyclopedia of Volcanoes*., pp.599–616.

Houghton, B.F. and Carey, R.J. 2019. Physical constraints for effective magma-water interaction along volcanic conduits during silicic explosive eruptions: comment. *Geology*. **47**(5), pp.e461–e461.

Janebo, M.H. 2016. *Historic explosive eruptions of Hekla and Askja volcanoes, Iceland: eruption dynamics and source parameters. Ph.D. Thesis*. University of Hawai'i at Manoa.

Janebo, M.H., Houghton, B.F., Thordarson, T., Bonadonna, C. and Carey, R.J. 2018. Total grain-size distribution of four Subplinian–Plinian tephras from Hekla volcano, Iceland: implications for sedimentation dynamics and eruption source parameters. *Journal of Volcanology and Geothermal Research*. **357**, pp.25–38.

Johnston, E.N., Sparks, R.S.J., Nomikou, P., Livanos, I., Carey, S., Phillips, J.C. and Sigurdsson, H. 2015. Stratigraphic relations of Santorini's intracaldera fill and implications for the rate of post-caldera volcanism. *Journal of the Geological Society*. **172**(3), pp.323–335.

Johnston, E.N., Sparks, R.S.J., Phillips, J.C. and Carey, S. 2014. Revised estimates for the volume of the Late Bronze Age Minoan eruption, Santorini, Greece. *Journal of the Geological Society*. **171**(4), pp.583–590.

Jones, A. 2018. *Using NWP data in NAME: a practical guide. NAME Technical Specification Document A03*. Exeter: Met Office.

Jones, A., Thomson, D., Hort, M. and Devenish, B. 2007. The U.K. Met Office's next-generation atmospheric dispersion model, NAME III *In*: *Air Pollution Modeling and Its Application XVII* [Online]. Boston, MA: Springer US, pp.580–589. [Accessed 5 March 2019]. Available from: http://link.springer.com/10.1007/978-0-387-68854-1_62.

Jude-Eton, T.C. 2013. *Eruption dynamics within an emergent subglacial setting: a case study of the 2004 eruption at Grímsvötn volcano, Iceland. Ph.D. Thesis.*[Online] University of Edinburgh. Available from: https://www.era.lib.ed.ac.uk/handle/1842/7682.

Jude-Eton, T.C., Thordarson, T., Gudmundsson, M.T. and Oddsson, B. 2012. Dynamics, stratigraphy and proximal dispersal of supraglacial tephra during the ice-confined 2004 eruption at Grímsvötn Volcano, Iceland. *Bulletin of Volcanology*. **74**(5), pp.1057–1082.

Karátson, D., Gertisser, R., Telbisz, T., Vereb, V., Quidelleur, X., Druitt, T., Nomikou, P. and Kósik, S. 2018. Towards reconstruction of the lost Late Bronze Age intra-caldera island of Santorini, Greece. *Scientific Reports*. **8**(1), p.7026.

Klawonn, M., Frazer, L.N., Wolfe, C.J., Houghton, B.F. and Rosenberg, M.D. 2014. Constraining particle size-dependent plume sedimentation from the 17 June 1996 eruption of Ruapehu Volcano, New Zealand, using geophysical inversions. *Journal of Geophysical Research: Solid Earth*. **119**(3), pp.1749–1763.

Koyaguchi, T. and Ohno, M. 2001. Reconstruction of eruption column dynamics on the basis of grain size of tephra fall deposits: 1. Methods. *Journal of Geophysical Research: Solid Earth*. **106**(B4), pp.6499–6512.

Krumbein, W.C. 1936. The use of quartile measures in describing and comparing sediments. *American Journal of Science*. **32**(188), pp.98–111.

Lawrence, B.N., Bennett, V.L., Churchill, J., Juckes, M., Kershaw, P., Pascoe, S., Pepler, S., Pritchard, M. and Stephens, A. 2013. Storing and manipulating environmental big data with JASMIN *In*: *2013 IEEE International Conference on Big Data* [Online]. IEEE, pp.68–75. [Accessed 17 July 2019]. Available from: http://ieeexplore.ieee.org/document/6691556/.

Le Bas, M.J., Le Maitre, R.W., Streckeisen, A. and Zanettin, B. 1986. A chemical classification of volcanic rocks based on the total alkali-silica diagram. *Journal of Petrology*. **27**(3), pp.745–750.

Leadbetter, S.J., Hort, M.C., Jones, A.R., Webster, H.N. and Draxler, R.R. 2015. Sensitivity of the modelled deposition of Caesium-137 from the Fukushima Dai-ichi nuclear power plant to the wet deposition parameterisation in NAME. *Journal of Environmental Radioactivity*. **139**, pp.200–211.

Liu, E.J., Cashman, K. V., Rust, A.C. and Höskuldsson, A. 2017. Contrasting mechanisms of magma fragmentation during coeval magmatic and hydromagmatic activity: the Hverfjall Fires fissure eruption, Iceland. *Bulletin of Volcanology*. **79**(10), p.68.

Macedonio, G., Costa, A., Scollo, S. and Neri, A. 2016. Effects of eruption source parameter variation and meteorological dataset on tephra fallout hazard assessment: example from Vesuvius (Italy). *Journal of Applied Volcanology*. **5**(1), p.5.

Magnúsdóttir, A.Ö. 2015. *Characteristics of the CE 1226 Medieval tephra layer from the Reykjanes volcanic system. Master's Thesis.*[Online] University of Iceland. Available from: https://skemman.is/bitstream/1946/20359/1/MS-Agnes Ösp.pdf.

Manning, S.W., Höflmayer, F., Moeller, N., Dee, M.W., Ramsey, C.B., Fleitmann, D., Higham, T., Kutschera, W. and Wild, E.M. 2014. Dating the Thera (Santorini) eruption: archaeological and scientific evidence supporting a high chronology. *Antiquity*. **88**(342), pp.1164–1179.

Manzella, I., Bonadonna, C., Phillips, J.C. and Monnard, H. 2015. The role of gravitational instabilities in deposition of volcanic ash. *Geology*. **43**(3), pp.211–214.

Maryon, R.H., Ryall, D.B. and Malcolm, A.L. 1999. *The NAME 4 dispersion model: science documentation. Turbulence and Diffusion Note No 262*. Exeter: Met Office.

Mastin, L.G., Guffanti, M., Servranckx, R., Webley, P., Barsotti, S., Dean, K., Durant, A., Ewert, J.W., Neri, A., Rose, W.I., Schneider, D., Siebert, L., Stunder, B., Swanson, G., Tupper, A., Volentik, A. and Waythomas, C.F. 2009. A multidisciplinary effort to assign realistic source parameters to models of volcanic ash-cloud transport and dispersion during eruptions. *Journal of Volcanology and Geothermal Research*. **186**(1–2), pp.10–21.

McGimsey, R.G., Neal, C.A. and Riley, C.M. 2002. *Areal distribution, thickness, mass, volume, and grain size of tephra-fall deposits from the 1992 eruptions of Crater Peak Vent, Mt. Spurr Volcano, Alaska. U.S. Geological Survey Open-File Report 01-370* [Online]. Anchorage: USGS. [Accessed 15 July 2019]. Available from: https://pubs.usgs.gov/of/2001/0370/.

Mohr, E.C.J. and van Baren, F.A. 1954. *Tropical soils; a critical study of soil genesis as related to climate, rock and vegetation*. The Hague: W. Van Hoeve.

Montanaro, C., Scheu, B., Gudmundsson, M.T., Vogfjörd, K., Reynolds, H.I., Dürig, T., Strehlow, K., Rott, S., Reuschlé, T. and Dingwell, D.B. 2016. Multidisciplinary constraints of hydrothermal explosions based on the 2013 Gengissig lake events, Kverkfjöll volcano, Iceland. *Earth and Planetary Science Letters*. **434**, pp.308–319.

Moreland, W.M. 2017. *Explosive activity in flood lava eruptions: a case study of the 10th century Eldgja eruption, Iceland. Ph.D. Thesis.* University of Iceland.

Mueller, S.B., Kueppers, U., Huber, M.S., Hess, K.-U., Poesges, G., Ruthensteiner, B. and Dingwell, D.B. 2018. Aggregation in particle rich environments: a textural study of examples from volcanic eruptions, meteorite impacts, and fluidized bed processing. *Bulletin of Volcanology*. **80**(4), p.32.

Murrow, P.J., Rose, W.I. and Self, S. 1980. Determination of the total grain size distribution in a Vulcanian eruption column, and its implications to stratospheric aerosol perturbation. *Geophysical Research Letters*. **7**(11), pp.893–896.

Nomikou, P., Parks, M.M., Papanikolaou, D., Pyle, D.M., Mather, T.A., Carey, S., Watts, A.B., Paulatto, M., Kalnins, M.L., Livanos, I., Bejelou, K., Simou, E. and Perros, I. 2014. The emergence and growth of a submarine volcano: The Kameni islands, Santorini (Greece). *GeoResJ*. **1**–**2**, pp.8–18.

Olsson, J., Stipp, S.L.S., Dalby, K.N. and Gislason, S.R. 2013. Rapid release of metal salts and nutrients from the 2011 Grímsvötn, Iceland volcanic ash. *Geochimica et Cosmochimica Acta*. **123**, pp.134–149.

Pardini, F., Spanu, A., de' Michieli Vitturi, M., Salvetti, M.V. and Neri, A. 2016. Grain size distribution uncertainty quantification in volcanic ash dispersal and deposition from weak plumes. *Journal of Geophysical Research: Solid Earth*. **121**(2), pp.538–557.

Pearson, C.L., Brewer, P.W., Brown, D., Heaton, T.J., Hodgins, G.W.L., Jull, A.J.T., Lange, T. and Salzer, M.W. 2018. Annual radiocarbon record indicates 16th century BCE date for the Thera eruption. *Science Advances*. **4**(8), p.eaar8241.

Pedrazzi, D., Suñe-Puchol, I., Aguirre-Díaz, G.J., Costa, A., Smith, V.C., Poret, M., Dávila-Harris, P., Miggins, D.P., Hernández, W. and Gutierrez, E. 2019. The Ilopango Tierra Blanca Joven (TBJ) eruption, El Salvador: volcano-stratigraphy and physical characterization of the major Holocene

event of Central America. *Journal of Volcanology and Geothermal Research*. **377**(1 June 2019), pp.81–102.

Petersen, G.N., Bjornsson, H. and Arason, P. 2012. The impact of the atmosphere on the Eyjafjallajökull 2010 eruption plume. *Journal of Geophysical Research: Atmospheres*. **117**(D20).

Pfeiffer, T. 2001. Vent development during the Minoan eruption (1640 BC) of Santorini, Greece, as suggested by ballistic blocks. *Journal of Volcanology and Geothermal Research*. **106**(3–4), pp.229–242.

Pioli, L., Bonadonna, C. and Pistolesi, M. 2019. Reliability of total grain-size distribution of tephra deposits. *Scientific Reports*. **9**(1), p.10006.

Poret, M., Costa, A., Andronico, D., Scollo, S., Gouhier, M. and Cristaldi, A. 2018. Modeling eruption source parameters by integrating field, ground-based, and satellite-based measurements: the case of the 23 February 2013 Etna paroxysm. *Journal of Geophysical Research: Solid Earth*. **123**(7), pp.5427–5450.

Poret, M., Costa, A., Folch, A. and Martí, A. 2017. Modelling tephra dispersal and ash aggregation: the 26th April 1979 eruption, La Soufrière St. Vincent. *Journal of Volcanology and Geothermal Research*. **347**, pp.207–220.

Pyle, D.M. 1989. The thickness, volume and grainsize of tephra fall deposits. *Bulletin of Volcanology*. **51**(1), pp.1–15.

Rose, W.I., Self, S., Murrow, P.J., Bonadonna, C., Durant, A.J. and Ernst, G.G.J. 2008. Nature and significance of small volume fall deposits at composite volcanoes: insights from the October 14, 1974 Fuego eruption, Guatemala. *Bulletin of Volcanology*. **70**(9), pp.1043–1067.

Rust, A.C. and Cashman, K. V. 2011. Permeability controls on expansion and size distributions of pyroclasts. *Journal of Geophysical Research: Solid Earth*. **116**, p.B11202.

Saxby, J., Beckett, F., Cashman, K., Rust, A. and Tennant, E. 2018. The impact of particle shape on fall velocity: implications for volcanic ash dispersion modelling. *Journal of Volcanology and Geothermal Research*. **362**, pp.32–48.

Schmith, J., Höskuldsson, Á., Holm, P.M. and Larsen, G. 2018. Large explosive basaltic eruptions at Katla volcano, Iceland: fragmentation, grain size and eruption dynamics. *Journal of Volcanology and Geothermal Research*. **354**, pp.140–152.

Scott, W.E. and McGimsey, R.G. 1994. Character, mass, distribution, and origin of tephra-fall deposits of the 1989–1990 eruption of Redoubt volcano, south-central Alaska. *Journal of Volcanology and Geothermal Research*. **62**(1–4), pp.251–272.

Self, S. 1983. Large-scale phreatomagmatic silicic volcanism: a case study from New Zealand. *Journal of Volcanology and Geothermal Research*. **17**(1–4), pp.433–469.

Smith, R.T. and Houghton, B.F. 1995. Vent migration and changing eruptive style during the 1800a Taupo eruption: new evidence from the Hatepe and Rotongaio phreatoplinian ashes. *Bulletin of Volcanology*. **57**(6), pp.432–439.

Song, W., Yang, S., Fukumoto, M., Lavallée, Y., Lokachari, S., Guo, H., You, Y. and Dingwell, D.B. 2019. Impact interaction of in-flight high-energy molten volcanic ash droplets with jet engines. *Acta Materialia*. **171**, pp.119–131.

Spanu, A., de' Michieli Vitturi, M. and Barsotti, S. 2016. Reconstructing eruptive source parameters from tephra deposit: a numerical study of medium-sized explosive eruptions at Etna volcano. *Bulletin of Volcanology*. **78**(9), p.59.

Sparks, R.S.J., Wilson, L. and Sigurdsson, H. 1981. The pyroclastic deposits of the 1875 eruption of Askja, Iceland. *Philosophical Transactions of the Royal Society A: Mathematical, Physical and Engineering Sciences*. **299**(1447), pp.241–273.

Stevenson, J.A., Loughlin, S.C., Font, A., Fuller, G.W., MacLeod, A., Oliver, I.W., Jackson, B., Horwell, C.J., Thordarson, T. and Dawson, I. 2013. UK monitoring and deposition of tephra from the May 2011 eruption of Grímsvötn, Iceland. *Journal of Applied Volcanology*. **2**(1), p.3.

Stevenson, J.A., Millington, S.C., Beckett, F.M., Swindles, G.T. and Thordarson, T. 2015. Big grains go far: understanding the discrepancy between tephrochronology and satellite infrared measurements of volcanic ash. *Atmospheric Measurement Techniques*. **8**, pp.2069–2091.

Thomson, D.J., Jones, A.R., Devenish, B.J., Hort, M.C., Webster, H.N., Muller, E.., Meneguz, E., Beckett, F.M., Hugget, L. and Selvaratnam, V. 2018. *Input. NAME Technical Specification Document B01*. Exeter: Met Office.

Van Eaton, A.R. and Wilson, C.J.N. 2013. The nature, origins and distribution of ash aggregates in a large-scale wet eruption deposit: Oruanui, New Zealand. *Journal of Volcanology and Geothermal Research*. **250**, pp.129–154.

Varekamp, J.C., Luhr, J.F. and Prestegaard, K.L. 1984. The 1982 eruptions of El Chichón Volcano (Chiapas, Mexico): character of the eruptions, ash-fall deposits, and gasphase. *Journal of Volcanology and Geothermal Research*. **23**(1–2), pp.39–68.

Venzke, E. 2013. Global Volcanism Program: volcanoes of the world.

Verolino, A., White, J.D.L. and Brenna, M. 2018. Eruption dynamics at Pahvant Butte volcano, Utah, western USA: insights from ash-sheet dispersal, grain size, and geochemical data. *Bulletin of Volcanology*. **80**(11), p.81.

Vespa, M., Keller, J. and Gertisser, R. 2006. Interplinian explosive activity of Santorini volcano (Greece) during the past 150,000 years. *Journal of Volcanology and Geothermal Research*. **153**(3–4), pp.262–286.

Volentik, A.C.M. 2009. *Tephra transport, sedimentation and hazards. Ph.D. Thesis.*[Online] University of South Florida. Available from: https://scholarcommons.usf.edu/etd/71/.

Walker, G.P.L. 1981. Characteristics of two phreatoplinian ashes, and their water-flushed origin. *Journal of Volcanology and Geothermal Research*. **9**(4), pp.395–407.

Webster, H.N. and Thomson, D.J. 2017. *A particle size dependent wet deposition scheme for NAME. Forecasting Research Technical Report 624.* Exeter: Met Office.

Webster, H.N. and Thomson, D.J. 2011. Dry deposition modelling in a Lagrangian dispersion model. *International Journal of Environment and Pollution*. **47**(1/2/3/4), p.1.

Webster, H.N. and Thomson, D.J. 2014. *The NAME wet deposition scheme. Forecasting Research Technical Report 584.* Exeter.

Webster, H.N., Thomson, D.J., Johnson, B.T., Heard, I.P.C., Turnbull, K., Marenco, F., Kristiansen, N.I., Dorsey, J., Minikin, A., Weinzierl, B., Schumann, U., Sparks, R.S.J., Loughlin, S.C., Hort, M.C., Leadbetter, S.J., Devenish, B.J., Manning, A.J., Witham, C.S., Haywood, J.M. and Golding, B.W. 2012. Operational prediction of ash concentrations in the distal volcanic cloud from the 2010 Eyjafjallajökull eruption. *Journal of Geophysical Research: Atmospheres*. **117**(D20).

Wilkins, K.L., Benedetti, A., Kristiansen, N.I. and Lange, A.C. 2016. Applications of satellite observations of volcanic ash in atmospheric dispersion modelling *In*: S. Mackie, K. V. Cashman, H. Ricketts, A. C. Rust and M. Watson, eds. *Volcanic ash : hazard observation*. Amsterdam: Elsevier, pp.233–246.

Wilson, C.J.. 2001. The 26.5 ka Oruanui eruption, New Zealand: an introduction and overview. *Journal of Volcanology and Geothermal Research*. **112**(1–4), pp.133–174.

Witham, C., Hort, M., Thomson, D., Leadbetter, S.J., Devenish, B.J., Webster, H., Beckett, F.M. and Kristiansen, N. 2017. *The current volcanic ash modelling set-up at the London VAAC. Met Office technical summary.* Exeter: Met Office.

Zimanowski, B., Büttner, R., Dellino, P., White, J.D.L. and Wohletz, K.H. 2015. Magma–water interaction and phreatomagmatic fragmentation. *The Encyclopedia of Volcanoes*., pp.473–484.

Appendix A Methods used in calculation of TGSD for Kelut 1919

GSDs reported in Mohr and Baren (1954) were interpolated into whole Φ bins and deposit accumulation was calculated at each sampling location, to provide data in the correct format for input to TOTGS (Biass and Bonadonna, 2014)

							Added point		
Phi	2	4	9	36	42	92	220	360	Density kg/m3
0	10.3	0.5	0.2		0.1				0.260
1	11.3	3	1.3	0.1	0.2				0.260
2	47.4	16	35.7	19.8	6.5	0.1			0.260
3	8.4	11.8	25.4	19.2	9.1	1.5	1.1	0.6	0.200
4	6.8	14.5	5.7	14.3	18.1	24.5	17.4	9	0.150
5	5.4	19.4	10.5	14.9	21	28.4	35.9	44.9	0.125
6	3	16.5	9.9	12.1	18.6	21.8	30.5	41.1	0.100
7	2.1	8.6	4.4	8.9	13.4	11.2	6.7	1.4	0.100
8	1.7	5.4	3.2	5.4	7.9	6.9	4.3	1.1	0.100
9	1.2	2.1	2	1.9	2.5	2.7	1.8	0.7	0.100
10	0.4	0.7	0.7	0.5	0.7	1.1	0.7	0.2	0.100
11	0.4	0.7	0.7	0.5	0.7	1.1	0.7	0.2	0.100
12	1.6	0.7	0.3	2.5	1.2	0.9	0.9	0.8	0.100
Density *D* (g/m3)	223.55	155.00	190.40	162.02	134.28	121.21	118.78	116.33	
Thickness *T* (m)	0.398	0.307	0.161	0.109	0.103	0.062	0.017	0.004	
Accum = *D/T* (g/m2)	88.97	47.59	30.65	17.66	13.83	7.52	2.02	0.51	

Table A-1 Details of interpolation used to convert observations from Tables 2-3 and 2-4 (Mohr and van Baren, 1954) to mass fractions (whole Φ intervals) and deposit accumulations (g m^{-2}) for input into TOTGS (Table A-2).

lat	long	g/m^2	0	1	2	3	4	5	6	7	8	9	10	11	12
-7.938	112.296	88.97	10.3	11.3	47.4	8.4	6.8	5.4	3.0	2.1	1.7	1.2	0.4	0.4	1.6
-7.938	112.274	47.61	0.5	3.0	16.0	11.8	14.5	19.4	16.5	8.6	5.4	2.1	0.7	0.7	0.7
-7.928	112.228	30.65	0.2	1.3	35.7	25.4	5.7	10.5	9.9	4.4	3.2	2.0	0.7	0.7	0.3
-7.899	111.992	17.65	0.0	0.1	19.8	19.2	14.3	14.9	12.1	8.9	5.4	1.9	0.5	0.5	2.5
-7.881	111.931	13.83	0.1	0.2	6.5	9.1	18.1	21.0	18.6	13.4	7.9	2.5	0.7	0.7	1.2
-7.796	111.496	7.5	0.0	0.0	0.1	1.5	24.5	28.4	21.8	11.2	6.9	2.7	1.1	1.1	0.9
-7.37	109.113	0.51	0.0	0.0	0.0	0.6	9.0	44.9	41.1	1.4	1.1	0.7	0.2	0.2	0.8
-7.64	110.345	2.02	0.0	0.0	0.0	1.1	17.4	35.9	30.5	6.7	4.3	1.8	0.7	0.7	0.9
-8.767	109.988	0	0.0	0.0	0.0	0.0	0.0	0.0	0.0	0.0	0.0	0.0	0.0	0.0	100.0
-8.41	108.72	0	0.0	0.0	0.0	0.0	0.0	0.0	0.0	0.0	0.0	0.0	0.0	0.0	100.0
-8.382	107.667	0	0.0	0.0	0.0	0.0	0.0	0.0	0.0	0.0	0.0	0.0	0.0	0.0	100.0
-7.912	106.286	0	0.0	0.0	0.0	0.0	0.0	0.0	0.0	0.0	0.0	0.0	0.0	0.0	100.0
-6.014	106.305	0	0.0	0.0	0.0	0.0	0.0	0.0	0.0	0.0	0.0	0.0	0.0	0.0	100.0
-5.422	107.893	0	0.0	0.0	0.0	0.0	0.0	0.0	0.0	0.0	0.0	0.0	0.0	0.0	100.0
-5.977	108.72	0	0.0	0.0	0.0	0.0	0.0	0.0	0.0	0.0	0.0	0.0	0.0	0.0	100.0
-6.484	109.734	0	0.0	0.0	0.0	0.0	0.0	0.0	0.0	0.0	0.0	0.0	0.0	0.0	100.0
-6.418	110.712	0	0.0	0.0	0.0	0.0	0.0	0.0	0.0	0.0	0.0	0.0	0.0	0.0	100.0
-6.531	112.008	0	0.0	0.0	0.0	0.0	0.0	0.0	0.0	0.0	0.0	0.0	0.0	0.0	100.0
-7.226	112.666	0	0.0	0.0	0.0	0.0	0.0	0.0	0.0	0.0	0.0	0.0	0.0	0.0	100.0
-7.659	112.666	0	0.0	0.0	0.0	0.0	0.0	0.0	0.0	0.0	0.0	0.0	0.0	0.0	100.0
-8.11	112.591	0	0.0	0.0	0.0	0.0	0.0	0.0	0.0	0.0	0.0	0.0	0.0	0.0	100.0
-8.476	112.478	0	0.0	0.0	0.0	0.0	0.0	0.0	0.0	0.0	0.0	0.0	0.0	0.0	100.0
-8.758	112.083	0	0.0	0.0	0.0	0.0	0.0	0.0	0.0	0.0	0.0	0.0	0.0	0.0	100.0
-8.955	111.341	0	0.0	0.0	0.0	0.0	0.0	0.0	0.0	0.0	0.0	0.0	0.0	0.0	100.0

Table A-2 Data input into TOTGS.

Appendix B Change of median grain size with distance from source for eruptions with samples for both phreatomagmatic and magmatic phases

Only a few eruptions (shown in Figure B-1) have phreatomagmatic and magmatic phases that have both been systematically sampled for grain size analysis. For Askja 1875, extensive proximal to distal sampling provides clear evidence of differing trends in grain size with distance for phreatomagmatic and magmatic phases. Other eruptions with more spatially limited sampling (< 50 km from source) include Eldgja 10th century and Ilopango ~ 1.5 ka BP, where the difference between wet and dry phases is less clear. For Grímsvötn 2011, sampling extended to > 100 km from source, but the small number of samples makes it difficult to identify a clear pattern.

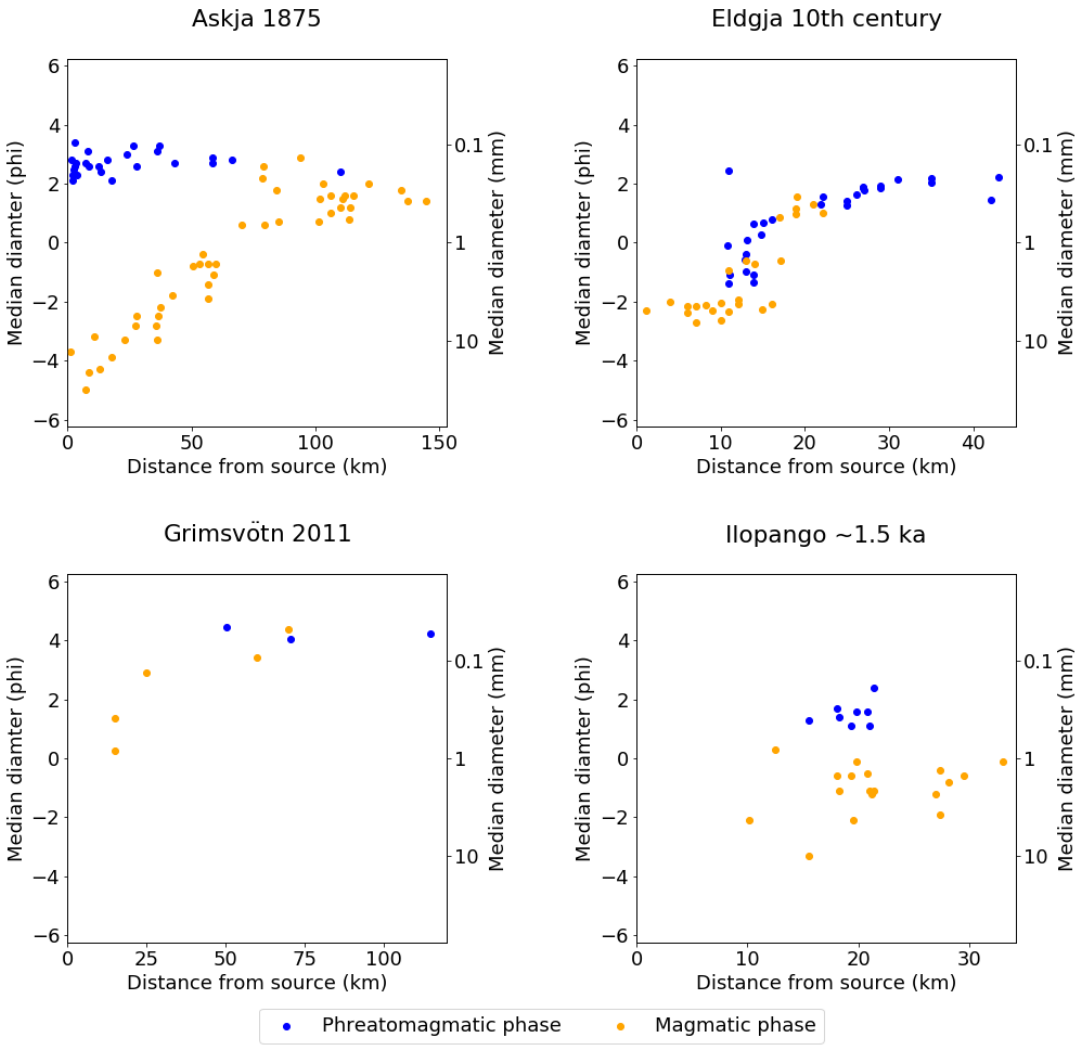

Figure B-1 Change of median grain size with distance from source for eruptions having both phreatomagmatic and magmatic phases.

Appendix C: Comparison of current VAAC default grain size distribution (GSD) with equivalent values on whole-Φ and half-Φ scales

Grain size distributions are often reported in Φ units:

$\Phi = - \log_2 (D/D_0)$

where D = particle size (in mm), and D_o = 1 mm (a reference value to make the equation internally consistent) (Krumbein, 1936; de' Michieli Vitturi et al., 2015).

To enable these GSDs to be input directly into NAME, we compiled and tested micron equivalents to whole Φ and half-Φ bins (Tables 3-4 and 3-5).

C.1 Converting micron values to Φ-scale

VAAC default particle size bins (Table 1-1) and Φ values are both uniformly distributed on a log scale, as shown in Figure A-1. For the London VAAC default PSD, the log of the particle diameter is uniformly distributed within each particle size bin, and the total mass is divided evenly over the total number of particles within a bin (Witham et al., 2017). Hence the proportion of particles from each micron bin to be allocated to each Φ bin can be calculated by scaling, and multiplied by the relevant mass fraction to obtain the mass fraction for the new Φ bins.

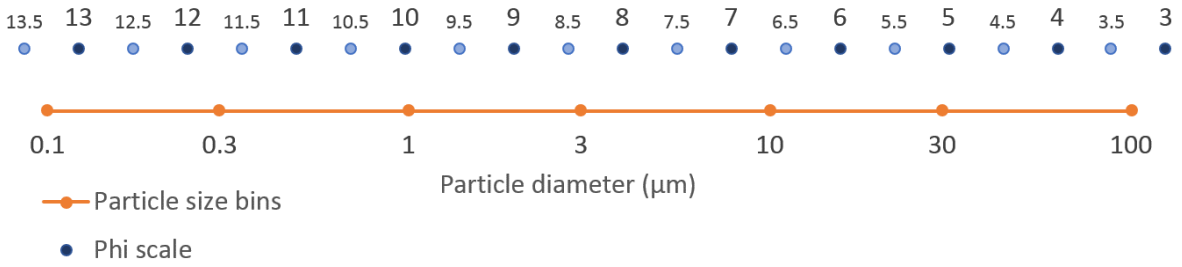

Figure C-1 VAAC default particle size bins and Φ values plotted on a log scale Φ bins.

For each VAAC default bin, the mass of particles allocated to the equivalent Φ bins (denoted by M_i, M_{i-1} etc.) can be defined by equation C-1 for Φ bins that straddle 2 micron bins and equation C-2 for Φ bins entirely within one micron bin, as shown in Figure C-2a.

$$M_{i-1} = \frac{m_j(L_{j+1} - D_i)}{L_{j+1} - L_j} + \frac{m_{j+1}(D_{i-1} - L_{j+1})}{L_{j+2} - L_{j+1}} \qquad \text{(C-1)}$$

$$M_{i-2} = \frac{m_{j+1}(D_{i-2} - D_{i-1})}{L_{j+2} - L_{j+1}} \qquad \text{(C-2)}$$

where $D = \log_{10}(1000 \times 2^{-\Phi})$ *(Φ values)*

$L = \log_{10}$(micron value)

m_j, m_{j+1} etc. are masses in the micron bins.

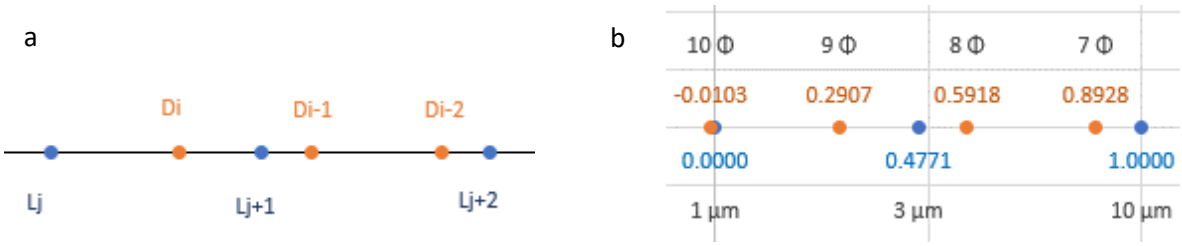

Figure C-2 Log values of Φ and micron scales a) general case. b) example for 8—9 Φ bin.

An example:

The 8—9 Φ bin sits partly in the 1—3 µm bin and partly in the 3 – 10 µm bin, which have mass fractions 5 % and 20 % respectively.

Mass fraction for 8—9 Φ:

$$5 \times \frac{(0.4771 - 0.2907)}{(0.4771 - 0)} + 20 \times \frac{(0.5918 - 0.4771)}{(1.00 - 0.4771)} = 6.338199$$

C.2 Comparison of current VAAC default PSD with equivalent values on whole-Φ and half-Φ scales

Figure C-3 shows the results of NAME simulations of the Eyjafjallajökull eruption during April 2010 for different binning of PSD. Source conditions were as shown in Table 3-6 and times for comparison were chosen to include periods of both high and low winds, and times of stronger and weaker plumes. When comparing the result for Φ-scale bins with the current VAAC default (Table C-1), the fractional bias (defined in Appendix D) is very low, at < +/- 0.01 in all cases except for the half-Φ scale when wind was low and plume was high (28 April 2010 12:00 UTC). In the latter case the plume dispersal was very limited and so even small differences between the model results are likely to have a large impact on the bias calculation.

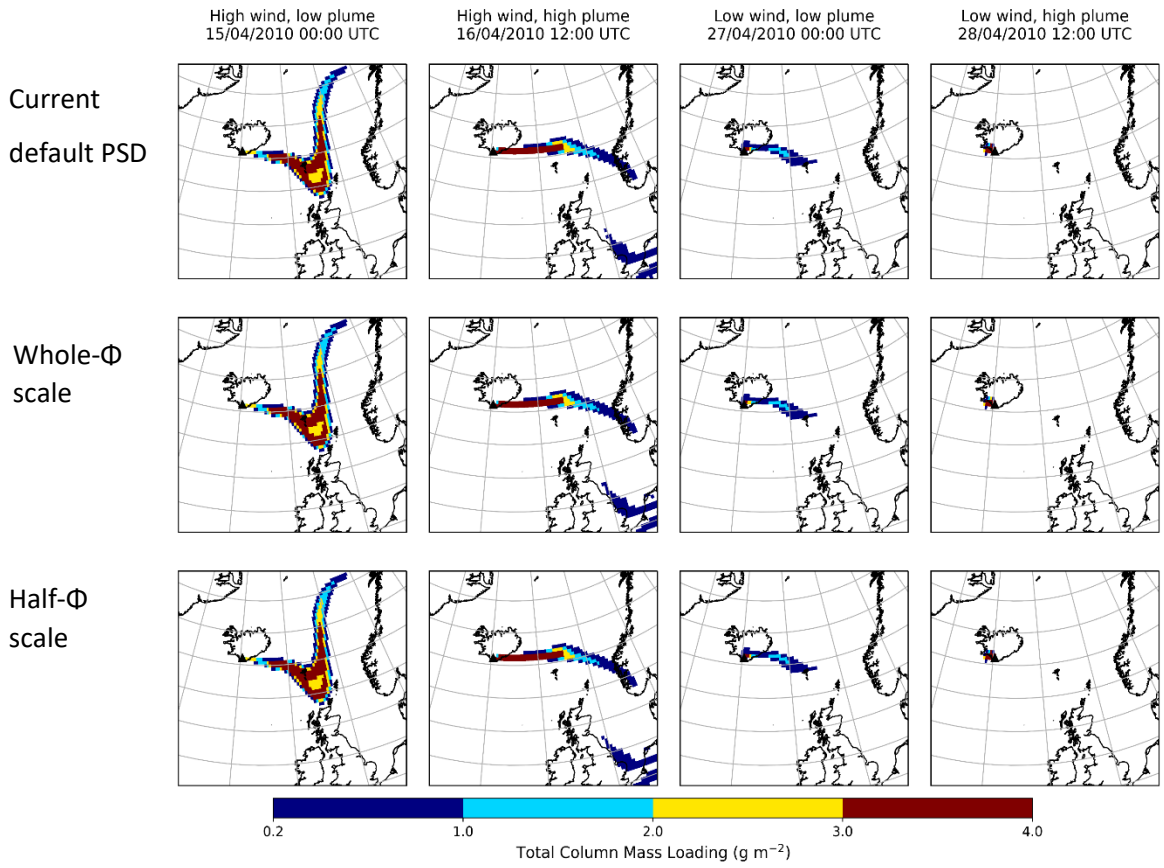

Figure C-3 Comparison of NAME output for total column mass loading using VAAC default PSD, whole-Φ scale PSD, half-Φ scale PSD, for times of high and low wind and high and low plume during the Eyjafjallajökull eruption 2010.

	15 April 2010 00:00 UTC	**16 April 2010 12:00 UTC**	**27 April 2010 00:00 UTC**	**28 April 2010 12:00 UTC**
Whole-Φ scale	-0.002	0.004	0.001	0.002
Half-Φ scale	-0.002	0.001	-0.003	1.371

Table C-1 Fractional bias of whole-Φ and half-Φ results (Figure A3) when compared with the VAAC default PSD. Fractional bias values range from -2 to +2 and positive values represent over-prediction.

Appendix D: Statistical tests and residual mass loadings

D.1 Statistical tests

Draxler et al. (2013) summarise the range of statistical tests used to describe differences between model and measured values, and to compare simulations using different models or different input parameters for the same model. The four tests selected for this study evaluate both ash concentration and spatial extent and have been used in other studies (e.g. Beckett et al., 2015; Leadbetter et al., 2015):

- Fractional Bias (FB) measures systematic bias with values ranging from +2 to -2 and positive values indicating an over-prediction. Results can be influenced by rare, high concentrations.
- Pearson's Correlation Coefficient (PCC) represents the linear relationship between 2 variables, with values of +1 and -1 indicating a positive and negative linear relationship respectively. For dispersion models, PCC tests ash mass loadings paired in time and space and quantifies differences both the spatial extent of the plume and ash concentrations within it. PCC has been found to be sensitive to outliers.
- Figure of Merit in Space (FoM) compares the spatial extents of the plumes and is a measure of the percentage overlap of two plumes. Values range from 0 when there is no overlap to 100 for complete overlap.
- The Kolmogorov-Smirnov Parameter (KSP) represents the difference between concentration distributions, but takes no account of the spatial distribution. The KSP is the maximum difference in the cumulative distribution of unpaired concentrations and values range from 0, where distributions are identical, to 100 % for distributions with no common values (Chang and Hanna, 2004; Draxler et al., 2013).

D.2 Air mass loadings for 6 May 2010

D.2.1 Fractional Bias

		Test eruption							
		VAAC	Rotongaio	Oruanui	Grímsvötn 2004	Eldgja	Hekla 1991	Eyja	Eyja Ground
Control eruption	VAAC		-0.412	-0.228	-0.584	-0.449	-0.742	-0.218	-0.318
	Rotongaio	0.412		0.188	-0.184	-0.039	-0.358	0.199	0.097
	Oruanui	0.228	-0.188		-0.369	-0.227	-0.538	0.010	-0.092
	Grímsvötn 2004	0.584	0.184	0.369		0.145	-0.178	0.379	0.279
	Eldgja	0.449	0.039	0.227	-0.145		-0.321	0.237	0.449
	Hekla 1991	0.742	0.358	0.538	0.178	0.321		0.547	0.452
	Eyja	0.218	-0.199	-0.010	-0.379	-0.237	-0.547		-0.102
	Eyja Ground	0.318	-0.097	0.092	-0.279	-0.449	-0.452	0.102	

D.2.2 Pearson Correlation Coefficient

	VAAC	Rotongaio	Oruanui	Grímsvötn 2004	Eldgja	Hekla 1991	Eyja	Eyja Ground
VAAC		0.973	0.992	0.947	0.965	0.916	0.992	0.983
Rotongaio	0.973		0.995	0.995	0.997	0.983	0.994	0.998
Oruanui	0.992	0.995		0.980	0.990	0.959	0.999	0.998
Grímsvötn 2004	0.947	0.995	0.980		0.996	0.996	0.979	0.989
Eldgja	0.965	0.997	0.990	0.996		0.984	0.988	0.996
Hekla 1991	0.916	0.983	0.959	0.996	0.984		0.957	0.973
Eyja	0.992	0.994	0.999	0.979	0.988	0.957		0.998
Eyja Ground	0.983	0.998	0.998	0.989	0.996	0.973	0.998	

D.2.3 Figure of Merit in Space

	VAAC	Rotongaio	Oruanui	Grímsvötn 2004	Eldgja	Hekla 1991	Eyja	Eyja Ground
VAAC		83.17	89.47	71.36	71.36	63.32	90.25	85.93
Rotongaio	83.17		92.46	85.80	85.80	76.13	91.18	96.21
Oruanui	89.47	92.46		79.33	79.33	70.39	93.30	94.44
Grímsvötn 2004	71.36	85.80	79.33		91.89	88.73	78.24	83.04
Eldgja	71.36	85.80	79.33	91.89		88.73	78.24	83.04
Hekla 1991	63.32	76.13	70.39	88.73	88.73		69.42	73.68
Eyja	90.25	91.18	93.30	78.24	78.24	69.42		94.21
Eyja Ground	85.93	96.21	94.44	83.04	83.04	73.68	94.21	

D.2.4 Kolmogorov-Smirnov Parameter

	VAAC	Rotongaio	Oruanui	Grímsvötn 2004	Eldgja	Hekla 1991	Eyja	Eyja Ground
VAAC		9.0	9.4	13.9	22.9	21.0	4.6	7.5
Rotongaio	9.0		4.8	6.0	16.9	15.0	9.2	4.4
Oruanui	9.4	4.8		9.0	13.8	15.5	10.6	9.4
Grímsvötn 2004	13.9	6.0	9.0		16.0	14.1	13.3	8.4
Eldgja	22.9	16.9	13.8	16.0		6.6	23.5	20.5
Hekla 1991	21.0	15.0	15.5	14.1	6.6		22.4	21.0
Eyja	4.6	9.2	10.6	13.3	23.5	22.4		7.4
Eyja Ground	7.5	4.4	9.4	8.4	20.5	21.0	7.4	

D.3 Air mass loadings for 8 May 2010

D.3.1 Fractional Bias

		Test eruption							
		VAAC	Rotongaio	Oruanui	Grímsvötn 2004	Eldgja	Hekla 1991	Eyja	Eyja Ground
Control eruption	VAAC		-0.807	-0.464	-1.165	-1.270	-1.522	-0.325	-0.636
	Rotongaio	0.807		0.378	-0.469	-0.622	-1.031	0.516	0.196
	Oruanui	0.464	-0.378		-0.811	-0.945	-1.284	0.145	-0.186
	Grímsvötn 2004	1.165	0.469	0.811		-0.165	-0.640	0.928	0.649
	Eldgja	1.270	0.622	0.945	0.165		-0.488	1.053	0.793
	Hekla 1991	1.522	1.031	1.284	0.640	0.488		1.366	1.168
	Eyja	0.325	-0.516	-0.145	-0.928	-1.053	-1.366		-0.328
	Eyja Ground	0.636	-0.196	0.186	-0.649	-0.793	-1.168	0.328	

D.3.2 Pearson Correlation Coefficient

	VAAC	Rotongaio	Oruanui	Grímsvötn 2004	Eldgja	Hekla 1991	Eyja	Eyja Ground
VAAC		0.987	0.995	0.956	0.905	0.846	0.990	0.991
Rotongaio	0.987		0.993	0.985	0.948	0.910	0.984	0.995
Oruanui	0.995	0.993		0.972	0.933	0.881	0.985	0.993
Grímsvötn 2004	0.956	0.985	0.972		0.965	0.953	0.962	0.979
Eldgja	0.905	0.948	0.933	0.965		0.973	0.890	0.930
Hekla 1991	0.846	0.910	0.881	0.953	0.973		0.848	0.889
Eyja	0.990	0.984	0.985	0.962	0.890	0.848		0.992
Eyja Ground	0.991	0.995	0.993	0.979	0.930	0.889	0.992	

D.3.3 Figure of Merit in Space

	VAAC	Rotongaio	Oruanui	Grímsvötn 2004	Eldgja	Hekla 1991	Eyja	Eyja Ground
VAAC		80.18	89.82	68.79	58.41	38.68	89.94	85.32
Rotongaio	80.18		88.60	85.57	72.64	48.18	86.65	92.99
Oruanui	89.82	88.60		76.51	64.96	43.01	91.68	92.67
Grímsvötn 2004	68.79	85.57	76.51		79.80	56.22	74.44	80.63
Eldgja	58.41	72.64	64.96	79.80		65.34	63.11	68.25
Hekla 1991	38.68	48.18	43.01	56.22	65.34		41.85	45.33
Eyja	89.94	86.65	91.68	74.44	63.11	41.85		91.98
Eyja Ground	85.32	92.99	92.67	80.63	68.25	45.33	91.98	

D.3.4 Kolmogorov-Smirnov Parameter

	VAAC	Rotongaio	Oruanui	Grímsvötn 2004	Eldgja	Hekla 1991	Eyja	Eyja Ground
VAAC		13.2	8.2	18.0	19.7	23.8	5.6	10.4
Rotongaio	13.2		6.4	7.4	14.4	16.0	8.4	3.4
Oruanui	8.2	6.4		13.0	15.0	19.7	8.0	4.3
Grímsvötn 2004	18.0	7.4	13.0		12.0	12.3	14.8	10.4
Eldgja	19.7	14.4	15.0	12.0		7.2	21.1	17.0
Hekla 1991	23.8	16.0	19.7	12.3	7.2		21.3	18.0
Eyja	5.6	8.4	8.0	14.8	21.1	21.3		5.7
Eyja Ground	10.4	3.4	4.3	10.4	17.0	18.0	5.7	

D.4 Deposits

D.4.1 Fractional Bias

		Test eruption							
		VAAC	Rotongaio	Oruanui	Grímsvötn 2004	Eldgja	Hekla 1991	Eyja	Eyja Ground
Control eruption	VAAC		0.265	0.201	0.336	0.361	0.398	0.068	0.213
	Rotongaio	-0.265		-0.064	0.073	0.098	0.137	-0.198	-0.052
	Oruanui	-0.201	0.064		0.137	0.162	0.201	-0.134	0.012
	Grímsvötn 2004	-0.336	-0.073	-0.137		0.026	0.065	-0.269	-0.125
	Eldgja	-0.361	-0.098	-0.162	-0.026		0.039	-0.295	-0.150
	Hekla 1991	-0.398	-0.137	-0.201	-0.065	-0.039		-0.333	-0.189
	Eyja	-0.068	0.198	0.134	0.269	0.295	0.333		0.146
	Eyja Ground	-0.213	0.052	-0.012	0.125	0.150	0.189	-0.146	

D.4.2 Pearson Correlation Coefficient

	VAAC	Rotongaio	Oruanui	Grímsvötn 2004	Eldgja	Hekla 1991	Eyja	Eyja Ground
VAAC		0.599	0.686	0.569	0.634	0.542	0.671	0.642
Rotongaio	0.599		0.993	0.999	0.992	0.996	0.995	0.997
Oruanui	0.686	0.993		0.988	0.994	0.980	0.999	0.998
Grímsvötn 2004	0.569	0.999	0.988		0.990	0.998	0.991	0.995
Eldgja	0.634	0.992	0.994	0.990		0.980	0.995	0.998
Hekla 1991	0.542	0.996	0.980	0.998	0.980		0.983	0.987
Eyja	0.671	0.995	0.999	0.991	0.995	0.983		0.999
Eyja Ground	0.642	0.997	0.998	0.995	0.998	0.987	0.999	

D.4.3 Figure of Merit in Space

	VAAC	Rotongaio	Oruanui	Grímsvötn 2004	Eldgja	Hekla 1991	Eyja	Eyja Ground
VAAC		64.62	82.04	47.17	52.40	35.97	81.20	72.17
Rotongaio	64.62		78.11	72.89	80.64	55.69	77.58	88.52
Oruanui	82.04	78.11		57.47	63.83	43.86	86.60	86.15
Grímsvötn 2004	47.17	72.89	57.47		85.21	75.84	57.08	65.35
Eldgja	52.40	80.64	63.83	85.21		68.68	63.17	72.39
Hekla 1991	35.97	55.69	43.86	75.84	68.68		43.56	49.87
Eyja	81.20	77.58	86.60	57.08	63.17	43.56		86.45
Eyja Ground	72.17	88.52	86.15	65.35	72.39	49.87	86.45	

D.4.4 Kolmogorov-Smirnov Parameter

	VAAC	Rotongaio	Oruanui	Grímsvötn 2004	Eldgja	Hekla 1991	Eyja	Eyja Ground
VAAC		18.9	9.4	28.9	30.4	38.5	12.9	16.0
Rotongaio	18.9		9.8	10.2	14.4	21.4	11.9	6.0
Oruanui	9.4	9.8		19.7	22.4	30.2	5.0	7.2
Grímsvötn 2004	28.9	10.2	19.7		7.8	14.0	20.8	14.6
Eldgja	30.4	14.4	22.4	7.8		9.9	25.1	19.7
Hekla 1991	38.5	21.4	30.2	14.0	9.9		32.4	26.8
Eyja	12.9	11.9	5.0	20.8	25.1	32.4		6.6
Eyja Ground	16.0	6.0	7.2	14.6	19.7	26.8	6.6	

D.5 Residual mass loadings

Residuals represent ash mass loadings remaining when spatially and temporally paired VAAC default values have been subtracted. Positive values indicate the test loading is higher than the VAAC default value. Figures D-1 and D-2 show residual mass loadings for air mass loadings on 6 May 2010 12:00 UTC and 8 May 2010 00:00 UTC respectively. Figure D-3 shows the same plot for deposit mass loadings for 4—12 May 2010.

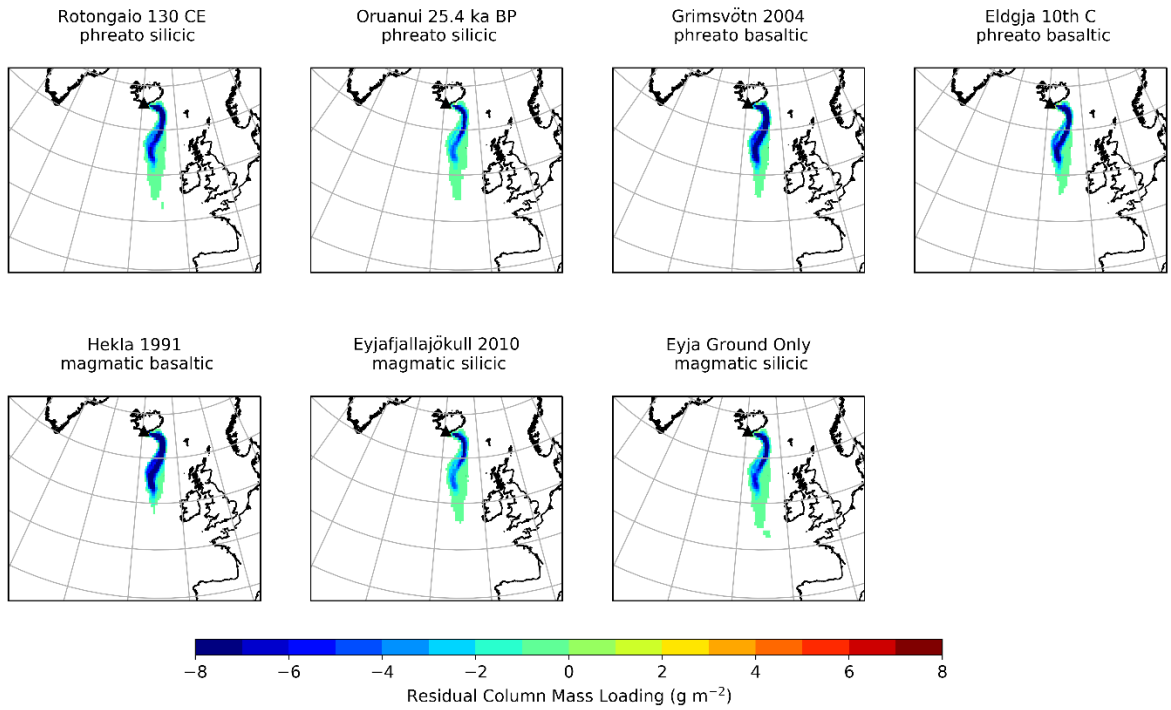

Figure D-1 Residuals for total column mass loading for 6 May 2010 12:00 UTC after removing VAAC default PSD values.

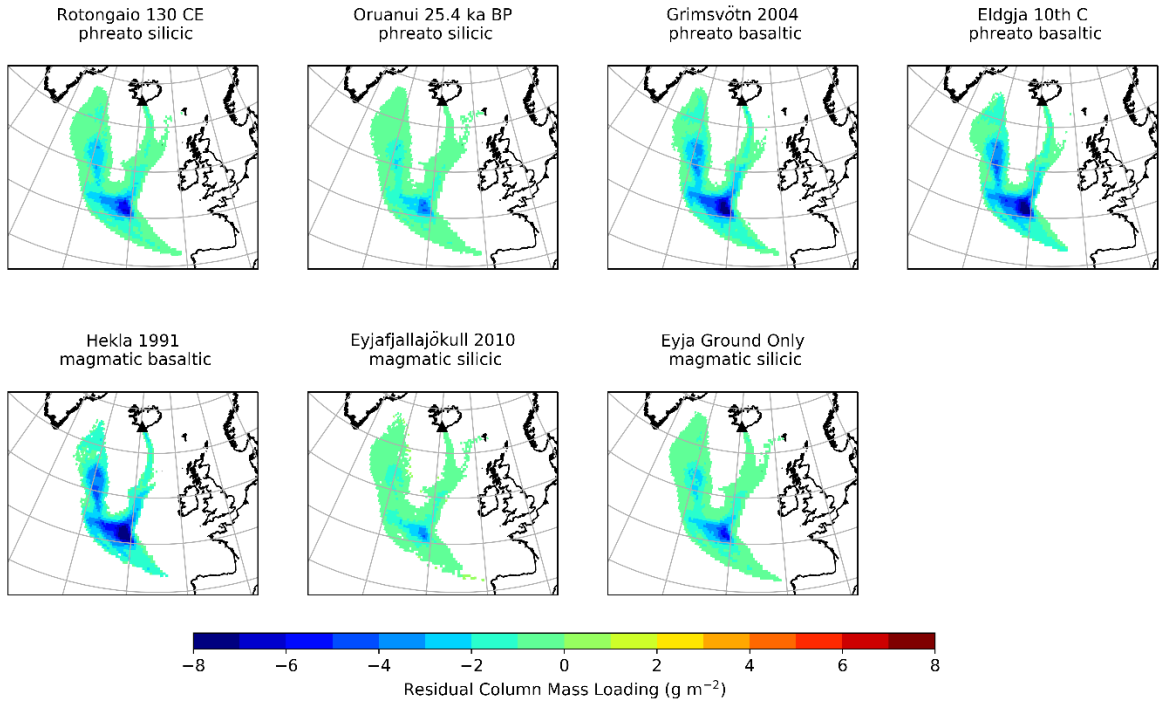

Figure D-2 Residuals for total column mass loading for 8 May 2010 00:00 UTC after removing VAAC default PSD values.

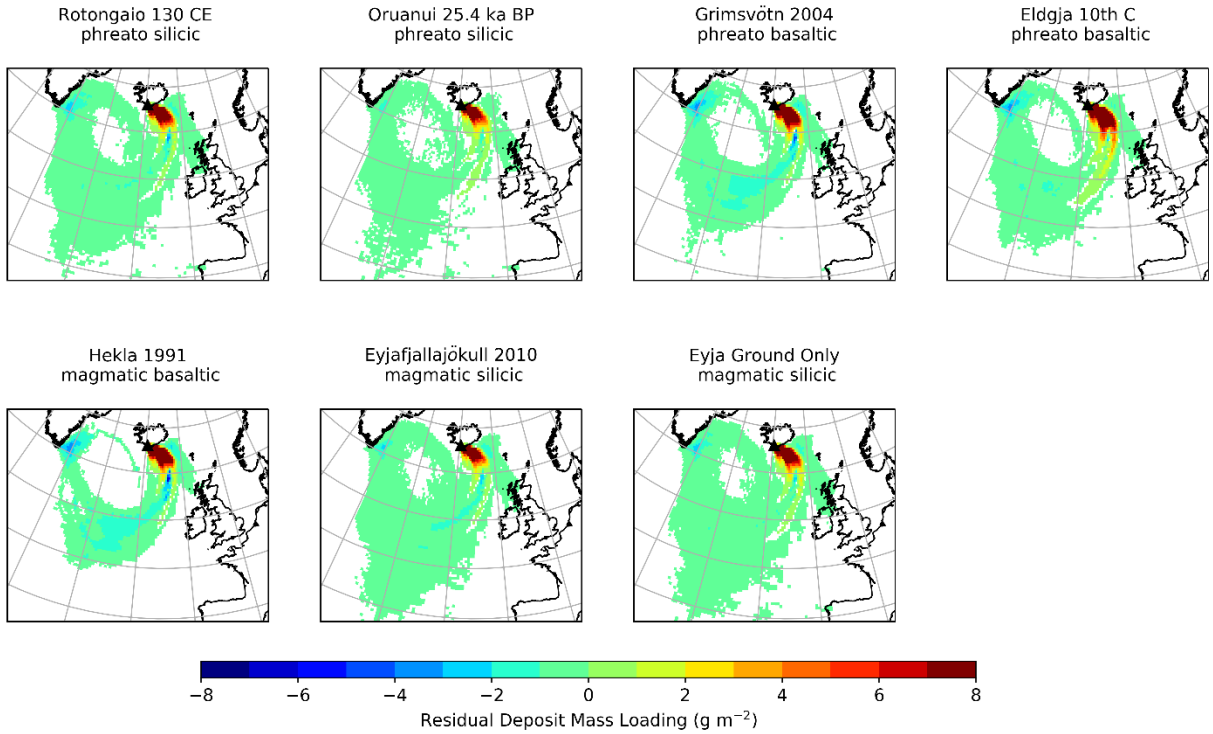

Figure D-3 Residuals for deposit mass loadings for 4—12 May 2010 after removing VAAC default PSD values.

Appendix E: NAME input file particle size distributions and cumulative mass fractions for test eruptions

Phi	PSD Diameter range boundary (μm)	Cumulative fraction						
		Oruanui	Rotongaio	Grímsvötn 2004	Eldgja 10th C	Eyjafjallajökull 2010	Eyjafjallajökull 2010 Ground only	Hekla 1991
11	0.4883					0		
10	0.9766			0		0.0186	0	
9.5	1.3811			0.0198				
9	1.9531	0	0	0.0221		0.04	0.0283	
8.5	2.7613			0.0292				
8	3.9063	0.0157	0.0466	0.0381	0	0.1194	0.0566	0
7.5	5.5243			0.0541	0.0031			0.008
7	7.8125	0.08	0.1274	0.0734	0.0093	0.2767	0.1419	0.0138
6.5	11.049			0.0992	0.0247			0.0291
6	15.625	0.3086	0.2014	0.1353	0.0617	0.4609	0.2855	0.0539
5.5	22.097			0.1906	0.142			0.0859
5	31.25	0.6286	0.4288	0.254	0.2901	0.6184	0.4851	0.155
4.5	44.194			0.3723	0.4969			0.2766
4	62.5	0.7914	0.637	0.5425	0.6975	0.8063	0.7428	0.4338
3.5	88.388			0.7756	0.858			0.6499
3	125	1	1	1	1	1	1	1

Appendix F: Additional NAME analyses

F.1 Changing particle release conditions

For the main set of model runs, particles were released along the whole height of the plume, but during the Eyjafjallajökull 2010 eruption, the weak plume was bent over by the wind (Petersen et al., 2012). The potential impact of this was investigated for 8 May 2010 00:00 by changing the particle release height. When model particles were released only from the top 1 km of plume, the extent of the plume was reduced but the highest total column mass loadings (10—30 g m^{-2}) covered a wider area as shown in Figure F-1. When ash concentrations were separated into different vertical heights, the bifurcation close to source was only seen in FL000-200 (where FL is flight level in hundreds of feet) for particles > 5 Φ (< 31.25 µm).

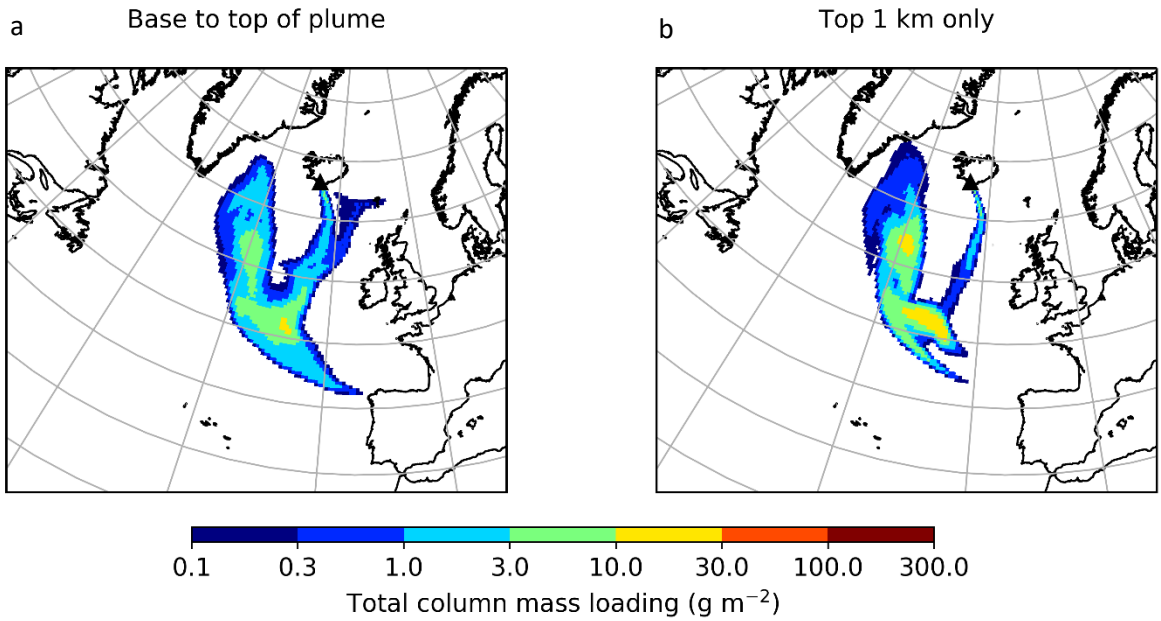

Figure F-1 Impact of changing particle release conditions. a) release from base to top of plume, b) release from top 1 km of plume only.

F.2 Wet and dry deposition

To investigate the relative importance of wet and dry deposition, the VAAC default PSD was run with only wet and only dry deposition for the same time period (Figure F-2). Dry deposition predominates with wet deposition occurring mainly close to source. The main set of NAME runs used the bulk wet deposition scheme in NAME which is expected to slightly underestimate proximal wet deposition for particles > ~ 3 µm in diameter, compared to using the PSD-dependent scheme (Webster and Thomson, 2017).

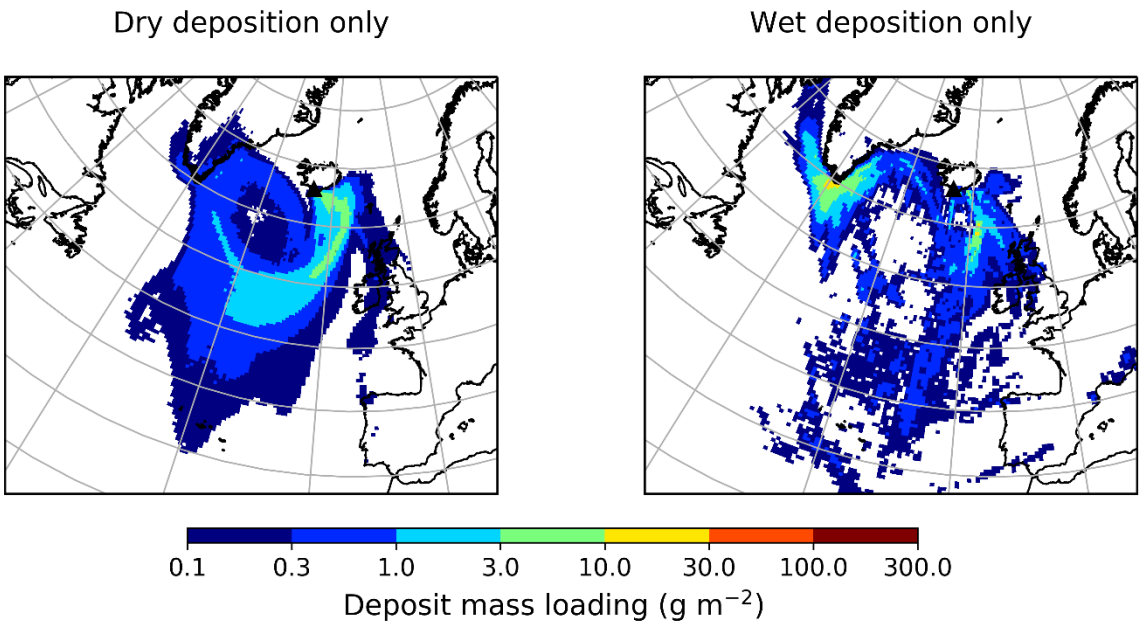

Figure F-2 NAME output with only dry and only wet deposition using VAAC default PSD.

Glossary of terms used

Italicised terms within definitions are also defined in this glossary.

Aggregation	Clustering of small particles to form larger composite grains which often have higher terminal velocities than their constituent particles.
Andesite	Volcanic rock with 57—63 weight % silica. See Figure G-1.
Ash	*Tephra* fragments < 2 mm in diameter.
Basalt	Volcanic rock with < 52 weight % silica. See Figure G-1.
Basaltic andesite	Volcanic rock with 52—57 weight % silica. See Figure G-1.
Basanite	Volcanic rock with low silica content. See Figure G-1.
Bed	Smallest distinct rock layer, representing deposition with specific source conditions. See also *unit.*
BP	Before present.
Caldera	Volcanic crater with diameter > 1 km.
CE	Common Era
Dacite	Volcanic rock with > 63 weight % silica. See Figure G-1.
Deposit mass loading	Mass of ash deposited on 1 m^2 on the ground (in g m^{-2}).
Distal	Far from source (hundreds of km). Compare to *proximal* and *medial*.
Dry deposition	Deposition of particles from a volcanic plume when atmospheric turbulence leads to impact with the ground.
Downfaulting	Subsidence within the centre of a caldera, following the evacuation of magma during an eruption. The space provided may accommodate *tephra* from the eruption and this must be taken into account when estimating the volume of erupted material.
Effusive eruption	Volcanic eruption producing lava flow (rather than explosive eruption producing *tephra*).
Eocene	Geological epoch (division of time) from ~ 56—34 million years ago.
Eruption source parameters	Values used to initialise a model, representing conditions at the source (e.g. plume height, *PSD*, *MER).*
Fragmentation	Brittle fracture of magma creating *tephra*.
Grain size distribution (GSD)	Size distribution of tephra particles in a sample (e.g. collected at a particular distance from source). Used to compile *TGSD*.
Ignimbrite	Rock formed from poorly-sorted fragments deposited by a *pyroclastic density current*.

Indurated	(Rock layer) hardened by heat or compaction.
Intensity	Measure of the size of an eruption based on *mass eruption rate*.
Intracaldera	Occurring within a *caldera*.
Isopach	Contour joining points of each thickness of tephra deposit.
ka	Thousand years
Lapilli	*Tephra* fragments 2—64 mm in diameter.
Lithic	Dense *tephra* fragments within a volcanic plume.
Mafic	Volcanic rock with low silica content (taken here as ≤ 63 weight %), including *basalt*, *basaltic andesite* and andes*ite*. See Figure G-1.
Magmatic eruption	Eruption without the influence of external. Compare to phreato*magmatic eruption*.
Magnitude	Measure of the size of an eruption based on erupted mass.
Medial	At intermediate distances from source (tens of km). Compare to p*roximal* and d*istal*.
Mass eruption rate (MER)	Rate at which magma is ejected during an eruption (in kg s^{-1}).
NAME	Lagrangian advection-diffusion model, used by London VAAC to simulate dispersal of *distal* ash plumes.
Paleocene	Geological epoch (division of time) from ~ 66—56 million years ago.
Paleosol	Soil horizon from the past, preserved because it was buried (e.g. under a volcanic deposit).
Phreatomagmatic eruption	Eruption where external water (e.g. groundwater, crater lake, glacier) is thought to have contributed to magma fragmentation. Compare to *magmatic eruption*.
Plinian eruption	Large explosive eruption with plume heights > ~ 24 km (Bonadonna and Costa, 2013).
Proximal	Close to source (few km). Compare to m*edial* and d*istal*.
Particle size distribution (PSD)	Size distribution of particles used as a model input parameter.
Pumice	Low density volcanic rock formed from vesicular magma.
Pyroclastic density current (PDC)	Erupted mix of gas and fragments moving under gravity, which may by formed by collapse of a volcanic plume.
Pyroclastic surge	Dilute concentration of fragments in a turbulent flow.
Rhyodacite	Volcanic rock with composition between *rhyolite* and *dacite*.
Rhyolite	Volcanic rock with high silica content (< ~ 70 %). See Figure G-1.

Scavenging	Removal of ash from the atmosphere by precipitation, leading to *wet deposition.*
Sedimentation	Fallout of particles from a volcanic plume under gravity.
Silicic	Volcanic rock with high silica content (taken here as > 63 weight %), Including *rhyolite* and *dacite*. See Figure G-1.
Stratosphere	Atmospheric layer above the troposphere. Volcanic ash reaching the stratosphere can result in a long-lived and globally extensive hazard.
Stratovolcano	Volcanic edifice built up of layers of *tephra* and lava from multiple eruptions.
Stromatolite	Rock-like mounds formed by layers of bacteria and sediment that form in shallow seas.
Subplinian eruption	Moderate to large explosive eruption with plume heights 14—24 km (Bonadonna and Costa, 2013).
Surtseyan eruption	Explosive eruption beneath a shallow lake or sea.
Syn-eruptive	Occurring at the same time as the eruption.
Tachylite	Volcanic glass with *basaltic* composition.
Tephra	All fragments produced during an explosive eruption, irrespective of size (including *lapilli* and *ash*).
Total grain size distribution (TGSD)	Best estimate of the size distribution of the total mass of *tephra* ejected during an explosive eruption. In this thesis, the TGSDs taken from published data are mainly compiled from *GSD*s obtained from ground samples at a range of distances from source, but no comment is made on the comprehensiveness of the input GSDs.
Tholeiite	*Basalt* with low sodium content, typical of mid-ocean ridge eruptions.
Total column mass loading	Mass of ash in the air column above 1 m^2 on the ground (in g m^{-2}).
Trachyandesite	Volcanic rock with silica content similar to *andesite*, but with higher alkali content. See Figure G-1.
Trachyte	Volcanic rock with high alkali and high silica content. See Figure G-1.
Triassic	Geological period (division of time) from ~ 250—200 million years ago.
Troposphere	Region of the atmosphere closest to Earth's surface, in which most weather events occur.

Unit	A distinct rock layer, often found at several locations, which can assist in identifying different phases of an eruption. Changing eruptive conditions may be identified by different *beds* (subunits) within the unit.
Vesicularity	Relating to vesicles (small pores within volcanic rock formed when gas bubbles become trapped within magma).
Volcanic Ash Advisory Centre (VAAC)	Centre designated by the International Civil Aviation Organization to provide forecasts of airborne ash to civil aviation.
Volcanic Explosivity Index (VEI)	Measure of the size of an explosive eruption based on erupted volume and plume height. Values range from 0 (smallest) to 8.
Volatile	Substance dissolved within magma at depth that exsolves as magma rises and decompresses to form bubbles e.g. water, carbon dioxide.
Vulcanian eruption	Small-to-moderate sized, short-lived explosive eruption, with plume heights up to ~ 20 km.
Wet deposition	Deposition of particles from a volcanic plume by falling precipitation (washout) or as cloud condensation nuclei (rainout).

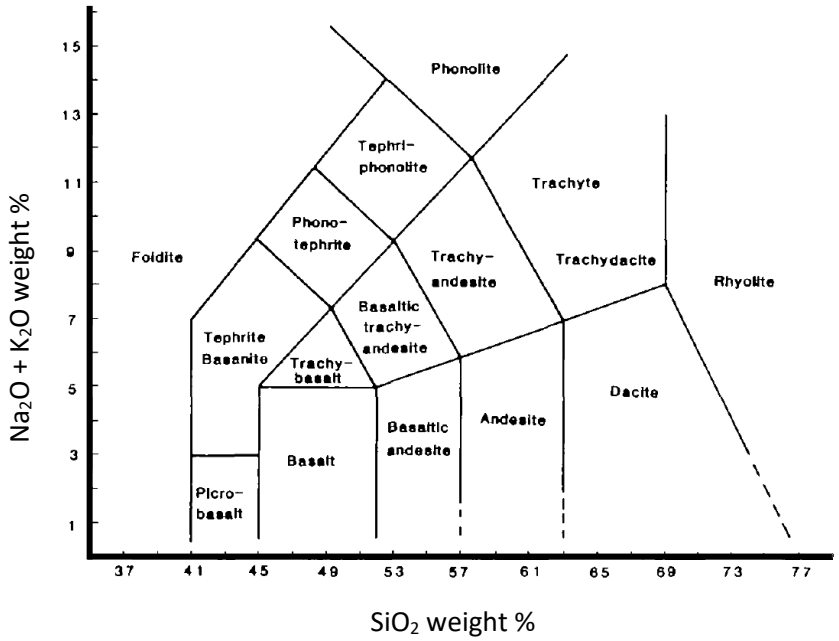

Figure G-1 Total alkali—silica (TAS) diagram showing classification of volcanic rocks by composition (Le Bas et al., 1986).